



Dipartimento di Fisica

CORSO DI LAUREA MAGISTRALE IN FISICA

Curriculum Fisica della Materia

Tesi di Laurea Magistrale

Generazione di Pattern Ottici per
l'Intrappolamento dell'Atomo di Itterbio con un
Modulatore Spaziale di Luce

Generation of Optical Patterns for Ytterbium
Atom Trapping with a Spatial-Light Modulator

Laureando:

Antonino Vardè

Relatore:

Prof. Francesco Scazza

Riassunto

Negli ultimi decenni, l'interesse per il campo degli *Atomi Ultrafreddi* è cresciuto considerevolmente, portando a un notevole miglioramento delle relative tecniche sperimentali. Questi sistemi, grazie alla loro versatilità, rappresentano una piattaforma ideale per la realizzazione di simulatori quantistici, orologi atomici e altri tipi di apparati incentrati sull'utilizzo delle proprietà quantistiche della materia.

Presso l'ArQuS Lab di Trieste è in corso lo sviluppo di uno di questi simulatori, basato su atomi di Itrerbio. Al livello attuale, l'esperimento consente di raffreddare gli atomi a temperature dell'ordine del microkelvin, per poi intrappolarli singolarmente in array monodimensionali di *Optical Tweezer*, generati tramite un singolo Acousto-Optic Deflector ed una sorgente laser a 532 nm.

Questa tesi si inserisce all'interno di questo progetto. Il suo scopo principale è stato la realizzazione di pattern bidimensionali di optical tweezers a 759 nm, lunghezza d'onda magica per la transizione di clock, utilizzando uno *Spatial Light Modulator*. Per fare ciò, è stato costruito un setup sperimentale nel quale siamo riusciti a generare questi array, ottenendo performance diffraction-limited grazie alla capacità di tale dispositivo di correggere le aberrazioni ottiche del sistema. Inoltre è stato sviluppato un modello per studiare la dinamica di tunneling degli atomi di Itrerbio all'interno di potenziali a doppia buca. Dalle simulazioni effettuate sono state ottenute frequenze di tunneling dell'ordine di 100 Hz. Tali potenziali possono essere generati tramite lo Spatial Light Modulator, apportando alcune modifiche al percorso ottico e agli algoritmi utilizzati per la generazione degli array di tweezer.

Questo lavoro rappresenta quindi il primo passo verso l'implementazione di uno *Spatial Light Modulator* sull'apparato sperimentale principale presente in laboratorio, grazie al quale sarà possibile generare potenziali con geometrie bidimensionali arbitrarie e tunabili in tempo reale in cui intrappolare gli atomi di Itrerbio.

Abstract

Over the last few decades, the interest in the field of *Ultracold Atoms* has grown considerably, leading to a remarkable improvement in the related experimental techniques. Due to their versatility, these systems provide an ideal platform for the realisation of quantum simulators, atomic clocks and other types of apparatuses focused on the utilisation of the quantum properties of matter.

One of these simulators, based on ytterbium atoms, is being developed at the ArQuS Lab in Trieste. At the present level, the experimental apparatus allows the atoms to be cooled to temperatures of the order of μK , and then trapped individually in one-dimensional arrays of *Optical Tweezers*, generated by using an Acousto-Optic Deflector with a 532 nm laser source.

This thesis reports on new developments within this project. Its main goal was the realisation of two-dimensional patterns of optical tweezers using a source at 759 nm, magic for the clock transition, utilising a *Spatial Light Modulator*. To do this, a test setup was constructed, by which we succeeded in generating arbitrary arrays, achieving diffraction-limited performance thanks to the ability of the device to correct for optical aberrations in the laser path.

In addition, a model was developed to study the tunneling dynamics of ytterbium atoms within double well potentials. From the simulations performed on them, tunneling rates of the order of 100 Hz could be obtained. These potentials can be generated using the Spatial Light Modulator, introducing some modifications to the optical path and the algorithms used to generate the tweezer arrays.

This work therefore represents the first step towards the implementation of a *Spatial Light Modulator* on the main setup in the lab, through which it will be possible to generate potentials with arbitrary and dynamically tunable two-dimensional geometries to trap ytterbium atoms.

Contents

Contents	7
Introduction	11
Thesis Overview	15
1 Theoretical Background	17
1.1 Radiative Forces	17
1.2 Laser Cooling	20
1.2.1 Zeeman Slower	20
1.2.2 Doppler Cooling	21
1.2.3 Magneto-Optical Trap	22
1.3 Optical Trapping	23
1.3.1 Dipole Traps	23
1.3.2 Optical lattices	24
1.4 Optical Tweezers	25
1.4.1 Energy Spectrum	26
1.4.2 Different Methods for Tweezers Generation	27
1.5 Ytterbium Atom	29
1.5.1 Magic Wavelength	30
2 The Spatial-Light Modulator	33
2.1 Technical Description	33
2.2 From Potential Differences to Phase Shifts	35
2.3 From Phase to Amplitude	36
2.3.1 Fourier Optics	37
2.3.2 Thin Lens	39
2.3.3 Wavefront Propagation	40
2.4 Phase-Retrieval Algorithms	43
2.4.1 The Gerchberg-Saxton Algorithm	44
2.5 Aberrations Correction	47
2.5.1 Phase-Shift Interferometry	48
3 Experimental Setup and Results	53
3.1 Titanium-Sapphire Laser	53
3.2 Experimental Setup	54
3.3 Working with the SLM	57
3.3.1 Lookup Table	58

3.3.2	Vendor Phase Correction	61
3.3.3	The Zero-Order	62
3.3.4	Fourier Calibration	64
3.4	Wavefront Calibration	65
3.4.1	The Diffraction Limit	69
3.5	Active Compensation of Inhomogeneities	72
3.6	Results Evaluation	75
3.6.1	Arrays	75
3.6.2	Minimum Distance	76
3.6.3	Generic Images	77
3.7	Theoretical model	79
3.8	Blurring Effect	84
3.9	Generation via SLM	88
3.10	Speckle Noise	89
	Conclusions and Outlooks	93
	Bibliography	97

Introduction

The idea that nature is composed of small and invisible objects that combine to create matter, dates back to ancient Greece, where philosophers, like Democritus, referred to them as " $\alpha\tauομος$ ", which means indivisible.

Their first experimental evidence dates back to the beginning of the nineteenth century, when John Dalton, during his experiments, noticed that matter tends to combine in definite proportions. This and other observations led him to lay the foundation of the modern atomic theory, triggering a mechanism that, in the following century, led to the birth of *Quantum Mechanics*, drastically changing our interpretation of the Universe and producing groundbreaking discoveries.

Among these, one of the most incredible was the invention of the *LASER* (Light Amplification by Stimulated Emission of Radiation) [53], a device based on quantum light-atom interactions.

By exploiting the properties of this device, in the 1990s various scientists, including Steven Chu, Claude Cohen-Tannoudji, and William Phillips [9], demonstrated that it was possible to cool and trap clouds of atoms using laser radiation. This made it possible to study in a completely new way these objects, which until less than two hundred years earlier were considered only as a philosophical concept. The field of *Cold Atoms* was born.

Nowadays, these techniques have evolved to the point where it is possible to trap and control even single atom in a sample, making them the most natural option for creating a quantum simulator able to resolve quantum many-body problems, that with classical computation would be impossible to perform in reasonable time [13]. By arranging and perturbing them in different ways, it is indeed possible to study the physics behind systems ranging from condensed matter physics [51, 7, 50] to cosmology [56]. Other applications of these platforms include quantum computing [6], atomtronics [3], and ultraprecise timekeeping [2].

One laboratory where such control on atoms has been recently achieved is the ArQuS Lab in Trieste, where this thesis work has been carried out.

The long-term goal of this laboratory is to create a quantum simulator based on ytterbium atoms to study various condensed matter systems, and in particular so-called impurity-problems, such as the *Kondo Problem* and its extensions [49].

In Figs. 1 and 2, 3D renders of the main part of the setup are displayed. In the first one we show the full vacuum system, while the second one is a zoomed-

in view of the region surrounding the science cell.

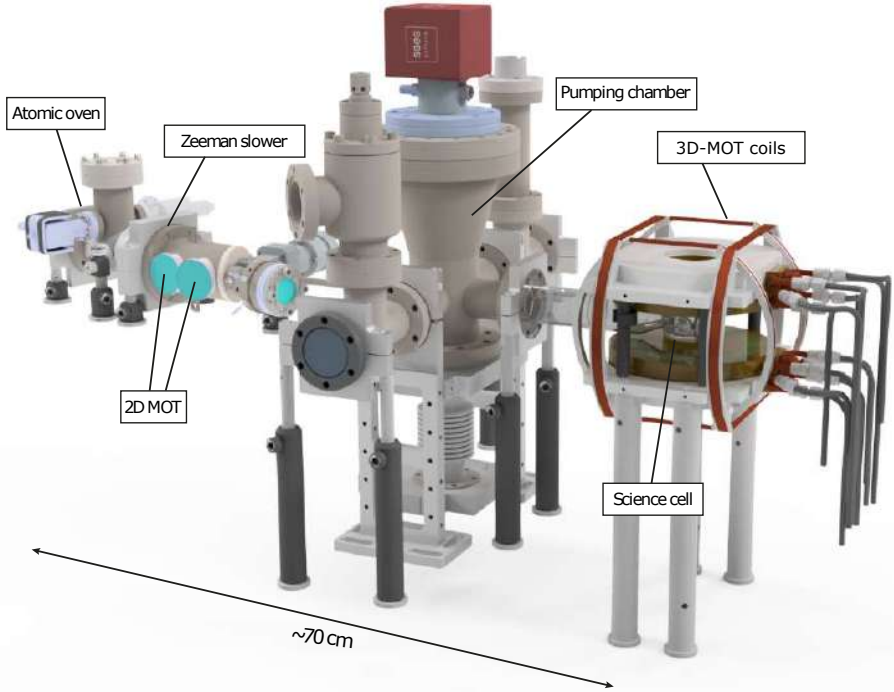


Figure 1: A 3D render of the main part of the setup.

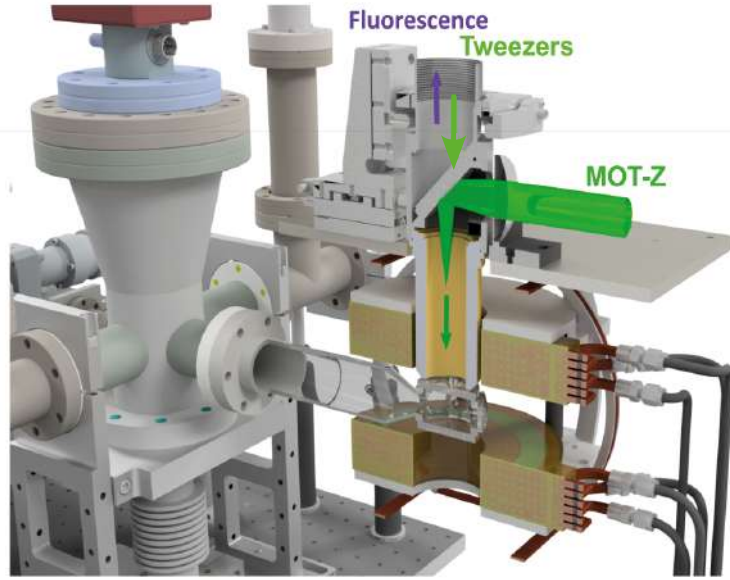


Figure 2: A 3D render of the science cell region.

We begin by describing the setup with the oven, where the atom reservoir is heated to $380\text{ }^{\circ}\text{C}$, generating an atomic flux of $\sim 10^{12}$ atoms/s. A permanent magnet Zeeman slower performs the initial slowing of the atomic beam. Then a 2D-MOT cools and confines the atoms in the plane orthogonal to the beam

propagation direction, but also deflects the atom flux by 20° , aligning its path with the science cell and filtering out all atoms that are still too fast. The resulting slow beam has an axial velocity of ~ 40 m/s and a radial velocity lower than 0.65 m/s. Both stages are implemented using lasers resonant with the blue transition (${}^1S_0 \rightarrow {}^1P_1$) at 399 nm.

At this point, the atoms arrive in the pumping chamber, where the pressure is reduced from the previous value of 5×10^{-10} mbar to 2×10^{-11} mbar, improving the quality of the ultra-high vacuum. Before entering the science cell, another cooling step is performed using two crossed beams, both resonant with the 399 nm transition. These beams further decelerate the atoms to a velocity of a few meters per second, below the capture velocity of the 3D-MOT¹.

The science cell is an octagonal glass chamber. Inside, the atoms are trapped using a 3D-MOT, with beams resonant with the green transition (${}^1S_0 \rightarrow {}^3P_1$) at 556 nm. The tweezers beam enters from the top of the science cell (Fig. 2), focused by a microscope objective (not shown in the figures) with a numerical aperture (NA) of 0.6. This beam has a wavelength of $\lambda = 532$ nm, which is magic for the green transition used for the 3D-MOT. The blue imaging beam enters from the side, producing scattered photons that are partly collected by the microscope objective and directed to the camera. Using this setup, single ytterbium atoms can be trapped and imaged, as shown in Fig. 3.

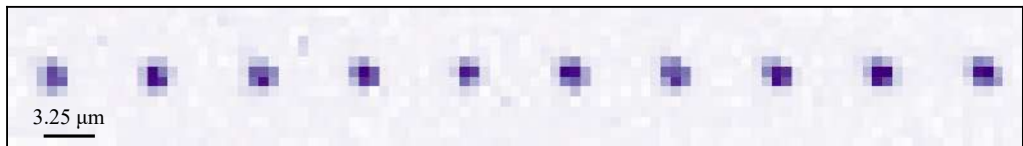


Figure 3: An array of single ${}^{174}\text{Yb}$ atoms trapped inside optical tweezers, obtained at the ArQuS Lab in Trieste. The image is produced by averaging over ~ 100 independent realizations.

The aim of this thesis was to build a optical setup to characterize the performance of a Spatial Light Modulator (SLM), with the future perspective of implementing it in the setup shown in Fig. 1 to enable the generation of bidimensional patterns at a wavelength of 759 nm, magic for the clock transition². We also tested the ability of this device to compensate for aberrations, achieving diffraction-limited performance in the optical setup. Furthermore, we developed a model based on engineered double-well potentials to study the tunnelling dynamics with ytterbium atoms, which we also attempted to generate using the SLM. This would offer the possibility to study lattice models, and in particular the *Su-Schrieffer-Heeger* (SSH) model, by controlling the tunneling rates between different sites of the arrays.

¹Velocity below which the MOT is able to trap atoms.

²See subsection 1.5.1

As we will see, the potential of this device is limited only by the optical resolution and the experimentalist's imagination, offering exciting perspectives for what will be achieved once it will be implemented in the main setup.

Thesis Overview

This thesis is divided into four chapters:

- Chapter 1: The first chapter introduces the basic concepts behind radiative forces and their role in laser cooling and trapping, as well as the working principles of some of these techniques. A more detailed description of optical tweezers, a type of dipole trap, is provided. The final section is dedicated to the specific properties of the ytterbium atom.
- Chapter 2: In this chapter we presents the necessary theoretical concepts to understand how the Spatial Light Modulator (SLM) works, explaining how it enables control over the wavefront of an incident beam, and the algorithm used for this purpose, the Gerchberg-Saxton Algorithm. The chapter concludes itself with a brief discussion of optical aberrations, followed by the procedure used to compensate for them via the SLM.
- Chapter 3: The third chapter discusses the realization of the test setup, including all the necessary procedures needed to properly operate the SLM. We continue with the implementation of the various algorithms, such as the one used for aberration compensation, followed by an analysis of the obtained Point-Spread Function. The chapter concludes with the generation of the tweezer arrays, where a feedback loop is used to improve the uniformity of the resulting patterns.
- Chapter 4: Finally, the last chapter presents the developed model to study the tunnelling dynamics in a double-well potential. In the simulations, we also take into account the blurring effect resulting from the finite aperture associated with the optics. An attempt to obtain this potential is shown, concluding with a discussion on how to resolve the Speckle Noise.

Chapter 1

Theoretical Background

In this chapter, we will introduce some concepts and techniques related to the field of quantum simulations with neutral atoms, which will help to contextualize this thesis project.

We will begin with the derivation of the *Scattering Force* and *Dipole Force*, which are consequences of light-atom interactions. Next, we will discuss some of the most common techniques used for cooling and trapping atoms with lasers, based on these forces. Due to its relevance in this thesis work, a separate section will be dedicated to a particular type of dipole trap, called *Optical Tweezer*. Finally, the last section will explore the properties of the ytterbium atom, aiming to justify its central role in the main experiment ongoing in laboratory.

1.1 Radiative Forces

In this section, we will present a simple derivation of the Scattering and Dipole Forces, consequences of the mechanical effects of radiation on atoms.

Consider the atom as a two-level system characterized by a frequency ω_0 , interacting with an incident monochromatic radiation, defined by a frequency ω and a wavevector \vec{k} . The Hamiltonian of the system can be written as:

$$\hat{H} = \hat{H}_a^{ext} + \hat{H}_a^{int} + \hat{H}_{a-l} \quad (1.1)$$

The three terms describes the external and internal degrees of freedom of the atom, and the atom-light interaction, respectively. Their explicit form is:

$$\begin{aligned} \hat{H}_a^{ext} &= \frac{\hat{\vec{P}}^2}{2M} \\ \hat{H}_a^{int} &= \hbar\omega_0|e\rangle\langle e| + 0 \cdot |g\rangle\langle g| \\ \hat{H}_{a-l} &= \hat{V}_{laser}(\hat{\vec{R}}) + \hat{V}_{vacuum}(\hat{\vec{R}}) \end{aligned} \quad (1.2)$$

We want to calculate the expectation value of the force exerted by the laser radiation on the atom. To do this, we can use the *Ehrenfest Theorem* [20, Cap. 1]:

$$\vec{F} = \frac{d}{dt} \left\langle \hat{\vec{P}} \right\rangle = \left\langle -\nabla \hat{H} \right\rangle \quad (1.3)$$

leading to:

$$\vec{F} = - \left\langle \nabla \hat{V}_{laser}(\hat{\vec{R}}) \right\rangle - \left\langle \nabla \hat{V}_{vacuum}(\hat{\vec{R}}) \right\rangle \quad (1.4)$$

The second term is related to the spontaneous emission phenomenon resulting from the isotropic coupling with the vacuum field, and thus emitted in random directions. The net force resulting from these events can be neglected.

The first term, under the *Dipole Approximation*,¹ can be written as $\hat{V}_{laser}(\hat{\vec{R}}) \approx -\hat{\vec{d}} \cdot \hat{\vec{E}}(\hat{\vec{R}})$. If we also assume the position and momentum of the atom to be classical quantities, we obtain:

$$\vec{F} \approx \left\langle \nabla \left[\hat{\vec{d}} \cdot \vec{E}(\vec{R}) \right] \right\rangle = \sum_i \langle \hat{d}_i \rangle \nabla E_i(\vec{R}) \quad (1.5)$$

The last assumption is valid if the fluctuations of \vec{R} and \vec{P} are small compared to the quantities involved in our discussion. This leads to the following two conditions:

$$\Delta R \ll \lambda \quad \Delta P \ll \frac{\Gamma M}{k} \quad (1.6)$$

The condition on the position fluctuations arises from the requirement that the fluctuations in the atom's position are small enough to be ignored by the light-atom interaction, and thus small compared to λ , the length scale over which the electromagnetic field associated with the radiation changes significantly.

To obtain the condition on ΔP , we must impose that the homogeneous broadening of the absorption coefficient is much larger than the Doppler broadening, which is an inhomogeneous feature depending on the velocity of the atom [14, Cap. 7, 8]. This, as before, ensures that the fluctuations of the momentum can be neglected in treating the light-atom interaction, leading to the following condition:

$$\Gamma_D = k\Delta V = k \frac{\Delta P}{M} \ll \Gamma \quad (1.7)$$

where Γ_D is the linewidth resulting from the Doppler broadening, obtaining ΔP . Even if we approximate these quantities with their expectation values, their uncertainties are still related by the Heisenberg Uncertainty Principle:

$$\hbar \leq \Delta R \cdot \Delta P \ll \frac{\Gamma M}{k} \lambda \quad (1.8)$$

¹The Dipole Approximation is valid if the dimension of the atom, d_{atom} , is much smaller than λ .

From this condition we obtain that:

$$\Gamma \gg 2\omega_R = \frac{\hbar k^2}{M} \quad (1.9)$$

where ω_R is the recoil frequency, associated with the energy gained or lost by an atom when it absorbs or emits a photon, respectively.

The inverse of this frequency define the timescale on which the atom makes significant movements. In Eq. (1.9), we see that this timescale is much larger than the one related to the absorption and emission events of the internal degrees of freedom, which is defined as the inverse of Γ , and therefore we can consider them to be in a stationary state.

Eq. (1.5) becomes:

$$\vec{F} \approx \sum_i d_i^{st} \vec{\nabla} E_i(\vec{R}) \quad (1.10)$$

For simplicity, we will consider the electric field of a linearly polarized plane wave, $\vec{E}(\vec{R}) = E_0(\vec{R}) \cos(kz - \omega t) \cdot \hat{y}$, obtaining:

$$\vec{F} \propto \frac{dE_0(\vec{R})}{dz} \cos(kz - \omega t) - kE_0(\vec{R}) \sin(kz - \omega t) \quad (1.11)$$

The dipole and scattering forces derive from the first and second terms of this equation, respectively [14, Cap. 9]. Their explicit expressions are:

$$\vec{F}_{scatt} = \hbar \vec{k} \frac{\Gamma}{2} \frac{s}{1+s} = \hbar \vec{k} R_{scatt} \quad (1.12)$$

$$\vec{F}_{dip} = -\frac{\hbar \delta}{2} \frac{\vec{\nabla} s}{1+s} \quad (1.13)$$

where $\delta = \omega - \omega_0$ is the detuning, R_{scatt} is the scattering rate, and s is the saturation parameter, which is related to the intensity of the radiation and corresponds to:

$$s = \frac{\Omega^2/2}{\delta^2 + \Gamma^2/4} \quad (1.14)$$

We can define the dipole potential as $U_{dip}(\vec{R}) = \frac{\hbar \delta}{2} \ln[1 + s(\vec{R})]$, obtaining:

$$\vec{F}_{dip} = -\vec{\nabla} U_{dip}(\vec{R}) \quad (1.15)$$

which explicitly shows the conservative nature of the dipole force.

If we take the first-order expansion of $U_{dip}(\vec{R})$ for $s \ll 1$, corresponding to the low saturation regime, assuming $|\delta| \gg \Omega, \Gamma$, we obtain:

$$U_{dip}(\vec{R}) \approx \frac{\hbar \Omega^2(\vec{R})}{4\delta} \propto I(\vec{R}) \quad (1.16)$$

which essentially corresponds to the behaviour associated with the *Light Shift* [14, Cap. 7].

In Fig. 1.1, we can see a qualitative plot of the two forces.

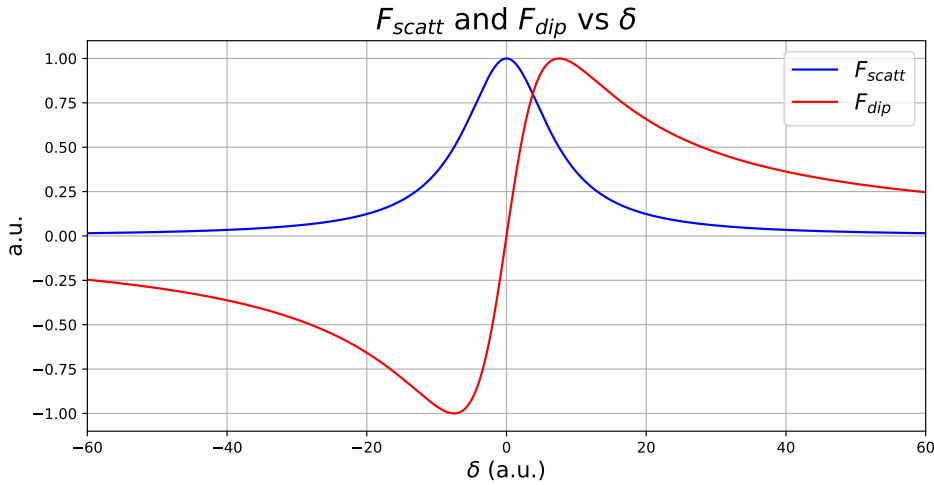


Figure 1.1: Qualitative plot of the scattering and dipole forces for different values of the detuning, δ . The scattering force was calculated assuming a Gaussian spatial profile for the intensity of the electromagnetic source.

As we can see, the scattering force has an absorptive profile, consistent with the fact that it arises from photon absorption, while the dipole force has a dispersive profile, reaching its maximum values far from resonance.

1.2 Laser Cooling

We will discuss two cooling techniques based on the scattering force: the *Zeeman Slower* and the *Doppler Cooling*, which is also referred to as *Optical Molasses*.

1.2.1 Zeeman Slower

Imagine a flux of atoms moving along a certain direction. If we illuminate it with a counterpropagating beam, the scattering force will reduce the velocity of the atoms. As we see from Eq. (1.12), the force exerted by the incident beam is given by the product of the momentum carried by a single photon multiplied by the scattering rate. Each absorbed photon reduces the velocity of the atom by $\Delta v = \frac{\hbar k}{M}$. Of course, when the photon is re-emitted, the atom's velocity changes again, but since the spontaneous emission occurs in a random direction due to the isotropic coupling with the vacuum field, the mean effect of this process, as a first approximation, can be neglected.

To effectively decelerate atoms using this principle, one must account for the change in resonance frequency due to the Doppler shift, produced by their deceleration.

This problem is solved by applying a non-uniform magnetic field that compensates the variations in the Doppler shift through the Zeeman effect. This configuration is known as *Zeeman Slower* [28, Cap. 2]. A schematic representation of this technique is shown in Fig. 1.2.

In this setup, the beam frequency is resonant with the atoms when they are at

rest. As the atoms decelerate, the Doppler shift is compensated by a magnetic field that gradually decreases along the direction of the cooling beam, accounting for their changing velocity.

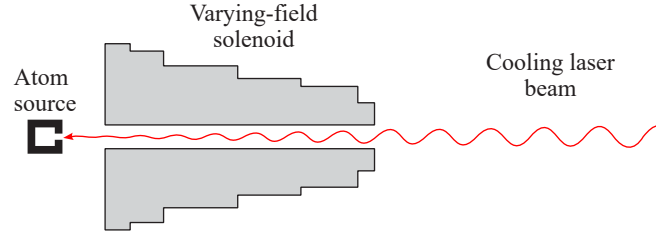


Figure 1.2: Zeeman Slower diagram, adapted from [14].

This procedure is typically the first step in cold atom experiments, such as in the main experiment ongoing in the laboratory, already discussed in the introduction.

1.2.2 Doppler Cooling

The idea behind this technique, is to use two counterpropagating red-detuned laser beams, with orthogonal polarizations to prevent interference, in order to cool atoms moving along the their axis. Due to Doppler shift, atoms will experience an imbalance in the scattering forces, as the beam they are moving toward will be more resonant than the other. The resulting force in this configuration is [14, 28]:

$$F_{molasses} = F_{scatt}(\omega - \omega_0 - kv) - F_{scatt}(\omega - \omega_0 + kv) \underset{v \rightarrow 0}{\approx} -\alpha v \quad (1.17)$$

which, in the limit of small velocities, can be approximated by a functional form similar to that of the viscous friction. For this reason, the configuration is also called *Optical Molasses*.

Note that this treatment is valid only for low saturation, otherwise, correlations between the photons absorbed from the two beams will arise, and we will no longer be able to consider the resulting force as the sum of two independent terms.

This configuration can also be extended to three dimensions, using three sets of counterpropagating beams. A diagram of a 3D optical molasses is shown in Fig. 1.3, along with a real one used to cool Sodium atoms [36].

Doppler Cooling has a lower temperature limit, known as the *Doppler Limit*, which is caused by fluctuations in the scattering force due to the Poissonian statistics of the photons emitted by the laser beams, as well as by the random kicks produced by spontaneous emissions. These factors increase the mean square velocity, $\bar{v^2}$, of the atoms, and consequently their mean kinetic energy, $\bar{E}_C = \frac{1}{2}M\bar{v^2}$. The Doppler limit is reached when a balance between the cooling produced by the scattering forces and the heating rate due to fluctuations is achieved. It

corresponds to [14, Cap. 9]:

$$T_D = \frac{\hbar\Gamma}{2k_B} \quad (1.18)$$

for $\delta = -\Gamma/2$, where Γ is the linewidth of the transition used in the cooling process.

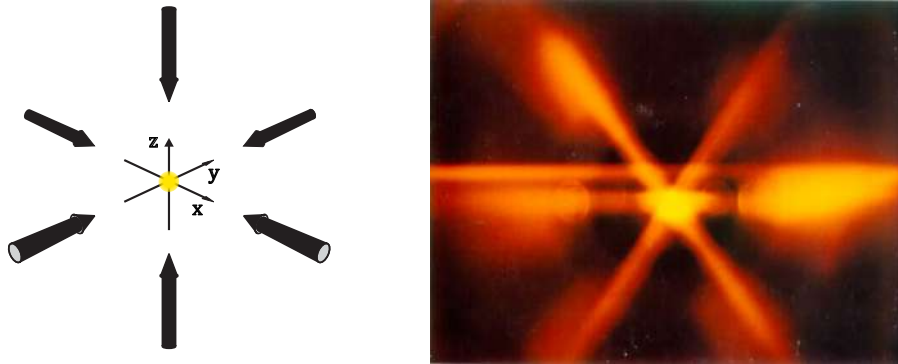


Figure 1.3: On the left, a diagram of a 3D optical molasses, while on the right, a picture of an optical molasses generated for sodium atoms, which allowed to cool them to a temperature of $20 \mu\text{K}$ [36].

1.2.3 Magneto-Optical Trap

We have already explained the principles behind the Doppler cooling. Even if this technique allows us to reach temperatures of tens of μK , does not provide any confinement to the atomic cloud. Indeed, once "stopped", atoms are left in their positions until fluctuations will diffuse them out of the beam trajectories. In a Magneto-Optical Trap, confinement is achieved using a non-uniform quadrupole magnetic field, which creates a preferential region to which atoms are directed while being cooled. This works only if the pairs of counterpropagating beams are circularly polarized in opposite directions².

In Fig. 1.4, on the left, we can see a scheme of a 3D-MOT. The magnetic field is produced by two coils carrying opposite currents. The quadrupole field induces a Zeeman splitting in the energy states of the atoms, favoring their interaction with the beam they are moving toward, respect to the other one. This imbalance adds a pulling effect toward the center of the molasses to the cooling mechanism. One of the factors that limit the atoms lifetime inside a MOT are the collisions with the background room-temperature gas³. For this reason, the confinement region of a MOT is placed in cells where ultra-high vacuum conditions are maintained. In Fig. 1.4, on the right, we can see the 3D-MOT obtained at the ArQuS

²For a more detailed explanation, see Refs. [14, 28].

³Note that this effect is dominant at low density, while at high density, losses are dominated by atom-atom interactions.

Lab for the ^{174}Yb , at the center of the octagonal science cell.

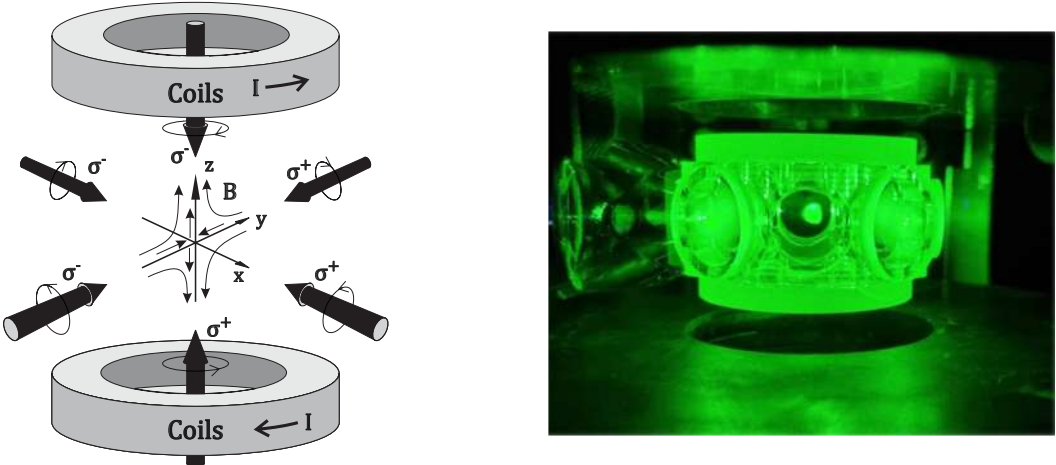


Figure 1.4: On the left, a schematic representation of a 3D-MOT, adapted from [14], while on the right, a picture of the 3D-MOT obtained at the ArQuS Lab for ^{174}Yb .

1.3 Optical Trapping

Another fundamental aspect of cold atom experiments is the trapping of atoms, which is typically performed after the cooling process. In this section, we will focus on architectures based on dipole force, called *Dipole Traps*.

1.3.1 Dipole Traps

The term *Dipole Traps* refers to all types of optical traps based on the dipole force. These traps are created by illuminating atoms with a highly detuned laser, and due to the weak intensity of the dipole force, they can trap atoms only if they are cold enough, typically below 10 mK ⁴.

Since the dipole force is conservative, if an atom descends to lower potential regions its kinetic energy will increase due to energy conservation, leading to an ineffective confinement⁵. An intuitive vision on this mechanism can be obtained by thinking to a ball rolling down from . This can be avoided by placing the atoms directly at the bottom of the potential, or by providing a dissipative mechanism, such as inside a MOT or molasses.

⁴Note that, due to the high-detuned wavelength used for this kind of traps, the scattering force does not interfere much with them (see Fig. 1.1).

⁵A classical analogy could be a ball rolling down a frictionless dip. Since there is no energy dissipation, it will enter from one side and escape from the other.

One of the advantages of this kind of trap is the possibility of generating it with any geometry [4], making it useful for applications ranging from atomtronics [3] to quantum computing [6].

They can be red-detuned ($\delta < 0$), where the atoms are trapped in the regions of highest intensity, or blue-detuned ($\delta > 0$), where they are instead repelled from these regions [21]. Some examples of these dipole traps are shown in Fig. 1.5.

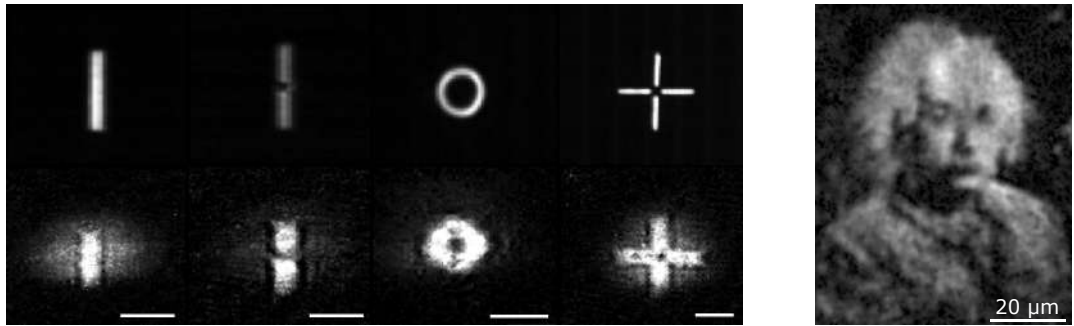


Figure 1.5: Some examples of dipole traps taken from [3] used to trap a Bose-Einstein Condensate for atomtronics application. Atoms are thus trapped in light-tailored "circuits", which act as a matterwave waveguides and interferometers. The potentials on the left were generated with an SLM. The top row shows the potential used for trapping, while the bottom row shows the trapped BEC. The white bar indicates a length of $100 \mu\text{m}$.

The potential on the right shows a BEC trapped in a "Einstein" dipole trap generated with a DMD.

This thesis work is focused on the realization of red-detuned traps, such as optical tweezers, as well as double-well potentials for the study of tunneling dynamics.

1.3.2 Optical lattices

We want to dedicate a few words to this type of dipole trap, since it is one of the most widely used, particularly for the generation of ordered arrays, providing an excellent platform for studying lattice models such as the Hubbard model.

These traps are created from the standing wave resulting from the interference of two counterpropagating laser beams. Depending on the sign of the detuning, the atoms are trapped at the antinode ($\delta < 0$) or at the nodes ($\delta > 0$). These types of traps are very effective at confining atoms over small, sub- μm length scales, due to the fact that the intensity of the field goes from its maximum value to zero over a distance of $\lambda/2$ [14, Cap. 9]. An example of optical lattice can be seen in Fig. 1.6.

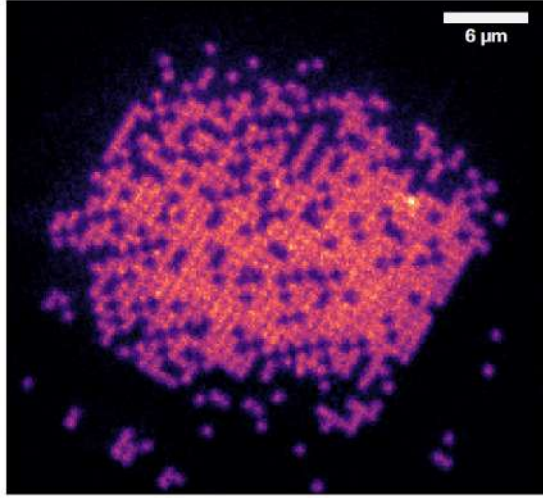


Figure 1.6: A *Mott Insulator* obtained by trapping ^{133}Cs atoms in an optical lattice, taken from [55].

1.4 Optical Tweezers

Optical Tweezers are red-detuned dipole traps created by focusing a laser beam into a very small region, typically with a linear dimension of $\sim 1 \mu\text{m}$, allowing to trap even a single atom. These highly focused spots are achieved through high numerical aperture microscope objectives.

The shape of these traps, in an ideal system with homogeneous illumination, corresponds to the point spread function of the optical setup, which as a consequence of the circular aperture of the microscope objectives is an Airy pattern. Since the Airy pattern is well approximated by a Gaussian profile, we assume this as the shape of the potential (3.20). At the focal point, we have:

$$U(x, y) = -U_0 \exp \left\{ -2 \left[\left(\frac{x - x_0}{\sigma_x} \right)^2 + \left(\frac{y - y_0}{\sigma_y} \right)^2 \right] \right\} \quad (1.19)$$

Two key parameters to characterize an optical tweezer are the trap depth and the radial trap frequencies.

The depth corresponds to the peak intensity of the potential, while the trap frequencies are defined as follows:

$$\omega_q = \sqrt{\frac{1}{M} \frac{\partial^2}{\partial q^2} U(x, y) \Big|_{q=0}} \quad (1.20)$$

where $q = x, y$. Similarly, we can also define an axial trap frequency [37]. For the potential given in Eq. (1.19), the radial trap frequencies are:

$$\omega_{x,y} = \sqrt{\frac{4|U_0|}{m\sigma_{x,y}^2}} \quad (1.21)$$

Before continuing, we would like to say a few words about the physical meaning

of the trap frequency.

The quality of a red-detuned dipole trap depends strongly on the dipole force produced by the light field, which is proportional to the intensity gradient. This means that better confinement is associated with more rapidly varying potentials. Around their minimum, we can approximate the potential in Eq. (1.19) with a parabola. The resulting parabolic approximation can be compared with the potential of a Harmonic Oscillator:

$$U_{HO}(x, y) = -U_0 + \frac{1}{2}m [(\omega_x x)^2 + (\omega_y y)^2] \quad (1.22)$$

yielding the trap frequency defined in Eq. (1.20), which indicates how steep the parabola is, and thus how intense the dipole force is.

This is why we want to make optical tweezers as small as possible.

1.4.1 Energy Spectrum

Since the trap frequencies of a tweezer are defined using the parabolic approximation, it is interesting to evaluate the energy spectrum of an atom trapped inside to verify the validity of this assumption.

We limit our evaluation to a one-dimensional section of the Gaussian potential in Eq. (1.19), considering it as a perturbed version of the Harmonic Oscillator potential. The energy levels are calculated using first-order perturbation theory, assuming the eigenfunctions of the Harmonic Oscillator as the unperturbed ones. The parameters defining the tweezers are those typically employed in the laboratory to trap ytterbium atoms [30].

In Fig. 1.7, we plot the lowest levels of the calculated energy spectrum, along with their relative errors compared to the Harmonic Oscillator energy levels. As expected, the quality of the parabolic approximation decreases as one ascends the potential, due to the cutoff of the Gaussian curve. This also means that the validity of the approximation is reduced at lower trap depth values.

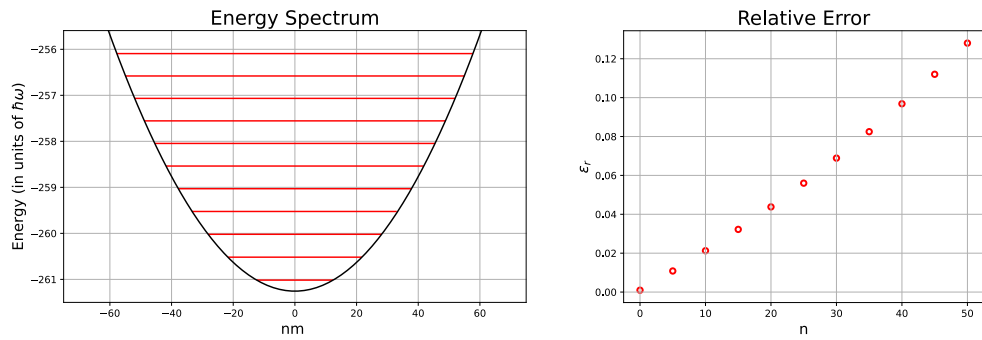


Figure 1.7: On the left, we show the ten lowest energy levels of the tweezer spectrum for $V_0 = k_B \cdot 2.3$ mK, $w_0 = 578$ nm, $\omega_x \sim 2\pi \cdot 180$ kHz and $\lambda = 532$ nm. We used the mass of the ^{171}Yb .

On the right, the relative errors between the obtained energy levels and those of the harmonic oscillator. n is the index identifying the states.

1.4.2 Different Methods for Tweezers Generation

Optical tweezers can be generated in many different ways. Since one of the main goals of this thesis work is their generation using an SLM, we will briefly compare it with the two other devices commonly used for this purpose: the *Acousto-Optic Deflector* (AOD) and the *Digital Micromirror Device* (DMD).

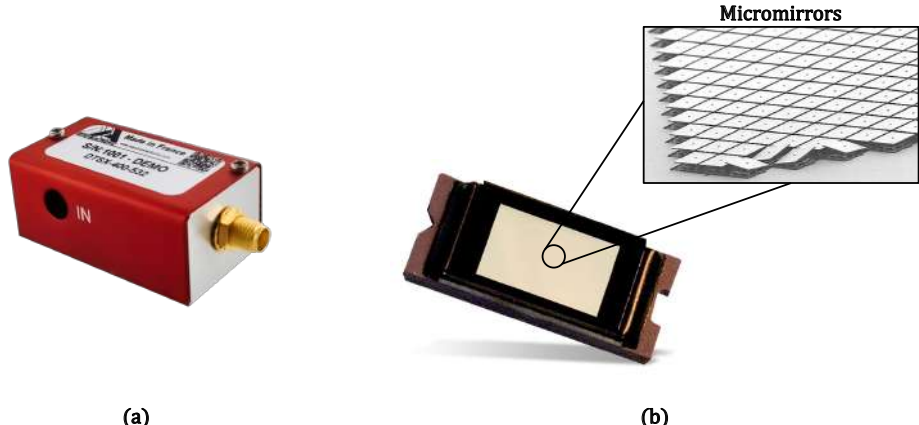


Figure 1.8: An AOD (a), similar to the model used in the laboratory, and a DMD (b), with a zoom on the micromirror array.

An AOD (Fig. 1.8a) is a device that uses the acousto-optic effect to diffract an incident beam into its various diffraction orders, each of which generates an optical tweezer. Two-dimensional arrays can be obtained by using two AODs oriented perpendicularly in sequence. AODs are faster than SLMs but can only generate simple square or rectangular patterns. In Fig. 1.9 we see a chain of optical tweezers obtained in the laboratory using an AOD.

A DMD (Fig. 1.8b) consists of a rectangular grid of micromirrors that allow to generate arbitrary intensity patterns by deflecting locally the light from the incident. This device also enables much faster dynamics compared to an SLM, which is slower due to the settling time required for the liquid crystals to stabilize. Since it is based on amplitude modulation, the generation of tweezers with this device involve only some of the micromirrors in the display, while the rest will direct away from the imaging zone incident light. This increases the sensitivity to local aberrations and results in very low light utilization efficiency. For this reason, it is typically used for generating smoother intensity patterns rather than spot arrays.

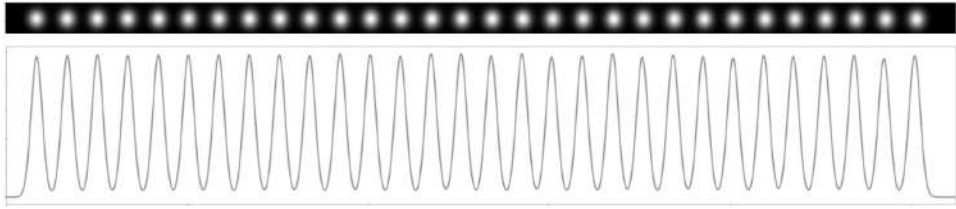


Figure 1.9: A linear chain of optical tweezers generated with an AOD and the relative intensity section, taken from Ref. [30].

Obviously, we cannot consider one device better than the others, but rather better suited for specific purposes.

However, there is one feature that the other two devices may envy to the SLM, that is the ability to correct aberrations to a level that even the DMD cannot reach, due to the lower number of degrees of freedom possessed by the micromirrors respect to those of liquid-crystal pixels.

This feature, along with the ability to generate static tweezer arrays and arbitrarily shaped potentials, makes the SLM the best option for our scenario.

One last observation: independently of the device used, it can be shown that the optimal working condition for the generation of tweezers, ensuring the highest trap frequency and depth, as well as high power transmission through the microscope objective, is achieved when $\frac{w_0}{R} \sim 1$ [37] where w_0 is the waist of the tweezer and R is the radius of the aperture associated to the objective.

This consideration guided us in the choice of the optics used for the test setup shown in 3.2.

We conclude with Fig. 1.10, showing the state of the art of atom trapping using optical tweezers.

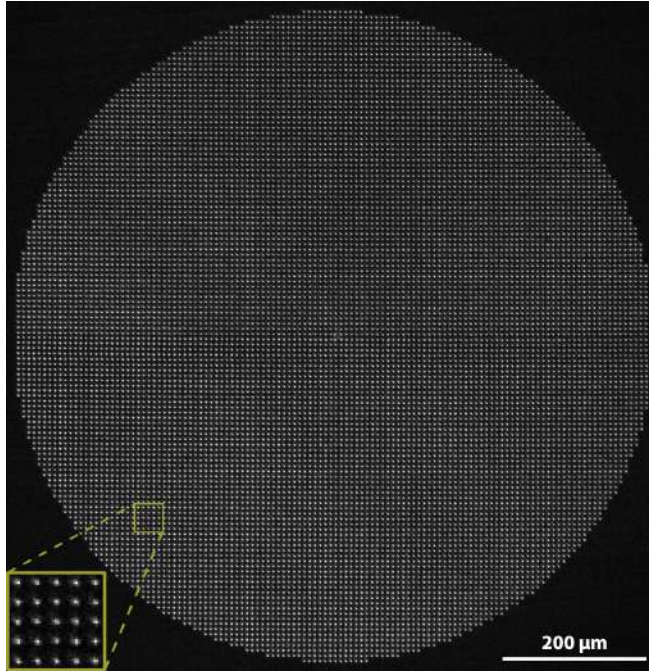


Figure 1.10: Twelve thousand sites of single ^{133}Cs atoms trapped inside an SLM generated optical tweezer array. The image is obtained by averaging over many measurement. Image taken from Ref. [38].

1.5 Ytterbium Atom

Last section of this chapter is dedicated to the ytterbium atom, with the aim of discussing its peculiar properties which motivate its use in the main experiment ongoing in the laboratory.

Ytterbium is a rare earth metal with an atomic number $Z = 70$. Due to its high atomic number, it has a wide variety of stable isotopes, both bosonic and fermionic in nature, offering the possibility to study phenomena arising from both types of statistics.

Its electronic configuration is $[\text{Xe}] 4f^{14} 5d 6s^2$, with a ground state, in the spectroscopic notation $^{2S+1}L_J$, given by 1S_0 . In Fig. 1.11, we can see the lowest levels of the fine structure of the ytterbium atom, with three of its most relevant transitions.

The *blue* transition ($^1S_0 \rightarrow ^1P_1$) has a wavelength of $\lambda = 398.9$ nm and a linewidth of $\Gamma = 2\pi \cdot 29.1$ MHz. Due to the large linewidth, this transition is used for the Zeeman slower, the initial 2D-MOT, the crossed beams and the imaging process.

Then we have the *green* transition ($^1S_0 \rightarrow ^3P_1$), with a wavelength of $\lambda = 555.8$ nm and a linewidth of $\Gamma = 2\pi \cdot 182.4$ kHz. This transition is narrower because it violates the selection rule for the spin quantum number ($\Delta S = 0$). Due to its moderate narrowness, it is used for the generation of the 3D-MOT, which has a Doppler limit of $T_D \approx 4.4$ μK

Lastly, we have the *yellow* transition, also called the *clock transition* ($^1S_0 \rightarrow ^3P_0$). It has a wavelength of $\lambda = 578.4$ nm and a linewidth of $\Gamma = 2\pi \cdot 10$ mHz. As we can see, this transition is incredibly narrow. This is a consequence of a double violation of the selection rule, and in particular, it violates the rule on the quantum spin number and the rule on the total angular momentum number, which prohibits transitions between two states with $J = 0$.

Due to the extremely low value of Γ , this transition is used to realize atomic clocks (hence the name). Additionally, as a consequence of its long lifetime, the 3P_0 state is metastable and can be considered as another ground state. This offers the possibility to study impurity physics, where impurities are modeled by atoms excited to the 3P_0 state. A more detailed explanation of this and other applications of this transition can be found in [30, 48].

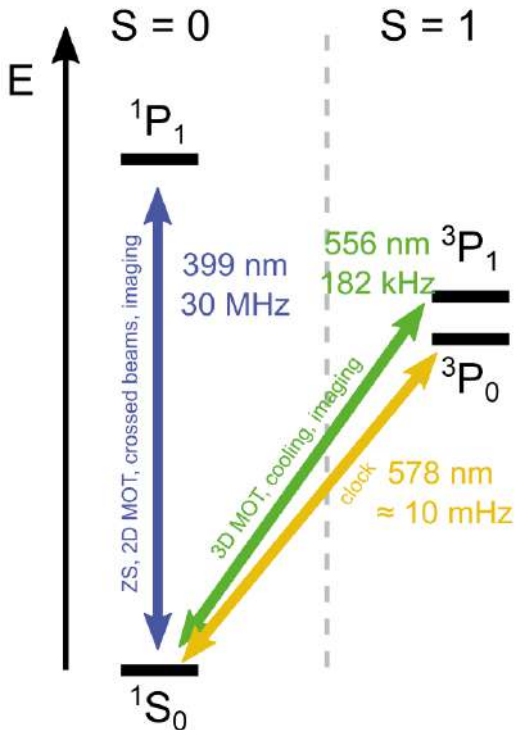


Figure 1.11: The lowest levels of the fine structure of ytterbium, with the most relevant transitions and their various applications indicated.

1.5.1 Magic Wavelength

As we have already discussed in the first section of this chapter, the force produced by a laser on an atom depends on its dipole moment (Eq. (1.10)), which, in turn, depends on two quantities: the applied electromagnetic field and the *polarizability* of the atom's state. This last quantity tells us how an atom in a

particular state behaves under the influence of an external radiation⁶.

If, for a given wavelength λ of the electromagnetic field, the polarizability of two different states of an atom, $|i\rangle$ and $|f\rangle$, is the same, they will experience the same dipole force, and thus the same light shift. The wavelength λ is said to be the *Magic Wavelength* for the $|i\rangle \rightarrow |f\rangle$ transition. These magic wavelengths are particularly useful when dealing with narrow transitions, such as the clock transition, because even a slight shift in one of the two levels can cause the clock laser to fall out of resonance.

One of the magic wavelengths for the clock transition is 759.37nm [12] (in particular for the ^{171}Yb) which indeed is the frequency of the laser source used in this thesis work to create the amplitude patterns through SLM.

Another magic wavelength (depending on the isotope) is 532 nm, which is magic for the green transition used to generate the 3D-MOT, and it is currently used to generate the optical tweezers in the laboratory (Fig. 3).

In conclusion, the ytterbium atom, due its variety of isotopes, transitions, and the presence of many relevant magic and non-magic wavelengths, offers the possibility to study a wide range of physical phenomena, making it the main character of the ArQuS Lab.

⁶Since an atom is not a true 2-level system, a more complete treatment of atomic polarizability requires considering all possible transitions from the state taken as a reference to all the other states in its spectrum. We will keep the discussion at a qualitative level, but a more detailed discussion on atomic polarizability can be found in [52, Cap. 1].

Chapter 2

The Spatial-Light Modulator

A *Spatial Light Modulator* (SLM) is a device capable of locally modifying the phase of an incident beam, giving full control over the reflected wavefront. In this chapter, we will explore the key aspects of its operation and use.

First, we will describe the SLM model used for this thesis project, and then the principles behind the generation of the desired amplitude patterns. We will explain how local potential differences translate into phase shifts and how these are related to the amplitude patterns in a particular point on the optical path. Since this relation is known, we can use some algorithms, based on the *Gerchberg - Saxton Algorithm* (GSA), to determine the correct phase patterns to apply on the SLM display in order to obtain arbitrary intensity profiles.

We conclude this chapter by showing how the SLM can be used to compensate the aberrations of the optical system. Some of the most important types of aberrations will be presented, and then we will discuss a procedure based so-called phase-shift interferometry to compensate the aberrations affecting an optical setup using the SLM.

2.1 Technical Description



Figure 2.1: The *LCOS – SLM X15213 – 02* of Hamamatsu (taken from Ref. [23]).

The Spatial Light Modulator used for this thesis work is the *LCOS – SLM X15213 – 02* of Hamamatsu, where *LCOS* stands for *Liquid Crystal on Silicon*. This model has a dielectric mirror that covers the active matrix circuit, generating reflectivity up to 97% for wavelengths in the range of 750 – 850 nm. As shown in Fig. 2.1 the device consists of two parts, the *head* and the *controller*, which are connected by a *Flexible Printed Cable* (FPC).

The most important part of the SLM is the display, which is located in the head (Fig. 2.2). Our model has a display of 1272×1024 px of $12.5 \times 12.5 \mu\text{m}$ each, and therefore a total active region of $15.9 \times 12.8 \text{ mm}$.

Starting from the back, we have a silicon substrate with an active circuit printed on it. Above, there are the pixel electrodes, used to apply the potential differences necessary to control the phase of the incident beam. The pixels and the regions around them are covered with the dielectric mirror, which is responsible for the high reflectivity of the display. Then we have the liquid crystal layer, and on the other side a common electrode covered by a glass substrate, which is the first thing hit by the laser beam.

The SLM brain is the controller, that contains all the electronics necessary to operate the display and to monitor the status of the entire device. One of its main tasks is to take the *8-bit* phase images generated by computer, corresponding to a specific amplitude pattern, and to use the *Look-Up Table* (LUT) to compensate for the non-linearity of the liquid crystal, applying the correct potential difference to each pixel.

After this technical description, we need to understand how the control of the potential differences applied across the pixels allows us to manipulate the intensity profile of the incident beam.

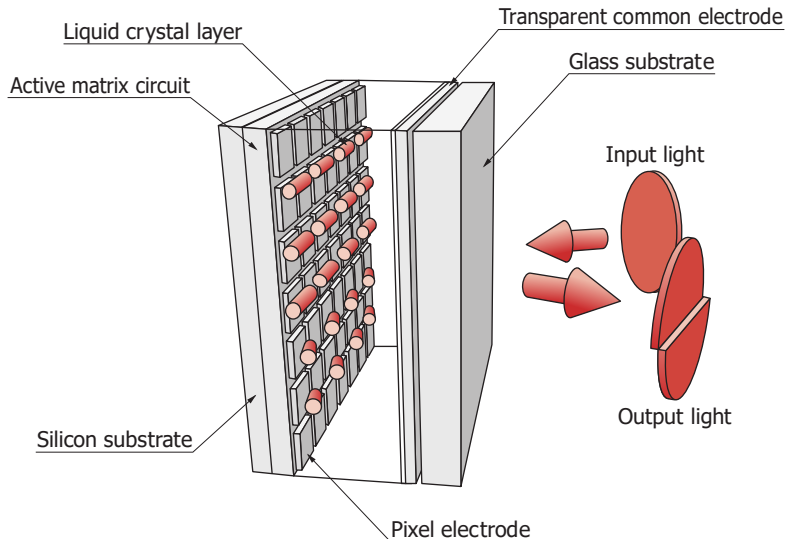


Figure 2.2: Illustration of the SLM display (taken from Ref. [24]).

2.2 From Potential Differences to Phase Shifts

The phase modulation is a consequence of a change in the orientation of the liquid crystal molecules inside the liquid crystal layer. These molecules have an elongated shape, which gives them uniaxial symmetry. This means that the liquid crystal molecules have an extraordinary axis with a refractive index n_e and two ordinary axes, perpendicular to the first one, with a refractive index n_o . Since the relation between the relative permittivity and the diffractive index is: $\varepsilon = n^2$, we can represent this situation with the following tensor:

$$\bar{\varepsilon} = \begin{pmatrix} \varepsilon_{\perp} & 0 & 0 \\ 0 & \varepsilon_{\perp} & 0 \\ 0 & 0 & \varepsilon_{||} \end{pmatrix} = \begin{pmatrix} n_o^2 & 0 & 0 \\ 0 & n_o^2 & 0 \\ 0 & 0 & n_e^2 \end{pmatrix} \quad (2.1)$$

In conclusion, the liquid crystal layer is *birefringent*.

In the typical SLM working conditions, the liquid crystal layer is in the *Nematic Phase* (Fig. 2.3a). In this phase, the liquid crystal molecules do not have a crystalline positional order, and are free to move as in a liquid. However their long axes are aligned, resulting in an anisotropic medium [19, p.185-190]. When no potential difference is applied, their alignment is perpendicular to the normal of the SLM display.

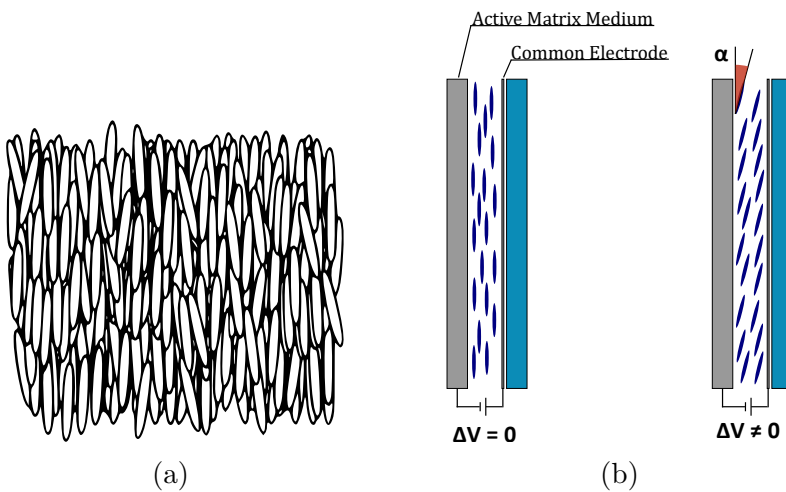


Figure 2.3: The liquid crystal layer in the *Nematic Phase* (a) and the effect of a potential difference on the liquid crystal molecules (b).

In these molecules, we have a dipole moment aligned with their long axes. When a potential difference is applied between the active matrix circuit and the common electrode, these dipoles try to align with the generated electric field to minimize their potential energy, resulting in a tilt of the molecules (Fig. 2.3b). This means that an incident beam with a wave vector \vec{k} and a linear polarization parallel to the display plane will perceive a different refractive index depending on the applied voltage. If the polarization of the incident beam is aligned with the

long axis of the liquid crystal molecules in the absence of an applied potential difference, the refractive index will be $n_e(\alpha)$, with values ranging from n_o to n_e . From the theory of the ellipsoid of refractive indices we know that [46]:

$$\frac{1}{n_e^2(\alpha)} = \frac{\cos(\alpha)}{n_e^2} + \frac{\sin(\alpha)}{n_o^2} \quad (2.2)$$

It is important to have an incident beam with the correct polarization in order to achieve the full dynamic range permitted by the SLM, and the highest possible diffraction efficiency, since the portion of the beam with a polarization different from the optimal one will experience the SLM display as a mirror.

The relation between the accumulated phase of the incident beam and the refractive index along the polarization axis is [25]:

$$\phi(V) = 2D \frac{2\pi}{\lambda} n_e(V) \quad (2.3)$$

where D is the width of the liquid crystal layer. We can see that the relation connecting the phase with the refractive index is linear, but the relation between the refractive index and the applied voltage is not. However, it is made so through the LUT.

The next step is to understand how these local phase shifts are used to generate the desired amplitude patterns.

2.3 From Phase to Amplitude

In Fig. 2.4 we can see a schematic representation of how an SLM is used in reflection mode (image inspired by Fig. 2.2 in [11]). A beam illuminates the desired portion of the SLM display. The wavefront of this beam is modified by the SLM and then focused by a lens called *Fourier Lens*. At the focus of this lens, we observe the desired amplitude pattern.

In this section, we will derive the relation between this amplitude pattern and the phase shifts applied through the SLM display.

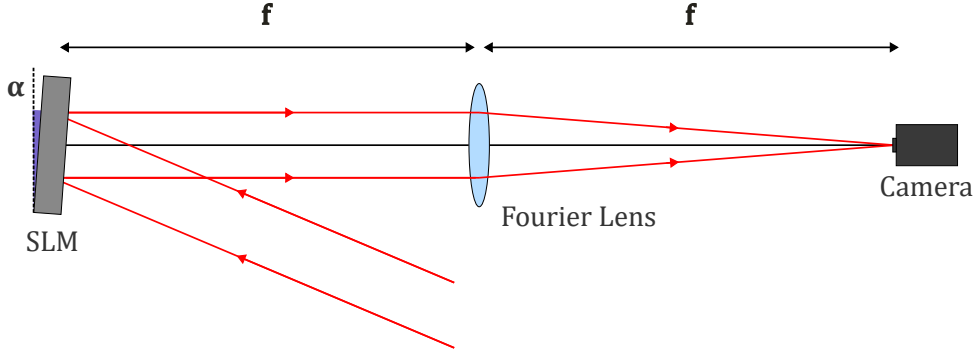


Figure 2.4: Schematic of the SLM used in reflection mode [47]. We have four elements: a beam, the SLM tilted by an angle $\alpha < 10^\circ$, a lens and a camera, which is necessary to observe the generated intensity pattern. The distance between the SLM and the lens must be equal to the focal length f of the lens.

2.3.1 Fourier Optics

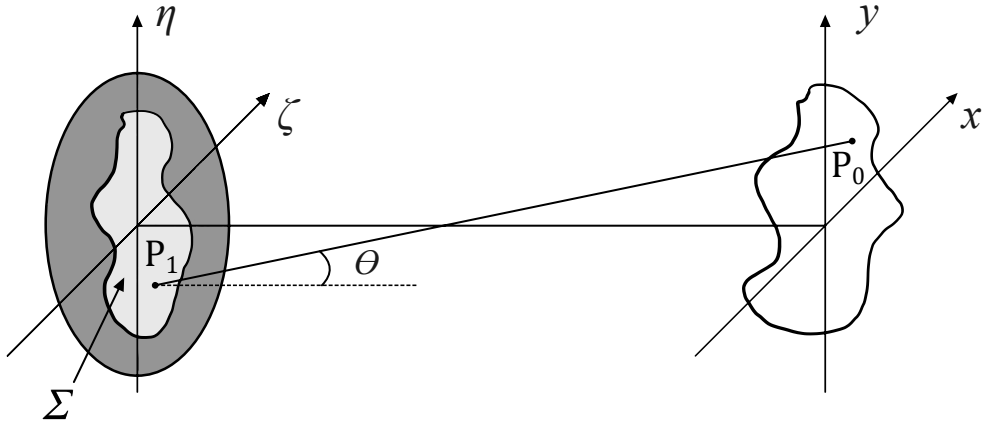


Figure 2.5: Diffraction geometry.

To model the system shown in Fig. 2.4, it is natural to use the formalism of *Fourier Optics* which uses phase and amplitude to describe light as a wave¹. To avoid coupling between the various components of the fields, we will consider only dielectric mediums which are linear and homogeneous. This implies that all the components of the electric field can be described by the following scalar wave equation:

$$\nabla^2 u(\vec{r}, t) = \frac{n^2}{c^2} \frac{\partial^2}{\partial t^2} u(\vec{r}, t) \quad (2.4)$$

The solution to this equation for a monochromatic beam is of the form $u(\vec{r}, t) = Re[U(\vec{r})e^{i\omega t}]$. If we substitute this into Eq. (2.4) we obtain the *Helmholtz Equation*:

$$(\nabla^2 + k^2) U(\vec{r}) = 0 \quad (2.5)$$

¹The discussion in this section extensively uses reference [19].

where $k = \frac{\omega n}{c} = \frac{2\pi n}{\lambda}$.

One of the solutions of Eq. (2.5), which fits particularly well for our situation, is the complex spherical wave solution, which describes point-like sources:

$$U(r) = \frac{U_0}{r} e^{ikr} \quad (2.6)$$

We will describe the SLM as an array of phase-modulating apertures. As a consequence of the *Huygens–Fresnel Principle*² we can describe the wavefront at a distance d from the aperture as a superposition of solutions like Eq. (2.6), in the following way [19, Chap. 3]:

$$U(P_0) = \frac{1}{i\lambda} \int \int_{\Sigma} U(P_1) \frac{e^{ikr_{01}}}{r_{01}} \psi(\theta) d\sigma \quad (2.7)$$

where $\psi(\theta)$ is called the *obliquity factor*. Its role is to take into account the difference in path length covered by the different wavelets due to their angle with respect to P_1 , and it is equal to: $\psi(\theta) = \cos(\theta) = \frac{z}{r_{01}}$. The explicit form of r_{01} is:

$$r_{01} = z \sqrt{1 + \left(\frac{(\zeta - x)}{z} \right)^2 + \left(\frac{(\eta - y)}{z} \right)^2} \quad (2.8)$$

which, under the *Fresnel Approximation*³, becomes:

$$r_{01} \approx z \left[1 + \frac{1}{2} \left(\frac{(\zeta - x)}{z} \right)^2 + \frac{1}{2} \left(\frac{(\eta - y)}{z} \right)^2 \right] \quad (2.9)$$

Now we are going to substitute this expansion into Eq. (2.7). r_{01} appears twice in the argument of the integral: once in the denominator, where we substitute it with the zero order of the expansion, and once in the exponent, where we also take the first order. We obtain:

$$U(x, y) \approx \frac{e^{ikz}}{i\lambda z} e^{\frac{ik}{2z}(x^2+y^2)} \int_{-\infty}^{\infty} \int_{-\infty}^{\infty} U(\zeta, \eta) e^{\frac{ik}{2z}(\zeta^2+\eta^2)} e^{-i\frac{2\pi n}{\lambda z}(x\zeta+y\eta)} d\zeta d\eta \quad (2.10)$$

Eq. (2.10) is called *Fresnel Diffraction Integral* and tells us how the wavefront at a generic distance z after an aperture is related to the wavefront at $z = 0$. We can also write this integral as a convolution integral:

$$U(x, y) = \int_{-\infty}^{\infty} \int_{-\infty}^{\infty} U(\zeta, \eta) h(x - \zeta, y - \eta) d\zeta d\eta \quad (2.11)$$

²The Huygens–Fresnel Principle states that every point of a wavefront is itself a source of spherical wavelets, and the secondary wavelets emanating from these points interfere with each other, creating a new wavefront.

³The Fresnel Approximation consists of a quadratic approximation of the phase factor inside the propagation integral. This is essentially a small-angle assumption, similar to the paraxial approximation.

where the kernel $h(x - \zeta, y - \eta)$ takes into account how propagation occurs in free space and corresponds to:

$$h(x - \zeta, y - \eta) = \frac{e^{ikz}}{i\lambda z} e^{\frac{ik}{2z}[(x - \zeta)^2 + (y - \eta)^2]} \quad (2.12)$$

Note that the finite size of the aperture is incorporated into the complex amplitude $U(\zeta, \eta)$.

2.3.2 Thin Lens

Another important element of the setup illustrated in Fig. 2.4 is the lens. To continue our discussion we need to understand how a lens acts on the wavefront of an incident beam and why we refer to the one in the figure as a *Fourier Lens*. We will use the thin lens approximation, which is valid if the thickness of the lens is negligible compared to its curvature radius. As a consequence of this approximation, we will not consider the translational effect of the lens, since its thickness is assumed to be negligible. This implies that the phase delay generated by the spherical lens can be written as:

$$\varphi(u, v) = kn\Delta(u, v) + k(\Delta_0 - \Delta(u, v)) \quad (2.13)$$

where Δ_0 is the maximum width of the lens and $\Delta(u, v)$ is a function which describes the thickness of a lens at a specific point. We are also considering $n_{air} \approx 1$.

$\Delta(u, v)$ can be decomposed into three components as we can see in Fig. 2.6, corresponding to the two sides of the lens and the central part, which can be neglected since we are using the thin lens approximation. We obtain [19, p.98]:

$$\Delta(u, v) = \Delta_L(u, v) + \Delta_C(u, v) + \Delta_R(u, v) \quad (2.14)$$

$$\Delta_{L,R}(u, v) = \Delta_{0L,0R} \mp R_{L,R} \left(1 - \sqrt{1 - \frac{u^2 + v^2}{R_{L,R}^2}} \right) \quad (2.15)$$

which, under the paraxial approximation ($|R_{L,R}| \gg |u|, |v|$), gives:

$$\Delta(u, v) \approx \Delta_0 - \frac{u^2 + v^2}{2} \left(\frac{1}{R_L} - \frac{1}{R_R} \right) \quad (2.16)$$

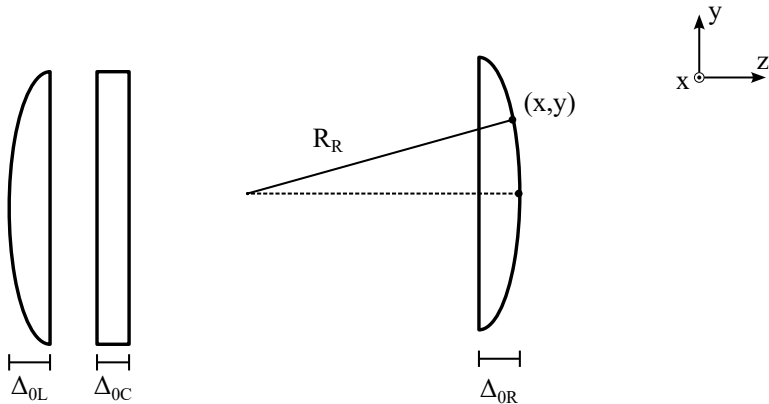


Figure 2.6: Decomposition of lens thickness into three parts, as indicated in Eq. (2.14).

From the *Lensmaker's Equation* we have that:

$$\frac{1}{f} = (n - 1) \left(\frac{1}{R_L} - \frac{1}{R_R} \right) \quad (2.17)$$

So we can finally evaluate the phase modulation applied by a lens under the thin lens approximation, which, neglecting the constant values becomes:

$$\varphi(u, v) = -\frac{k}{2f}(u^2 + v^2) \quad (2.18)$$

If we denote the complex amplitude of the wavefront just before and just after the lens $U_l(u, v)$ and $U'_l(u, v)$, respectively, we can relate them through the following equation:

$$U'_l(u, v) = t(u, v)U_l(u, v) = e^{-i\frac{k}{2f}(u^2 + v^2)}P(u, v)U_l(u, v) \quad (2.19)$$

which tells us how a lens modulates the phase of an incident beam, but gives no explanation as to why it is called Fourier Lens.

The term $P(u, v)$ in Eq. (2.19) defines the area of the aperture associated with the lens and corresponds to:

$$P(u, v) = \begin{cases} 1 & \text{if } u^2 + v^2 \leq R^2 \\ 0 & \text{elsewhere} \end{cases} \quad (2.20)$$

where R is the radius of the aperture.

2.3.3 Wavefront Propagation

At this point, we have all the necessary tools to determine the relation between the wavefront at the focus of the lens, $U_f(x, y)$, and the wavefront of the beam reflected by the SLM, $U_{SLM}(\zeta, \eta)$.

Starting from the focus of the lens, and using Eq. (2.10) we obtain:

$$U_f(x, y) = \frac{e^{ikf}}{i\lambda f} e^{\frac{ik}{2f}(x^2+y^2)} \int_{-\infty}^{\infty} \int_{-\infty}^{\infty} U'_l(u, v) e^{\frac{ik}{2f}(u^2+v^2)} e^{-i\frac{2\pi}{\lambda f}(xu+yv)} du dv \quad (2.21)$$

We rewrite $U'_l(u, v)$ according to Eq. (2.19), obtaining:

$$\begin{aligned} U_f(x, y) &= \frac{e^{ikf}}{i\lambda f} e^{\frac{ik}{2f}(x^2+y^2)} \int_{-\infty}^{\infty} \int_{-\infty}^{\infty} U_l(u, v) e^{-i\frac{2\pi}{\lambda f}(xu+yv)} du dv \\ &= \frac{e^{ikf}}{i\lambda f} e^{\frac{ik}{2f}(x^2+y^2)} \mathcal{FT}\{U_l(u, v)\}(f_x, f_y) \end{aligned} \quad (2.22)$$

Last equation shows us that the relation between the wavefront at the focus of a lens and the one incident on it is similar to a *Fourier Transform* in the spatial frequency domain, with frequencies: $f_x = \frac{x}{f\lambda}$ and $f_y = \frac{y}{f\lambda}$. This is why we call the lens a *Fourier Lens*.

The *Fresnel Diffraction Integral* can be rewritten as a convolution integral (Eq. (2.11)). Then, by using properties of the Fourier Transform⁴, we get:

$$\mathcal{FT}\{U_l(u, v)\}(f_x, f_y) = \mathcal{FT}\{U_{SLM}(\zeta, \eta)\}(f_x, f_y) \mathcal{FT}\{h(x - \zeta, y - \eta)\}(f_x, f_y) \quad (2.23)$$

where:

$$\mathcal{FT}\{h(x - \zeta, y - \eta)\}(f_x, f_y) = e^{ikz} e^{-i\pi\lambda z(f_x^2 + f_y^2)} \quad (2.24)$$

obtaining:

$$U_f(x, y) = \frac{e^{i2kf}}{i\lambda f} \mathcal{FT}\{U_{SLM}(\zeta, \eta)\}(f_x, f_y) \quad (2.25)$$

Finally, neglecting the constant phase factor, we get:

$$U_f(x, y) = \frac{1}{i\lambda f} \int_{-\infty}^{\infty} \int_{-\infty}^{\infty} U_{SLM}(\zeta, \eta) e^{-i2\pi(f_x\zeta + f_y\eta)} d\zeta d\eta \quad (2.26)$$

where $U_{SLM}(\zeta, \eta)$ takes into account the finite size of the SLM aperture.

At this point we have a mapping between the wavefront reflected by the SLM after the phase modulation (*Near Field*) and the wavefront in the focus of the Fourier Lens (*Far Field*). To obtain the desired amplitude pattern, we simply need to perform an Inverse Fourier Transform to retrieve the right phase modulation mask to be applied to the SLM display for a given near field amplitude. This is not trivial, and to obtain the phase pattern, we will need to use a particular *Phase Retrieval Algorithm*, which we will discuss in the next section.

Since we want to use these equations on a computer, it is useful to discretize Eq. (2.26). If we consider the pixels of the SLM as a matrix of point-like sources

⁴ $\mathcal{FT}\{f * g\} = \mathcal{FT}\{f\} \cdot \mathcal{FT}\{g\}$

with $N_\zeta \times N_\eta$ pixels, each associated with an area of $\Delta\zeta \times \Delta\eta$, we can express $U_{SLM}(\zeta, \eta)$ as:

$$U_{SLM}(\zeta, \eta) = U_{SLM}(n\Delta\zeta, m\Delta\eta) = A[n, m]e^{i\psi[n, m]} \quad (2.27)$$

The discrete version of the Fourier Transform is the *Discrete Fourier Transform* (DFT). To use it, we need to discretize the area associated with the focal point of the lens. As a consequence of the DFT, the number of points calculated in the far field is the same as the number of points used to discretize the near field, and so: $N_\zeta = N_x$ and $N_\eta = N_y$.

From the definition of the DFT⁵, we obtain:

$$e^{-i2\pi(f_x\zeta+f_y\eta)} = e^{-i\frac{2\pi}{f\lambda}(pn\Delta_x\Delta_\zeta+qm\Delta_y\Delta_\eta)} = e^{-i2\pi(\frac{pn}{N_x}+\frac{qm}{N_y})} \quad (2.28)$$

which implies that the dimensions of the calculated points in the far field are:

$$\Delta x \times \Delta y = \frac{\lambda f}{L_\zeta} \times \frac{\lambda f}{L_\eta} \quad (2.29)$$

The discretized intensity pattern is given by:

$$I_f[p, q] \propto \left| \sum_{n=0}^{N_x-1} \sum_{m=0}^{N_y-1} U_{SLM}[n, m] e^{-i2\pi(\frac{pn}{N_x}+\frac{qm}{N_y})} \right|^2 = |\mathcal{DFT}\{U_{SLM}[n, m]\}|^2 \quad (2.30)$$

By writing the SLM wavefront explicitly, it becomes:

$$I_f[p, q] \propto \left| \sum_{n=0}^{N_x-1} \sum_{m=0}^{N_y-1} A[n, m] e^{i\psi[n, m]} e^{-i2\pi(\frac{pn}{N_x}+\frac{qm}{N_y})} \right|^2 \quad (2.31)$$

We conclude this section with some examples of intensity patterns resulting from basic phase profiles applied to a circular aperture (Fig. 2.7).

In the first case, we calculate the phase pattern generated by a flat phase profile ($\psi[n, m] = 0 \ \forall n, m$). The resulting intensity pattern is the *Airy Disk* [19, p.477-479], which is the *Point-Spread Function*⁶ (PSF) of the system. The parameters of the Fourier Lens determine the size of the spot and thus set the diffraction limit of the system, which is the smallest achievable point. This also corresponds to the phase modulation of an ideal mirror. Next we consider a linear phase $\psi[n, m] = \alpha n + \beta m$, that acts as a diffraction grating, shifting the position of the spot. We can arrive at this conclusion also by considering the frequency-shifting property of the Fourier Transform⁷.

The last example is a quadratic phase of the form $\psi[n, m] = \alpha n^2 + \beta m^2$, which produces the same profile as that produced by a lens. This means that the focal point of the resulting system is in a different position, consistent with the observed intensity pattern.

⁵ $F[p, q] = \sum_{n=0}^{N_x-1} \sum_{m=0}^{N_y-1} f[n, m] e^{-i2\pi(\frac{pn}{N_x}+\frac{qm}{N_y})}$

⁶The Point-Spread Function is defined as the response of an optical imaging system to a point-like source placed at infinity.

⁷ $\mathcal{FT}\{e^{i2\pi\omega_0 t} f(t)\}(\omega) = \mathcal{FT}\{f(t)\}(\omega - \omega_0)$

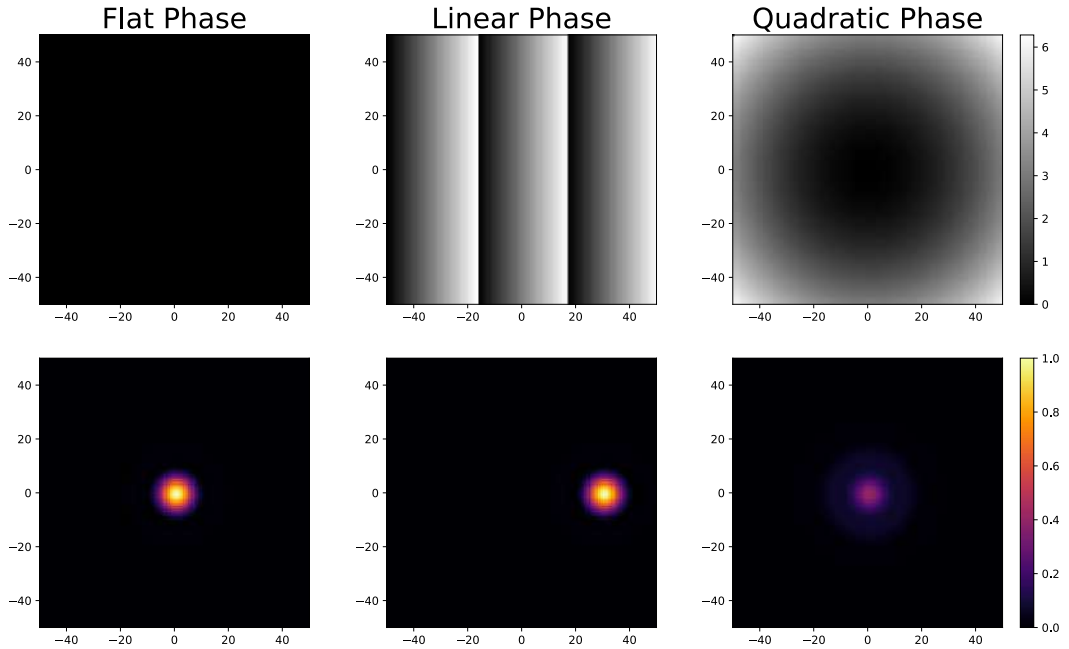


Figure 2.7: Intensity pattern generated by simple phase patterns.

2.4 Phase-Retrieval Algorithms

The main reason for using an SLM is the total freedom it offers to the user in generating the desired intensity patterns. To achieve this, we need to determine the local phase shift that must be applied to each pixel of the display.

From Eq. (2.31) we know that the relation between the near field and the far field is a DFT. This means that, in the same way it is possible to obtain the intensity pattern in the far field starting from amplitude and phase in the near field using a DFT, it is possible to do the inverse operation using an Inverse DFT. Unfortunately, things are not that simple.

Imagine having an intensity pattern that we want to reproduce in the far field using the SLM. If we want to perform the Inverse DFT to determine the phase mask to apply to the SLM in order to obtain such a pattern, we need a phase profile associated with it. Since the intensity profile in the near field is constrained by the laser beam incident on the SLM, we cannot use a random phase profile for the far field, nor can we consider solving the complex calculations derived from fixing the near field amplitude as well.

This leads us to the following question: How can we determine the phase pattern to apply to a known amplitude profile in the near field in order to generate the desired amplitude profile in the far field ?

This question is at the root of the *Phase Problem*⁸. We will solve this problem using a *Phase Retrieval Algorithm* called the *Gerchberg-Saxton Algorithm* and

⁸The *Phase Problem* [26, Cap. 7] arises from the loss of information about the phase that can occur when making a physical measurement, such as in our case, where we can only measure the amplitude patterns, with no information on the associated phases.

The algorithms used to solve this problem are called *Phase Retrieval Algorithms*.

one of its variants, the *Weighted GSA*. In the rest of this section, we will explain how these algorithms work.

2.4.1 The Gerchberg-Saxton Algorithm

The Gerchberg-Saxton Algorithm (GSA) [17] is an iterative algorithm that uses the *Fast Fourier Transform* (FFT) and the *Inverse Fast Fourier Transform* (IFFT) to move alternately between the near field and the far field until a convergence criterion or a specified number of iterations is reached.

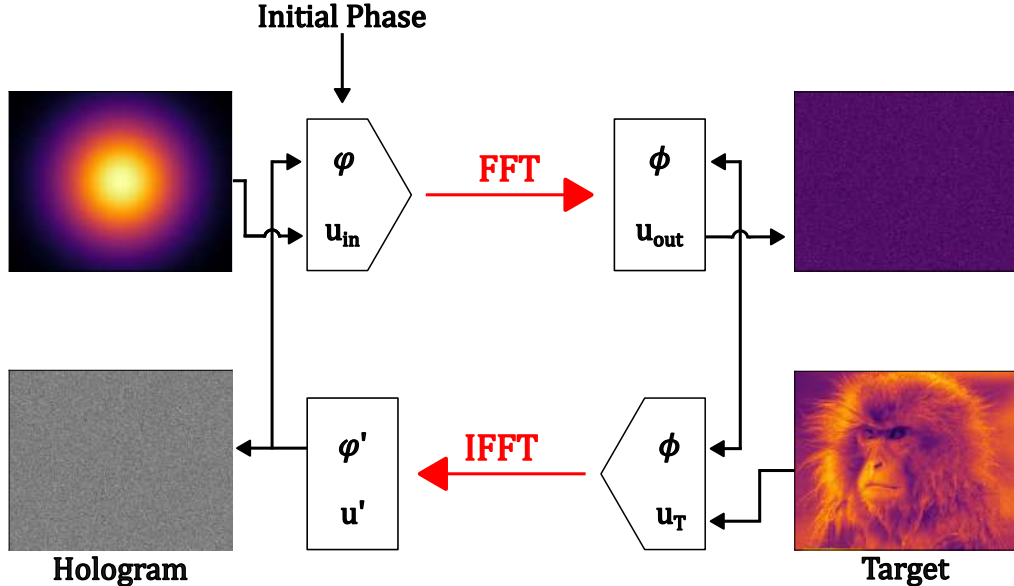


Figure 2.8: The flowchart of the Gerchberg-Saxton algorithm: the SLM domain is on the left, and the Fourier domain is on the right. The images on the sides correspond to the first iteration of the algorithm.

In Fig. 2.8 we present the flow chart of the algorithm. On the left side of the image, we have the wavefront in the near field, and on the right side, the wavefront in the far field. When using an SLM, these two areas are respectively referred to as the *SLM Domain* and the *Fourier Domain*. In our setup, the far field and the near field are at a distance of $2f$, where f is the focal length of the Fourier Lens. Another thing to keep in mind is that, since the algorithm is based on the FFT, the number of pixels in the target intensity pattern will be the same of the number of pixels of the SLM display, which is a constraint of the DFT (Eq. (2.30)).

The algorithm starts from the near field, considering a wavefront with an amplitude fixed by the laser source and a phase chosen randomly. The FFT is performed, obtaining the wavefront in the far field. We are not interested in its phase, so we will ignore it. We apply the first constraint by substituting the resulting amplitude with the target amplitude, and then perform the IFFT. At this point, we impose the second constraint by swapping the obtained near-field amplitude with the source profile. This operation concludes the first iteration.

We now have a wavefront in the near field with the correct amplitude and a phase that is closer to the one required to produce the target amplitude in the Fourier Domain.

This cycle is repeated until the desired convergence is reached or a specific number of iterations is done.

For this thesis project, we used the GSA for the generation of *Computer Generated Holograms* (CGH) corresponding to generic patterns, and a variation of the GSA, called the *Weighted GSA* [35], which is better suited for generating spot arrays. This variation of the algorithm improves the uniformity of the obtained intensity pattern through the use of the following weight function:

$$\mathcal{W}_{i+1,m} = \mathcal{W}_{i,m} \cdot \left(\frac{\mathcal{T}_{i,m}}{\mathcal{F}_{i,m}} \right)^p \quad (2.32)$$

where, i is the iteration index and m is the spot index. $\mathcal{W}_{i,m}$, $\mathcal{T}_{i,m}$ and $\mathcal{F}_{i,m}$ are the weight, the target amplitude, and the measured amplitude for a specific spot in a specific iteration, respectively. We can observe that for each iteration, if the measured amplitude of a spot is greater than the desired one, the weight of that spot is reduced, otherwise, it is increased. The parameter p modulates the behavior of the algorithm: larger values of p speed up convergence, while smaller values slow it down but result in greater uniformity.

We did not use the original version of the Weighted GSA, but a slightly modified version [32], which fixes the far-field phase after a desired number of iterations. This new constraint improves the convergence of the algorithm, though it sacrifices some efficiency.

Note that, since every point of the near field wavefront contributes to the far field wavefront, if we change the near field intensity pattern slightly (or if we are not very precise in measuring it) maintaining the same CGH, the far-field amplitude pattern would not be significantly affected.

We conclude this chapter by presenting the statistics related to the generation of CGHs for a 10×10 spot square array (Fig. 2.9) and for a generic image (Fig. 2.10) consisting of only two values, using a virtual environment. These simulations are performed assuming a uniform source for the generation of the square array and a Gaussian laser source for the other pattern.

The statistics in Fig. 2.9 are:

- *Inefficiency*: quantify the overlap between the obtained pattern and the target one;
- *Non Uniformity*:

$$n = 1 - u = \frac{I_{max} - I_{min}}{I_{max} + I_{min}} \quad (2.33)$$

where I_{max} and I_{min} are the maximum and minimum intensities of the obtained spot array, respectively.;

- *pkpk_error*: if we define r_i as the ratio between the obtained intensity and the target intensity of a spot, this parameter corresponds to the difference

between the maximum and minimum values, divided by the number of spots.

- *Standard Error*: relative to the standard deviation of the variable r_i .

We can see that the Weighted GSA produces more uniform arrays, although it is slightly less efficient. On the other hand, in Fig. 2.10, we observe that for generic images that are not spot-based, the GSA produces better uniformity compared to the Weighted GSA. In this case, uniformity is calculated as the mean of the absolute value of the difference between the target amplitude pattern and the obtained pattern over various iterations (normalized both to the same value). This provides a good estimate of uniformity since the target image consists of only two different values (0 and 1).

In conclusion, the Weighted GSA works better than the GSA with spot arrays, while it works worse for generic images. This is a consequence of the weight which indeed was thought to improve convergence in spot based arrays, where the used unit cells of the far field are limited and not so many like in the left pattern in Fig. 2.10.

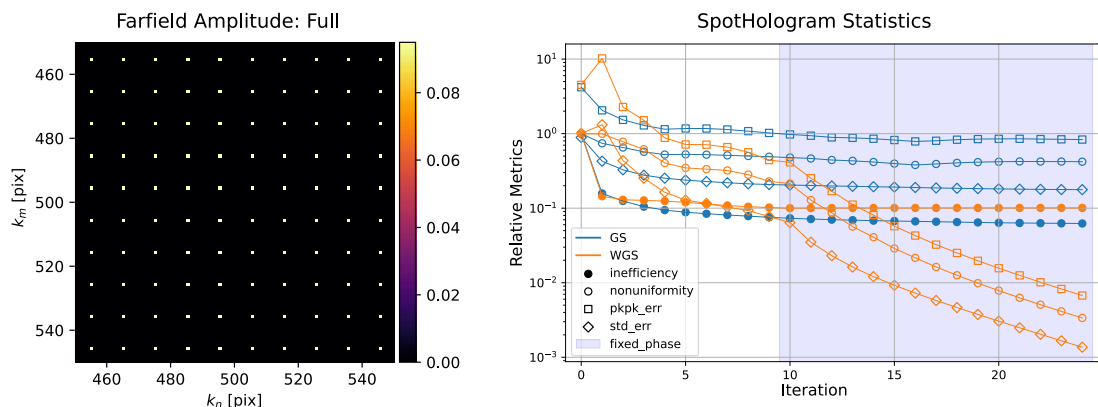


Figure 2.9: On the left, we have the simulated far field amplitude of a 10×10 spot square array obtained after 25 iterations of the Weighted GSA. On the right, there is a comparison of the statistics of the GSA and the Weighted GSA.

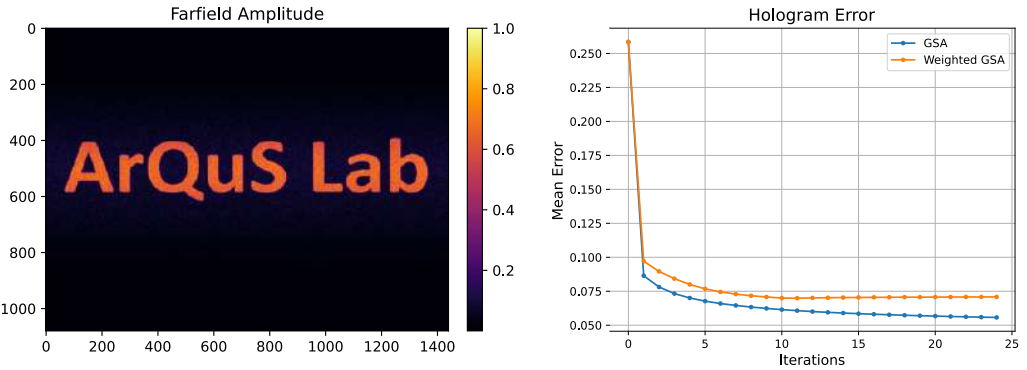


Figure 2.10: On the left, we have the simulated far field amplitude of an image representing the name of the laboratory where all this thesis work was done, obtained after 25 iterations of the GSA. On the right, there is a comparison of the uniformity of the GSA and of the Weighted GSA.

2.5 Aberrations Correction

Every optical system exhibits *Optical Aberrations*. These are caused by imperfect positioning and alignment of the elements that make up the setup, as well as by manufacturing imperfections in the optics.

Their presence is manifested through a distortion of the wavefront. In particular, referring to the schematic system presented in Fig. 2.4, they can be modeled as phase shifts in the SLM domain, which produce modulation of the amplitude in the Fourier Domain. The quality of an optical setup depends significantly on the presence of these effects and on our ability to correct and compensate for them. Since our source is a laser, we are interested only in monochromatic aberrations. The most common among them are [22]:

- *Defocus*: One possible cause of defocus is the incorrect positioning of lenses along the optical axis. This results in a shift of the focal plane with respect to the expected one, leading to a blurred image, even though its shape does not change significantly.
- *Astigmatism*: This is caused by elements that are tilted or not well aligned. These imperfections lead to different focal points along the optical axis, causing the wavefront to be distorted. As a result, the image becomes blurred in certain directions.
- *Coma*: One case where we can observe this effect is when the light source is not perfectly centered with respect to the optical axis. The typical symptom of this aberration is the characteristic comet-like tails, caused by the fact that the focal point of the wavefront is spread in the direction perpendicular to the optical axis.
- *Spherical Aberrations*: These arise from spherical surfaces that converge light rays to different positions depending on the radial distance from the optical axis. They are typically caused by manufacturing imperfections and are common in non-achromatic lenses with a small curvature radius, which

is necessary for achieving short focal lengths. This leads to blurring and loss of detail, especially at the periphery of the image.

The phase shift in the near field associated with various types of aberrations can be generated using *Zernike Polynomials* [33]. The basis identified by these polynomials can also be used to decompose the phase shift profile of a system, providing a better understanding of the types of aberrations that affect it.

In Fig. 2.11, we can observe the consequences of the described optical effects on the PSF of the system simulated in Fig. 2.7. These patterns are obtained by adding the phase shift calculated using Zernike Polynomials to the Flat Phase case shown in the cited figure.

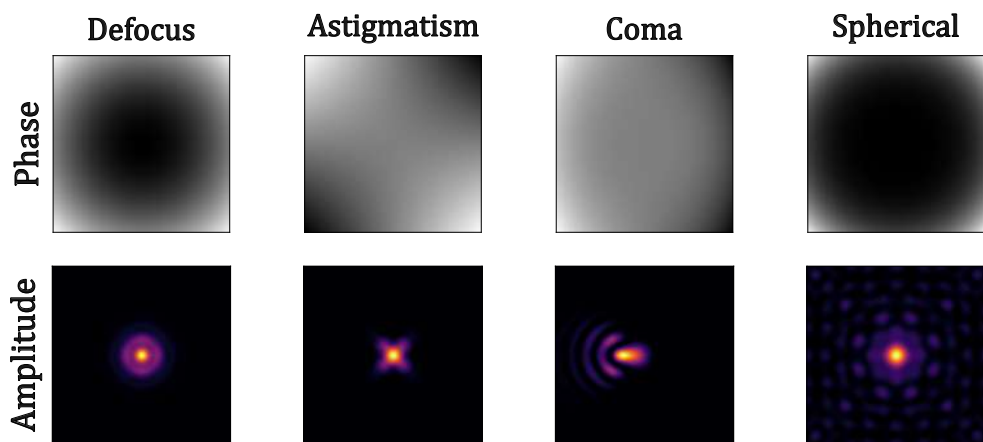


Figure 2.11: Effect of Various Types of Aberrations on the PSF of the System (the Airy Disk). Notice the similarity between the phase profile and the corresponding intensity patterns for both the quadratic phase and the defocus aberration.

In the same way that we applied these phase patterns to introduce aberrations in our system, they can also be subtracted to compensate for them. To do this, we need to calculate the phase shift profile produced by the aberrations affecting our system.

To compute these phase profiles, we use a method based on phase-shift interferometry.

2.5.1 Phase-Shift Interferometry

The method we used to calculate the phase profile to compensate for aberrations is based on phase-shift interferometry [8]. This procedure relies on the idea that if we take two coherent beams traveling through an optical setup, they will acquire different phases depending on their coordinates in the transverse plane. The relative phase between them will be related to the position of the fringes in the resulting interference pattern.

We can gain a better understanding by thinking of *Young's Double-Slit Experiment* [15, p.59-61]. If the incident wave is a plane wave, we will see an interference pattern with the main peak centered in the transverse plane between the two slits.

If we change the phase of the wavefront at one of the two slits, the position of the fringes will change depending on the relative phase between them.

In our case, these phase shifts are produced by aberrations. Therefore, we can look at the shifts in the fringe positions to obtain a complete characterization of the phase delays introduced in our setup by aberrations, which can then be compensated by subtracting the obtained phase pattern.

To implement this procedure, the first step is to divide the SLM display into non-overlapping squares. We will call these regions *Superpixels*, which are essentially 2D slits. If we set the amplitude to zero for all the superpixels except one, the intensity pattern in the Fourier domain will be a 2D *sinc* function, as expected from a square aperture [19, p.475–477]. The extent of the main lobe of this profile will depend on the dimensions of the superpixel. If we 'switch on' another superpixel, we will observe an interference pattern. The section of these two intensity profiles is the same as those obtained from a single slit, which is a *sinc* function, and from two slits, which is a *sinc* function multiplied by a cosine with a higher frequency, respectively [15, p.120-122]. These two situations are represented in the following figure:

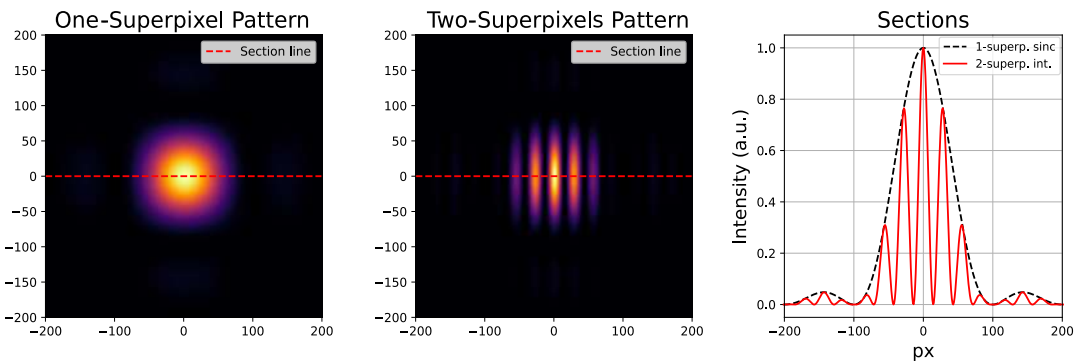


Figure 2.12: One and Two Superpixel Patterns. In this case, the relative phase between them is zero. The fringe density becomes higher as we move the two superpixels closer. In the plot on the right, we can see that the section of the resulting intensity pattern is the same as that obtained in the double-slit case.

If we change the phase of one of the two superpixels, we will observe a shift in the fringe positions, as illustrated in Fig. 2.13. The intensity at the center of the Fourier Domain, corresponding to the position of the red dots in the center of the three bottom figures, exhibit the trend described by the equation below [8]:

$$I_0 \propto |E_t|^2 + |E_r|^2 + 2|E_t||E_r|\cos(\Delta\phi) \quad (2.34)$$

where E_t and E_r are the values of the main peaks of the *sinc* profiles generated by the two superpixels, called target and reference superpixels, respectively, and $\Delta\phi$ is the relative phase between them.

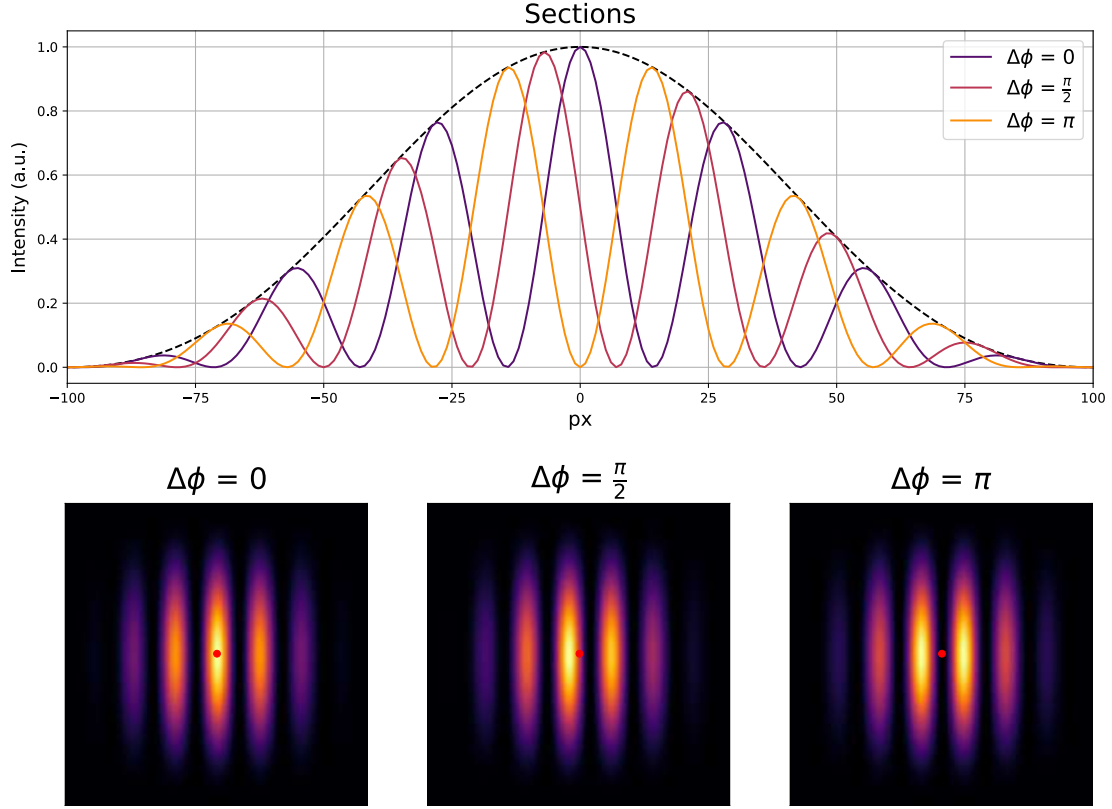


Figure 2.13: Shift in the fringe positions due to different values of the relative phase, $\Delta\phi$.

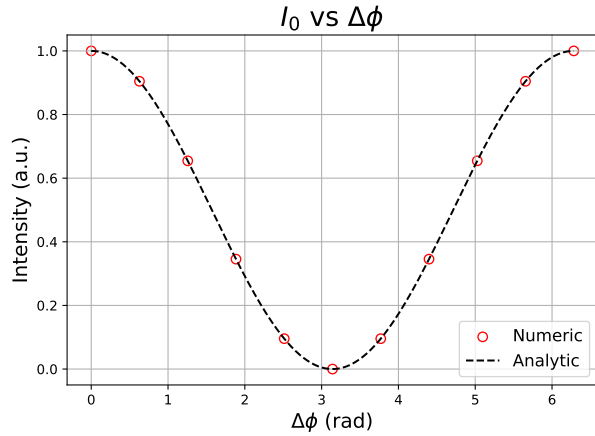


Figure 2.14: Normalized intensity at the center of the Fourier domain for different values of $\Delta\phi$. The red dots are obtained by taking the amplitude values at the center of the Fourier domain for various phase shift values, including those from the three bottom figures in Fig. 2.13, while the dashed black line is a plot of Eq. (2.34).

To implement the algorithm, we first choose a superpixel as a reference (*Reference Superpixel*), which will set the phase offset and the amplitude scale for the evaluations of the wavefront. We then scan all the other superpixels one by one,

observing the resulting interference pattern. In this way, we can evaluate both the relative phase between all the superpixels and the reference one, as well as the amplitude, thereby obtaining a complete characterization of the wavefront. In Fig. 2.15, we can see an example of the output of this procedure obtained in our setup.

At this point, we can simply subtract the phase pattern obtained using the SLM, which compensates for aberrations and reduces the distortion of the wavefront. Through this correction, we can improve the quality of our optical system and, hopefully, achieve diffraction-limited performance.

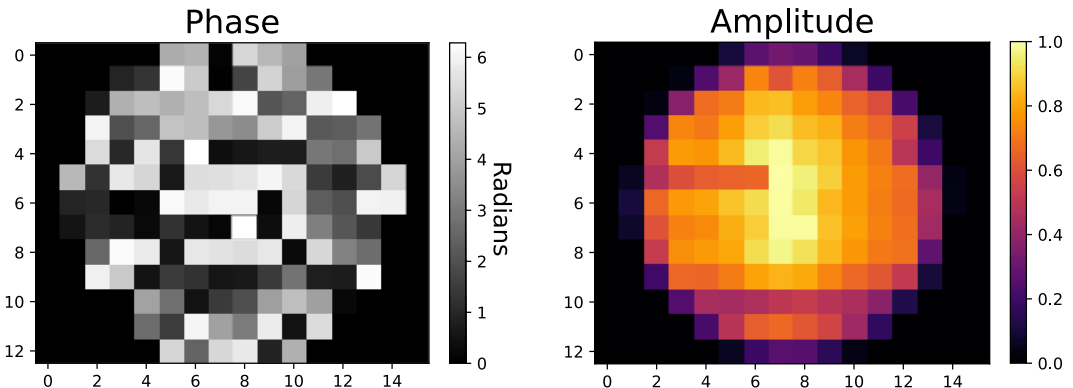


Figure 2.15: Output of the algorithm to evaluate the aberration affecting our optical setup. The camera was positioned at the focus of the Fourier lens. The superpixels were square-shaped with a side length of 80px (1mm). The reference superpixel is the one located at coordinates (8, 7) in the superpixel grid.

This method can also be used if there are other elements between the SLM and the camera, as it only relies on analysing the interference pattern and calculating the correction to apply to the wavefront in order to maximize the fringe values at the center of the interference pattern. Furthermore, the interference signal can be generated by a laser source or by atom fluorescence, allowing us to correct the aberrations directly in the plane of the atoms [8].

However, we must consider that if there are other optical elements between the point where we want to correct the aberrations and the camera, we will also compensate for them, since the algorithm creates a phase mask that is optimal for the aberrations in the camera plane. If these optics introduce too many defects, we risk to overcompensate aberrations, increasing the distortion of the wavefront in the target atom plane.

We conclude this section, and the relative chapter, with some considerations. The first is related to the accuracy of the calculated wavefront. It can be improved by reducing the dimensions of the superpixels, but obviously, "the blanket is too short to cover everything". Smaller superpixels mean smaller portions of the laser beam power which reaches the far field, and bigger interference patterns. This sets a lower bound for their dimensions, as there must be enough power to resolve the intensity profile, and the interference pattern must also fit within the camera sensor.

Another important consideration, and likely the biggest limitation of this method, is that the calculated corrections are local. This means we must repeat the process each time we want to move our patterns to another region of the Fourier Domain. Additionally, if our patterns are too large, the edge regions will not experience the effects of the correction, which could risk to degrade their quality. These corrections are also time-independent, meaning they can only account for static aberrations.

In conclusion, the SLM can be used to compensate for static aberrations in optical systems, and this method provides a simple and effective way to utilize this feature.

Chapter 3

Experimental Setup and Results

We will start this chapter with a brief description of the *Titanium-Sapphire Laser* used in the setup. After that, we will discuss the optical path built for the SLM. Then, we will explain the various procedures to follow in order to achieve the best performance from the SLM, such as blocking the zero-order of diffraction and achieving a diffraction-limited spot. This is done through a Python library called *slmsuite*, which allows us to control the SLM via the computer.

We will conclude the chapter by presenting some results and making relevant considerations regarding the generation of spot arrays, discussing their statistics for various parameters and geometries. We will also present and discuss some images that are not spot-based, which present a peculiar phenomenon.

3.1 Titanium-Sapphire Laser

The laser we used is the *Matisse CS* from *Spectra-Physics*, a Continuous Wave (CW) solid-state Ti:Sapphire laser [43, 34]. This laser is pumped by a green diode laser at 532 nm, the *Millennia eV*, that is also a CW laser. The pump can produce up to 25 W of power, which allows the Matisse CS to output more than 7.2 W for wavelengths in the range of 750 – 800 nm (as declared by the manufacturer). The temperature of the Millennia eV is maintained at 20° through a chiller, which also cools the crystal of the laser. The emission bandwidth of the Matisse CS is 668 – 1068 nm, that is the typical range for a Ti:Sapphire laser, with a declared linewidth of less than 35 kHz. We use this setup for wavelengths around 759 nm (395 THz), which, as mentioned in the first chapter, is the magic wavelength for the clock transition (${}^1S_0 \rightarrow {}^3P_0$).

The maximum output we achieved with our device, with the pump operating at 25 W, was 7.9 W for $\lambda = 759.7$ nm.

Since operating at the maximum capacity of the pump reduces its lifespan, we typically use it at 10 W. With this power, we measured an output from the Matisse CS of 1.04 W for $\lambda = 759.7$ nm, which is the lowest possible power required to properly set up the laser each time we switch it on, ensuring a sufficiently stable output.



Figure 3.1: On the left is a picture of the *Matisse CS*, while on the right we can see the compact form with the *Millenia eV*, which is the same setup present in the laboratory (images taken from [34]).

3.2 Experimental Setup

Now we are going to discuss the experimental setup built for this thesis project. Its diagram is illustrated in the following picture.

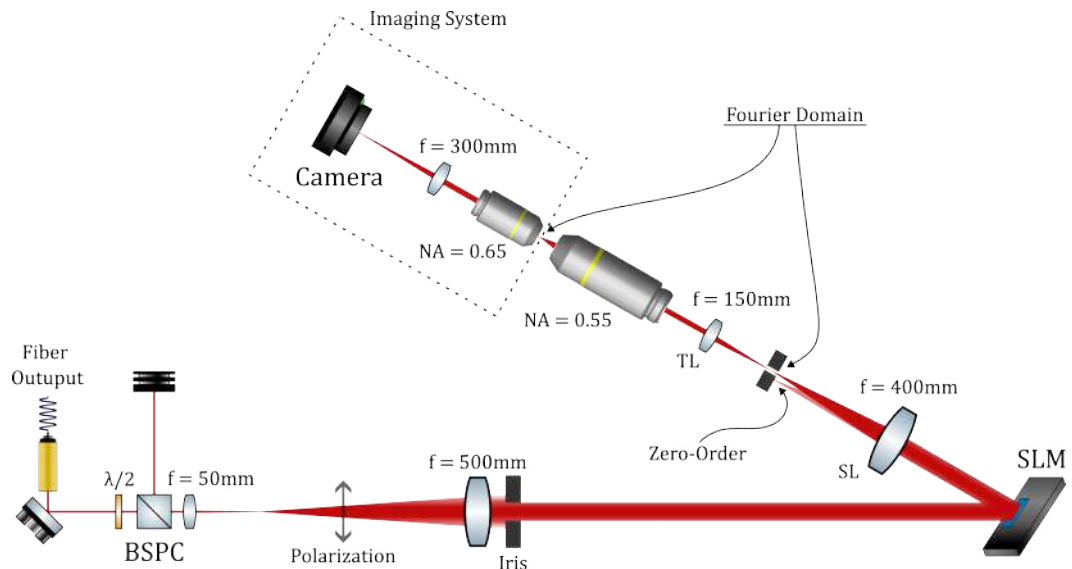


Figure 3.2: The diagram of the optical path.

We will start the description of the setup from the fiber, used to guide the laser beam from the Matisse CS table to another one, where the setup is built. The fiber is connected to a collimator, from which we get a laser beam with a radius of $w_0 \approx 0.95\text{mm}$. The power output was typically around 10 – 20 mW, in order to ensure a sufficiently visible beam, even in the regions where it is expanded. The first thing we need to do is clean the polarization of the beam. To do this, we use a *Half-Wave Plate* and a *Beam Splitter Polarizing Cube*. In this way, we obtain a linear polarization in transmission with the correct direction needed by the SLM. By rotating the mounting of the Half-Wave Plate, we can adjust the ratio between the transmitted and reflected power. The reflected fraction of the beam is blocked by a beam dump, but this can be replaced by a photodiode to moni-

tor and stabilize the power of the beam using a *Proportional-Integral-Derivative* (PID) control.

After the cube, we have a telescope, necessary to expand the beam to the desired dimension. The expected magnification was $M_{th} = 10$, but the measured value is $M_{meas} \approx 12.5$, producing a beam waist of $w_0 \approx 11.5 \pm 0.5\text{mm}$. To evaluate the magnification produced by this telescope, we measured the demagnification produced by another telescope, already characterized, and then placed it after the one in the setup. This allows us to have a beam small enough to be captured by the sensor of our camera and to fit it for determining its dimensions.

On the other side of the telescope, we placed an iris with a radius set between 5mm and 6.5mm to cut away the tails of the Gaussian beam. This way, we obtained a beam profile reasonably flat, with a diameter slightly smaller than the short edge of the SLM display. This profile is the most functional for using the SLM, as it provides a good compromise between the 'flatness' of the amplitude and the power loss due to the circular cutting.

Then the beam illuminates the SLM. Since we want to operate it in reflection mode, we need to determine the optimal configuration to avoid overlap between the optical elements associated with the incident beam and those of the reflected one. To do this, it is sufficient to tilt slightly the SLM with respect to the incident beam. The angle between the normal of the display and the incident beam must be smaller than 10° to avoid significant degradation in the performance of the SLM due to misalignment between the polarization of the beam and the one desired by the SLM [47]. In our setup, we used an angle $\alpha \sim 7^\circ$, which is the smallest angle possible to avoid overlap in our configuration.

To align the beam with the SLM display, we use the following procedure:

First we shrink the iris, reducing the diameter of the beam. This allows us to obtain a rough starting point by eye. Then, we restore the beam's original size and apply a diffraction grating with the SLM, but only in a circular region at its center. The diameter of this region must be slightly smaller than the short side of the display. The correct alignment is achieved when we obtain a perfectly symmetric circular crown around the zero-order (Fig. 3.3). This indicates that the entire incident beam is inside the SLM display and well aligned with the center of the display.

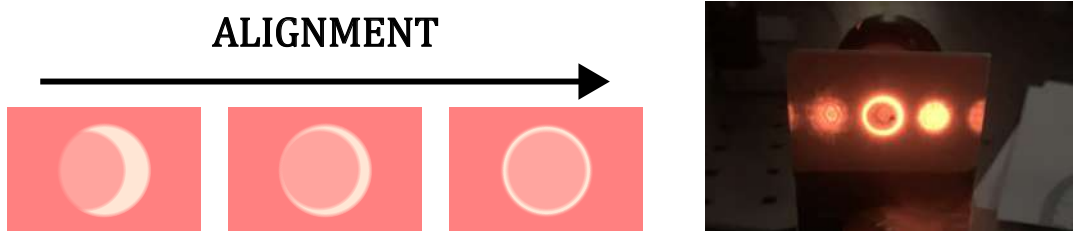


Figure 3.3: Patterns observed during the alignment procedure of the SLM around the position of the zero-order. The photo on the left was taken in the laboratory, showing the discussed pattern on a Detector Card.

The optical elements following the reflection on the SLM will be aligned with the first order generated by it, that is separated from the zero-order by a diffraction grating that creates an angle of 0.5° between them. We will discuss this in more detail in the next section.

The next optical element on the path is the *Scan Lens*, with a focal length of $f_{sl} = 400\text{mm}$, corresponding to the Fourier Lens discussed in the previous chapter. The distance between the lens and the SLM is equal to f_{sl} , ensuring that the relationship between the wavefront reflected by the SLM and its focus matches the one described by Eq. (2.31). At the focus of the Scan Lens, we place an iris to completely filter out the zero-order from our patterns.

The path continues with a *Tube Lens* of focal length $f = 150\text{mm}$, followed by the *Mitutoyo Plan Apo 50x*, a microscope objective with $NA = 0.55$. With these two elements, the pattern generated at the focus of the Scan Lens is demagnified by a factor of $M_{Mit} = 35 \pm 0.6^1$.

Obviously, the generated patterns are too small to be properly observed with our camera, which has pixels of $3.45 \times 3.45 \mu\text{m}$. To observe them, we placed another microscope objective after the first one. The model used is the *PLN 40x Olympus*, that has an $NA = 0.65$, and thus a diffraction limit smaller than that of the Mitutoyo Plan Apo 50x, allowing us to resolve any pattern produced with it. This objective has a magnification value of $M_{Ol} = 71.23 \pm 1.14$ (with a tube lens of focal length $f = 300\text{mm}$). This value was calculated using the *1951 USAF Resolution Target* as a reference.

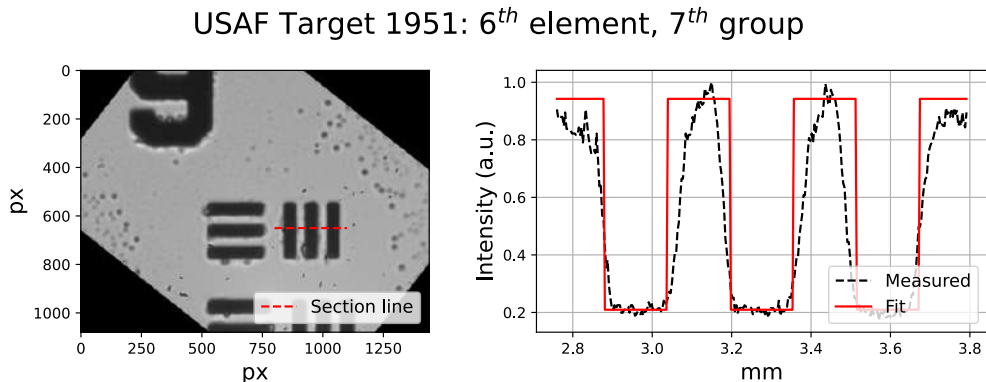


Figure 3.4: In this figure, we can see one of the images taken of the *1951 USAF Resolution Target*, specifically the 6th element of the 7th group, which corresponds to 228 lp/mm. From this image, we extracted a section and fit it with a square wave. Using the frequency of the square wave, we extrapolated the magnification of the objective. This procedure was repeated for several images, and the obtained values were averaged to yield the final result.

At this point, we reach the last element of the setup: the camera, which in our case is the *ThorCam CS165MU*.

¹This value is obtained as the ratio between the best spot observed at the focus of the Scan Lens and the best spot observed at the focus of the objective. It can only be evaluated a posteriori, as we need the magnification value of the PLN 40x Olympus to determine the spot size at the focus of the Mitutoyo Plan Apo 50x.

We conclude this section with photos of the setup taken in the laboratory.

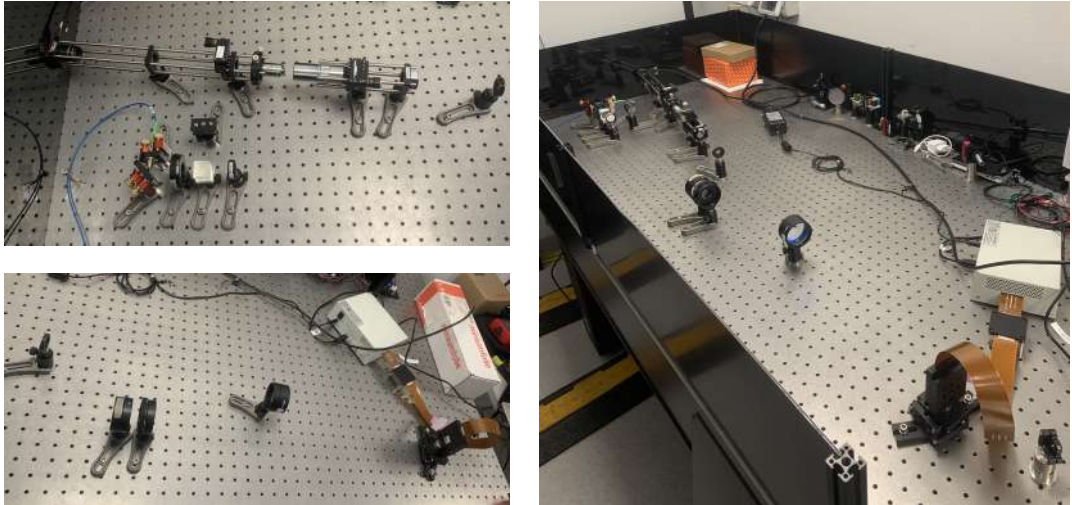


Figure 3.5: Some pictures of the setup taken in the lab, showing different regions (on the left) and the entire optical path (on the right).

3.3 Working with the SLM

In this section, we will discuss all the necessary calibrations and procedures required for the proper use of the SLM setup. These require a complete control over the SLM, but also a way to observe the resulting patterns, which is done using the camera. This control is achieved by computer, using a Python library called *slmsuite* [45], which allows us to manage both simultaneously. This library enables us to perform basic tasks such as applying phase patterns to the SLM and reading the head and controller temperatures, as well as more sophisticated operations like aberration correction routines and feedback loops. Additionally, this library contains all the necessary scripts to communicate with devices that use *DLL* (Dynamic-Link Library) files.



Figure 3.6: Logo of the *slmsuite* library ([45]).

When we were working on this project, the Hamatsu models had not yet been implemented in the library, so we wrote all the necessary scripts by ourselves.

This gave us a better understanding of the SLM's functionality and potential. We also encountered some issues with the scripts related to the control of the ThorCam, but after some adjustments, they started to work properly.

3.3.1 Lookup Table

In an ideal device, the minimum potential difference that can be applied to each pixel corresponds to a zero phase shift, while the maximum value corresponds to a 2π phase shift, connected by a linear trend. However, this is not the case with real devices.

For them, we need to find a mapping between all the possible potential difference values that can be applied and the resulting local phase shifts. A complete understanding of these relations constitutes the *Lookup Table* LUT of the device. After measuring it, we need to feed the data to the device, which will use them to determine the potential difference to apply to each pixel in order to produce the desired local phase shift.

Our SLM was sent by Hamamatsu with a test sheet, showing that its characteristic function was perfectly linear for all the wavelengths for which the model was designed. This sheet also included the fraction of the total potential difference range, associated with the interval $[0, 255]$, that we must use for a specific wavelength in order to cover the range $[0, 2\pi]$. We cannot change the LUT functional form, so we trust Hamamatsu on its linearity. However, since we can choose the fraction of the total potential difference range, we decided to test whether the value provided by Hamamatsu for our wavelength was correct. This is important because an incorrect value can affect the diffraction efficiency, and consequently, how much of the total energy of the incident beam the SLM can direct toward generating the desired patterns. The diffraction efficiency, η , is obtained as the ratio between the power of the first order and the total one.

To understand the relation between the used range and the diffraction efficiency of the device, but also to determine its correct dimension for a specific wavelength, we first need to make some considerations.

We take into account a system like the one shown in Fig. 2.4, where we have a laser source with a certain wavelength λ . We apply a diffraction grating using the SLM to shift the position of the spot generated in the Fourier Domain, which corresponds to a linear phase profile (Fig. 2.7). If we zoom in on this linear ramp, we will notice that, since the number of pixels is finite, it will resemble a stair. We define two parameters related to these ramps [40]:

- N : the number of steps into which the ramps are subdivided, which can be seen as the resolution of the diffraction grating.
- M : the height of the ramp in units of 2π .

In Fig. 3.7, we simulate the effects of a diffraction grating for different values of these two parameters on the resulting spots. For simplicity, we use a square

mask instead of a circular one, resulting in patterns that are not Airy disks but sinc functions.

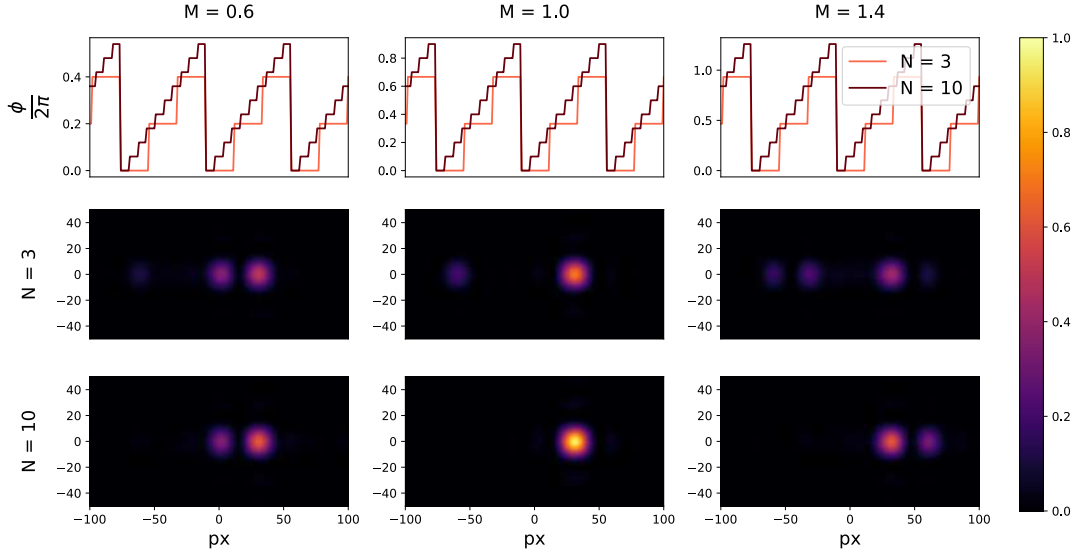


Figure 3.7: Resulting patterns for different values of the parameters N and M . The three top images show a section of the diffraction gratings used to generate the patterns.

As we can see in Fig. 3.7, larger values of N , and thus higher resolution of the ramp, generate higher diffraction efficiency. Regarding the parameter M , the best case occurs when $M = 1$, which corresponds to using only the range $[0, 2\pi]$ [19, p.211–213].

We can also solve these situations analytically, finding that the diffraction efficiency, $\eta(N, M)$, of the diffraction grating is [40, 1]:

$$\eta(N, M) = \left(\frac{\sin\left(\frac{\pi}{N}\right)}{\pi} \right)^2 \left(\frac{\sin(\pi(M-1))}{\sin\left(\frac{\pi}{N}(M-1)\right)} \right)^2 \quad (3.1)$$

From this formula, we see that $\eta(N, M)$ is independent of the diffraction angle and wavelength. In Fig. 3.8, we plot it as a function of M for different values of the parameter N . We observe an asymptotic behavior as $N \rightarrow \infty$, which gives $\eta(M = 1) = 1$.

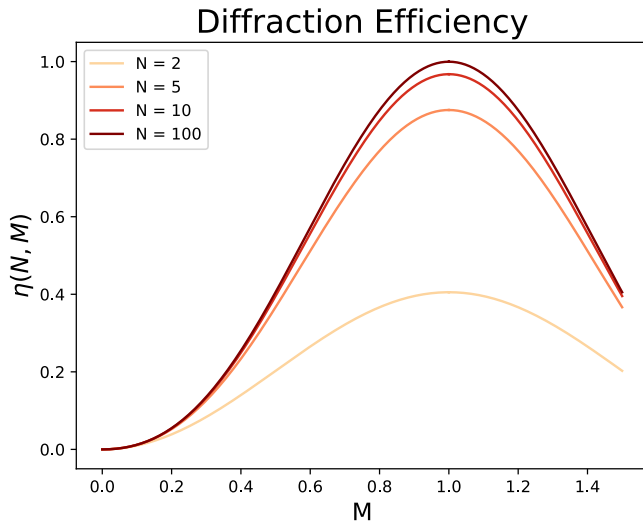


Figure 3.8: $\eta(N, M)$ as a function of M for different values of N .

This plot shows that for every value of N , the maximum efficiency occurs at $M = 1$, which corresponds to a phase range spanning from 0 to 2π . This is why we need to find the correct fraction of the different potential values to use, as it will maximize the efficiency. To determine this, it is enough to fix a diffraction angle and measure the diffraction efficiency for different interval dimensions. The optimal interval will be the one associated with the highest diffraction efficiency. The necessary measurements had been taken, and the results are plotted in Fig. 3.9.

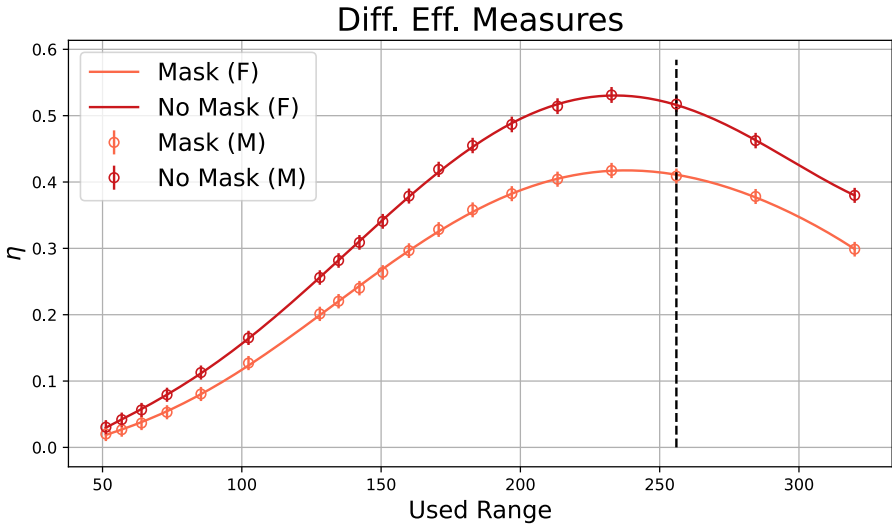


Figure 3.9: Measurement (M) and fit (F) of the diffraction efficiency for different ranges. The measurements were taken using a diffraction angle of 0.5° . In the measurements with the mask, we used a circular region with a diameter equal to the short side of the SLM display. For the fit, we used a polynomial function. The range corresponding to the maximum values of the fitted functions was 234 for the case without the mask, and 238 for the case with the mask. We consider their mean value, 236, as optimal.

In the measurements for ranges larger than 256, any value higher than that is set 255, the maximum possible value.

From the fit in Fig. 3.9, we determine an optimal value of 236. This value is passed to the SLM converted into a wavelength λ' using the parameter "*wav_design_um*" from slmsuite, which has the following relation with the source wavelength λ :

$$\lambda' = \lambda \frac{256}{236} \quad (3.2)$$

In our case, this wavelength corresponds to $\lambda' = 823$ nm. The obtained value is different from the one declared by Hamamatsu, which was 201. This difference is likely due to variations in the environmental conditions under which the measurements were conducted.

3.3.2 Vendor Phase Correction

Another thing provided by Hamamatsu is a phase correction mask to compensate for the deviation from the flatness of the SLM display. This correction is calculated using a Michelson interferometer and is provided for different wavelengths. The most suitable for us is the one at 760 nm.

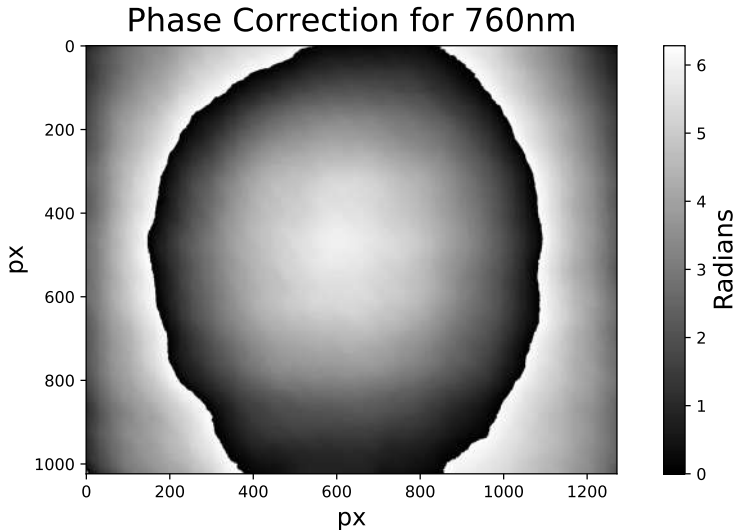


Figure 3.10: Phase correction provided by Hamamatsu for a wavelength of $\lambda = 760$ nm.

On the test sheet, it is stated that the *PV* (Peak-to-Valley) value before correction for a wavelength of 785 nm is $PV = 1.741\lambda$, and after correction, it is $PV = 0.034\lambda$, corresponding to a reduction of 98%. We can expect the same reduction using the correction shown in Fig. 3.10.

However, this phase correction can be bypassed, as we can directly correct the aberrations of the entire system, which will also take into consideration the deviation of the SLM display from a perfect flat surface.

3.3.3 The Zero-Order

A typical problem when using an SLM to generate patterns with phase-only modulation is the presence of zero-order of diffraction. This occurs because the regions between the pixels are not active, so the part of the beam that hits these areas will be reflected as it would by a normal mirror. Our model has a *fill factor*, which represents the portion of the display that is active, of 96.8%.

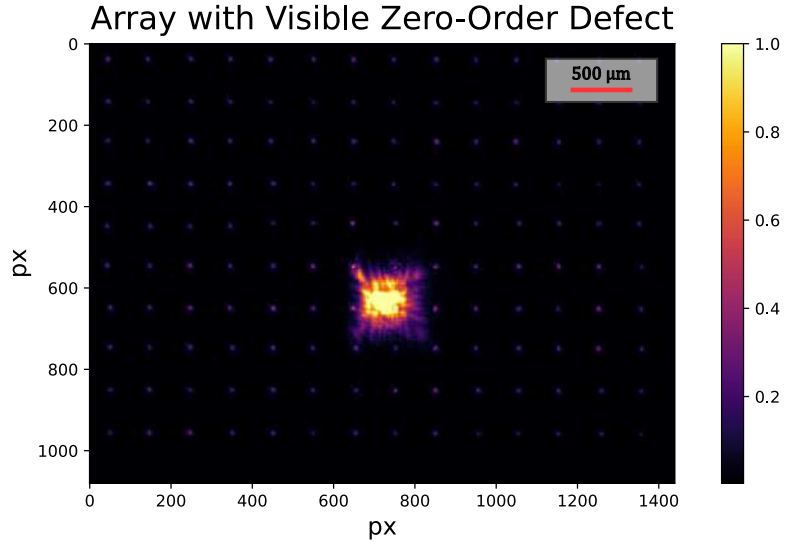


Figure 3.11: An image taken at the focus of the scan lens, where we can observe the presence of the zero-order of diffraction, superimposed on a square array.

There are two basic ways to avoid the presence of this defect in our pattern: we can cover it (as we can observe in the arrays presented in [44]) or we can move our patterns away from it [27, 54], which is the approach we used.

As showed in Fig. 3.2, we align the beam resulting from the reflection on the SLM with the first order, which is shifted by an angle of 0.5° with respect to the zero order, and then we filter it out completely using an iris placed at the focus of the Scan Lens.

We chose this angle after considering the diffraction efficiency for different working angles.

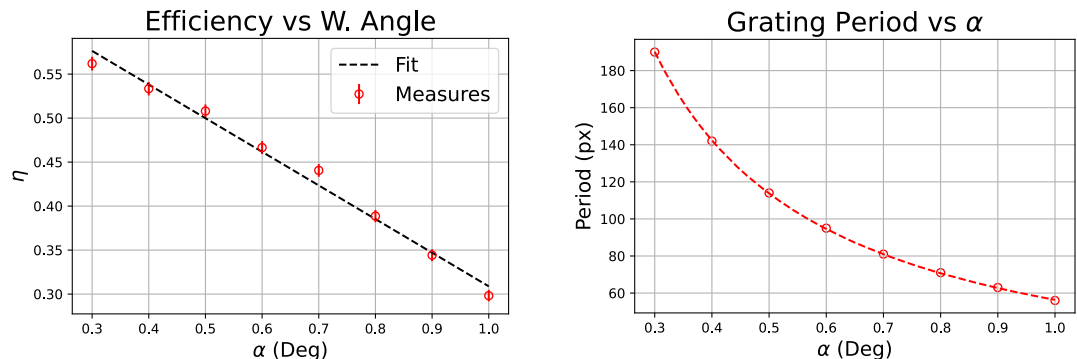


Figure 3.12: Diffraction efficiency η and the period of the diffraction gratings as a function of the working angle α . As shown in the figure on the right, the number of steps for the ramps of the measured gratings, based on Fig. 3.7, is sufficiently large to exclude it as the main cause of the reduction in diffraction efficiency as the working angle increases.

While the diffraction efficiency sets an upper bound for the choice of the working

angle, the need to avoid the zero order and to have enough space for generating the patterns establishes a lower bound. A working angle of 0.5° has been considered optimal since it gives us a diffraction efficiency² $\eta = 0.5$ and a distance of around 3.5 mm from the zero order, which is sufficient to generate arrays with more than 100 optical tweezers, with a spacing of $250 \mu\text{m}$ (at the Scan Lens focus).

This angle will be used for all the patterns we produce by adding the corresponding diffraction grating to the respective CGH.

3.3.4 Fourier Calibration

If we want to generate an array of focused spots, we need to set the coordinates of the spots as parameters. The simplest way to do this is to use the camera pixel indices as a reference frame. Similarly, if we want to create a generic pattern with the SLM, we also need to adapt the dimensions of the generated pattern to match those of the camera sensor.

The natural reference frame of the CGHs is the one of the unit cells into which the far field is subdivided, and it usually differs in size from what is observed by the camera. In our case, we typically observe only a fraction of this plane (both at the focus of the scan lens and at that of the objective), since the sensor is much smaller than it.

To solve this problem and find a conversion between the camera pixel reference frame, \vec{x} , and the $\{\vec{k}\}$ - space of the far field, we use a procedure called *Fourier Calibration* [45]. This procedure involves generating a square array using the $\{\vec{k}\}$ - space reference. The positions of the spots are then determined by searching for 2D-Gaussian profiles in the camera field and calculating the coefficients needed to create a map between the two frames. The resulting relation takes the form:

$$\vec{x} = M \cdot (\vec{k} - \vec{a}) + \vec{b} \quad (3.3)$$

This procedure takes only a couple of seconds and must be performed every time we initialize the setup. It is also important to repeat it periodically, depending on the tendency of our optics to drift. Furthermore, this procedure is essential for correcting aberrations, as it allows us to select the position of the interference pattern and determine the shifts in the fringe positions caused by optical aberrations (Fig. 2.13).

An example of the output of this procedure can be seen in figure Fig. 3.13 and in Fig. 3.14 where we can see that the all the elements of the generated array are marked with a red circle. The quality of the procedure depends on how well the algorithm can detect the correct center of the spots. Therefore, it is affected by the presence of optical aberrations and by the distance between the spots, that must be sufficient to avoid overlaps.

²Extremely close to the maximum predicted for our SLM model [24].

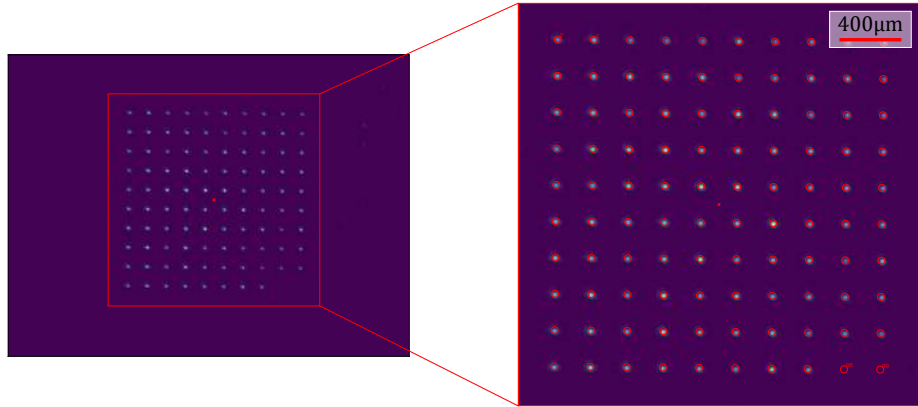


Figure 3.13: Output of the Fourier Calibration performed at the focus of the Scan Lens. The array used for the calibration was a 10×10 spot grid.

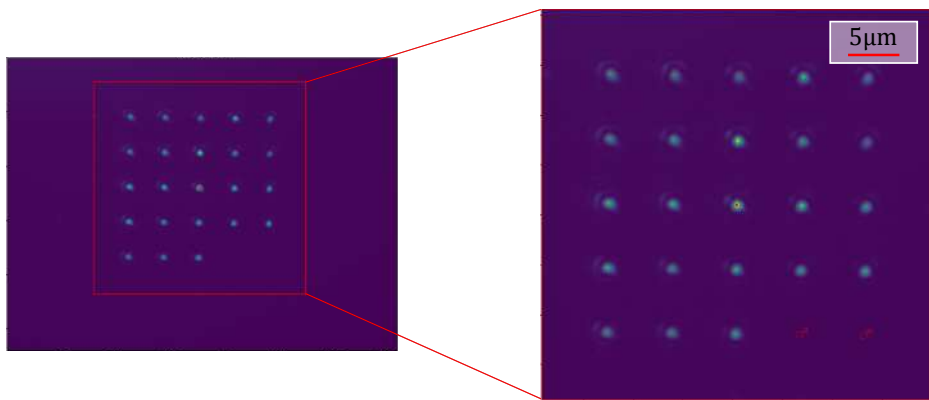


Figure 3.14: Output of the Fourier Calibration performed at the focus of the Mitutoyo objective. The array used for the calibration was a 5×5 spot grid, smaller than the one at the focus of the Scan Lens due to the high magnification produced by the Olympus objective.

Notice that both in Fig. 3.13 and in Fig. 3.14, the last two elements of the array are missing. This was done intentionally to ensure the correct orientation of the array and avoid a flipped reference frame due to incorrect positioning of the origin.

One last observation: an incorrect evaluation of the parameters in Eq. (3.3) can have various consequences. Errors in the evaluation of the parameters \vec{a} and \vec{b} will produce a shift in the determined reference frame relative to the camera frame, while an error in the calculation of M will influence the scale of the pattern. If our target is a spot array, this will modify the relative distance between the spots.

3.4 Wavefront Calibration

This section will be dedicated to *Wavefront Calibration* [45], the algorithm that implements the method discussed in subsection 2.5.1 [8], from which we determine the phase pattern to compensate for the optical aberration affecting the

system. It also evaluates the amplitude pattern of the beam incident on the SLM display, providing a complete characterization of the wavefront.

We already know that this algorithm divides the SLM display into sections called superpixels. One of these superpixels, usually the central one, is used as a reference. Some of the steps performed to determine the amplitude and phase offset of a single superpixel are shown in Fig. 3.15, which we will now discuss in detail.

First, a diffraction grating is applied to the display to direct all the light as far as possible from the *Calibration Point*, the region where we want to center all the interference patterns. This point is typically chosen at the center of the camera sensor, and it must be positioned far from the Zero-Order spot, located at the edge of the field of view.

At this point, the background light is measured and removed as an offset from the other measurements performed by the procedure. After that, a blaze grating is applied first to the reference and then to the target superpixel, respectively, sending the relative fraction of the beam to the Calibration Point. Their power is measured. Then, the two gratings are applied simultaneously, producing the interference pattern. The phase of the target superpixel can be obtained in two ways.

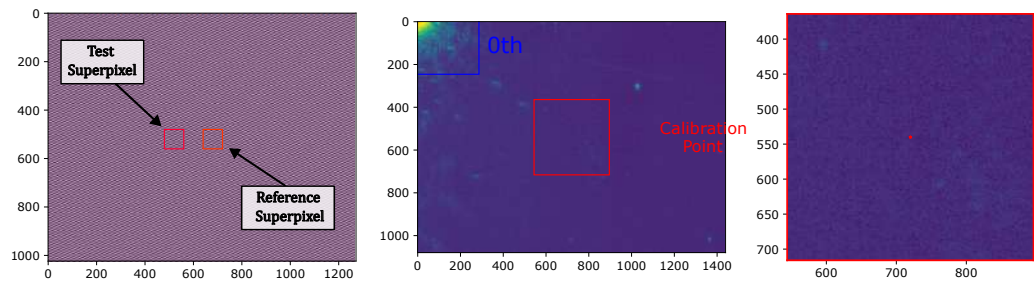
The first method consists of adding many different phase offsets to the target superpixel, measuring the resulting interference pattern each time. From these measurements, we plot the intensity at the center of the Calibration Point versus the applied phase shifts (Fig. 3.16). By fitting a sin function (similar to Eq. (2.34)) and searching for its maximum value, we obtain the phase offset between the target and reference superpixels.

The other method, that is the one we use most often, consists of taking just one measurement of the interference pattern without applying any offset to the target. This amplitude pattern is fitted with a 2D-interference profile [15, p.120-122] (Fig. 3.17), and from that, we derive the phase offset. This method is faster than the first one but more sensitive to noise, so to use it, we must isolate very well the system from stray light sources.

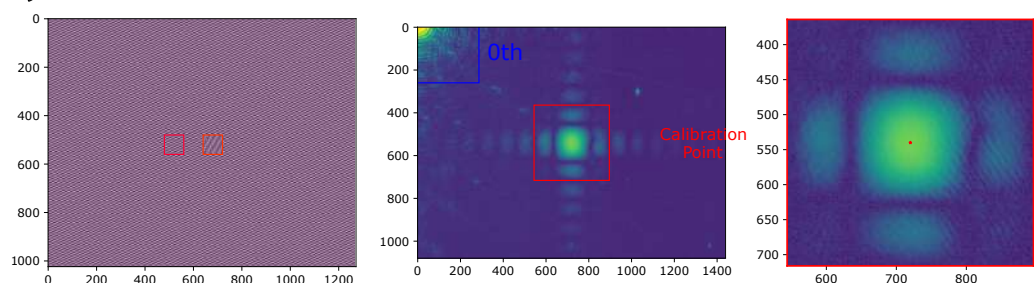
An important step, regardless of the method, is to test one of the central superpixels before performing the full procedure. This ensures that we don't saturate the camera during the process, as saturation would ruin the quality of the fit, making the correction useless. If the central pixel doesn't saturate, we can be reasonably sure that this will also be true for all the others.

At this point, we have the phase offset of the target superpixel, and indeed, we can observe in the last plot from Fig. 3.15 that the main peak of the interference pattern is correctly centered.

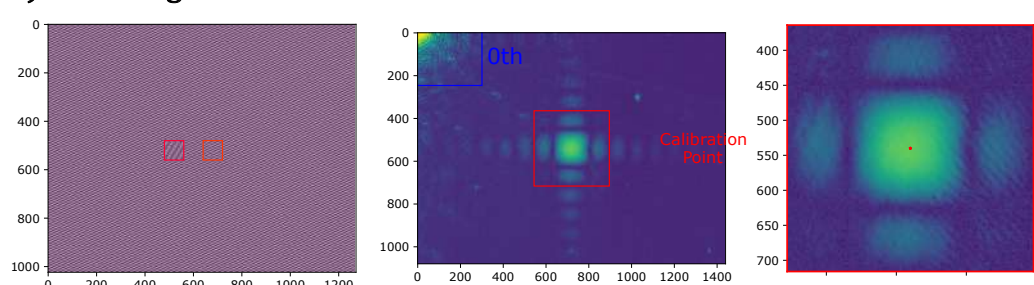
1) Background



2) Reference Diffraction



3) Base Target Diffraction



4) Best Interference

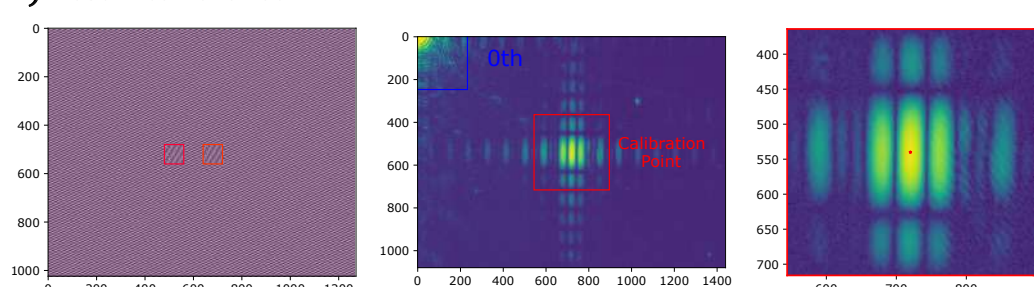


Figure 3.15: Main steps for calculating the phase offset of a superpixel. Measurements were taken at the focus of the Scan Lens using superpixels of 80×80 pixels.

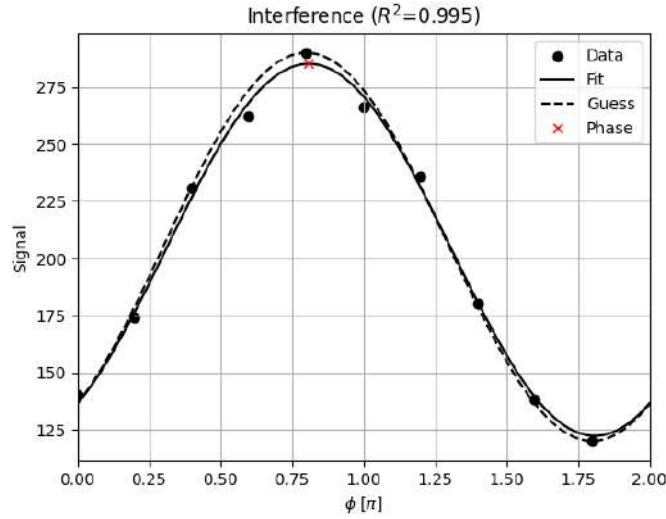


Figure 3.16: Plot produced to determine the phase offset of a superpixel of 80×80 pixels at the focus of the Scan Lens. The measured phase values were 10, from which a $\Delta\phi \approx 0.8\pi$ was evaluated.

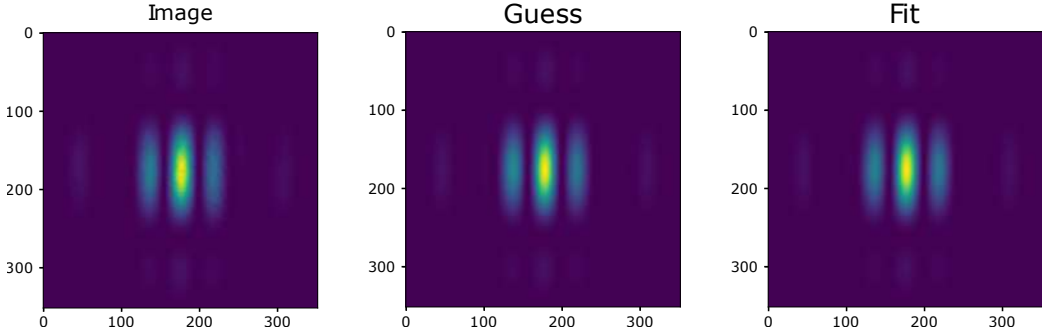


Figure 3.17: Image produced as a result of the interference between the reference and target superpixels. The image is then fitted to obtain $\Delta\phi$. This pattern was produced by a superpixel of 80×80 pixels at the focus of the Scan Lens. Due to the position of the camera, we cannot filter out the 0th-order using the iris.

This procedure is performed on all the superpixels into which the SLM display has been divided. The obtained phase and amplitude values are then processed, filtering out all values related to superpixels where the fit parameter R^2 exceeds a certain threshold, usually set to 0.9. To the discarded values, an offset value is assigned. The resulting wavefront is smoothed to remove discontinuities between the superpixels, improving the quality of the results.

In Figs. 3.18 and 3.19, we can see two examples of the wavefronts obtained. The first one was measured at the focus of the Scan Lens, while the second refers to the setup in Fig. 3.2. Notice that the second correction also takes into account the Olympus microscope objective and the last lens before the camera, whereas the first setup does not include any optical elements between the point of interest and the camera. In both cases, we can observe the effect of the iris positioned after the telescope on the Gaussian beam.

Note that the obtained corrections are relative to the calibration point, and they will become less effective as we move farther from it.

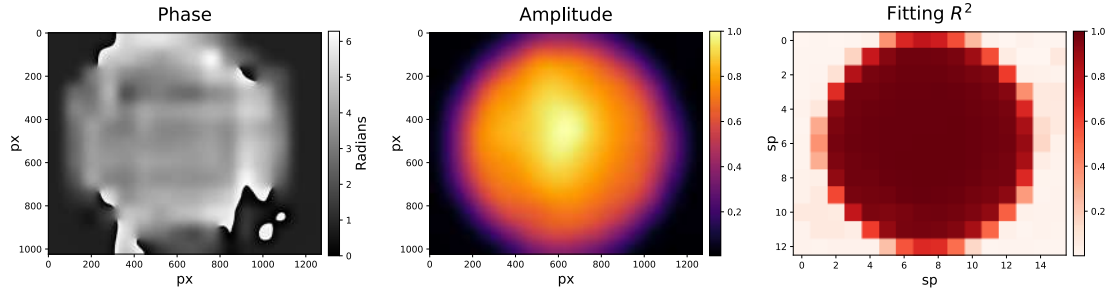


Figure 3.18: Wavefront calibration output at the focus of the scan lens for superpixels of 80×80 pixels.

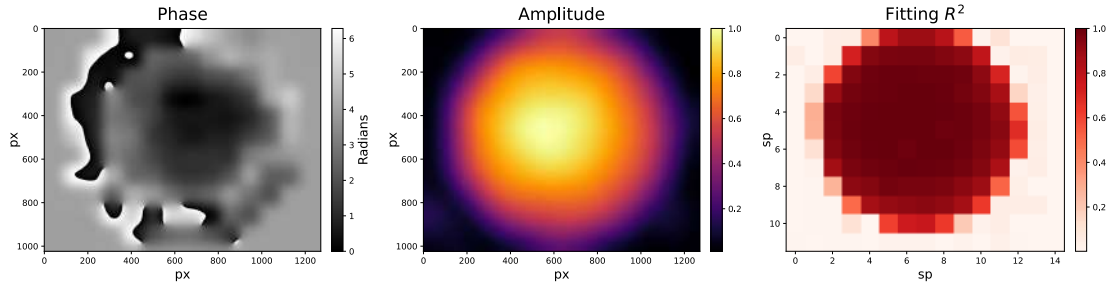


Figure 3.19: Wavefront calibration output of the system shown in Fig. 3.2 for superpixels of 90×90 pixels.

3.4.1 The Diffraction Limit

To verify the quality of the correction, we apply a flat phase pattern and observe how closely the obtained spot resembles the PSF of the system, quantifying this similarity by comparing their waists.

First, we simulate the PSF. Since the dominant effect is produced by the circular aperture associated with the Mitutoyo objective, we obtain the expected Airy disk, with the typical distance between the main peak and the first zero given by $d_{AD} = 0.61 \frac{\lambda}{NA}$ [19, p.75–76], which in our case corresponds to 842 nm. We then fit this pattern with a 2D Gaussian. The waist of the PSF, and thus the diffraction limit of the system, will be the standard deviation of the resulting Gaussian function. We obtain a value of:

$$d_G \approx 0.424 \frac{\lambda}{NA} = 585 \text{ nm} \quad (3.4)$$

In Fig. 3.20, we can see the PSF of the system and the Gaussian resulting from the fit, as well as a comparison between their profiles.

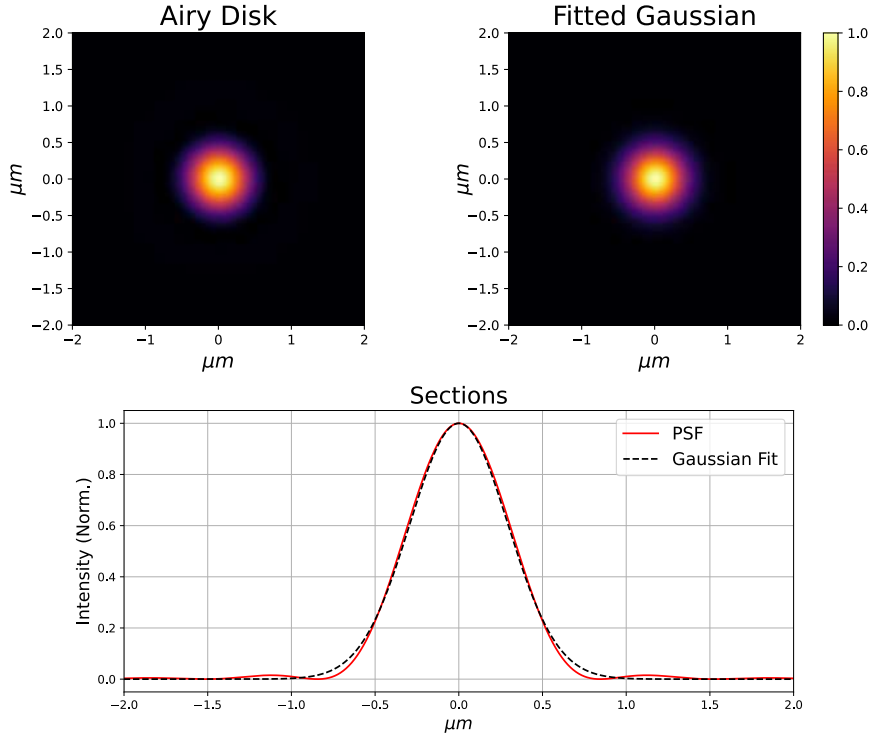


Figure 3.20: The top figures show the Airy disk corresponding to the PSF of the system and the Gaussian curve profile resulting from fitting it. The plot at the bottom shows a comparison between their profiles. The ratio of the distance from the main peak to the first zero of the Airy Disk and the standard deviation of the Gaussian is equal to: $\frac{d_{AD}}{d_G} \approx 1.44$.

In Fig. 3.21, we can see a comparison between the spot obtained before and after the correction. The applied correction is shown in Fig. 3.19, which is the best achieved during this thesis work. We observe that after the correction, the tweezers appear more symmetric, and the outer ring present in the uncorrected spot has almost completely vanished, approaching the shape of the PSF. This can be better understood by examining Fig. 3.22, where we plotted the two sections corresponding to the lines passing through the center of the tweezers along the plot axes of Fig. 3.21. We quantify this improvement by comparing the waist evaluated with the same procedure used for the PSF.

For the uncorrected spot, we obtain: $w_x = 0.632 \pm 10$ nm and $w_y = 664 \pm 11$ nm. These values confirm the astigmatic character of the spot. For the corrected spot, we obtain: $w_x = 624 \pm 10$ nm and $w_y = 621 \pm 10$ nm, which correspond to 1.07 ± 0.02 and 1.06 ± 0.02 times d_G , respectively. The error in these values is almost entirely due to the uncertainty in evaluating the magnification of the Olympus microscope objective. This proves that the wavefront measured via Wavefront Calibration effectively compensates for the aberrations present in our optical system.

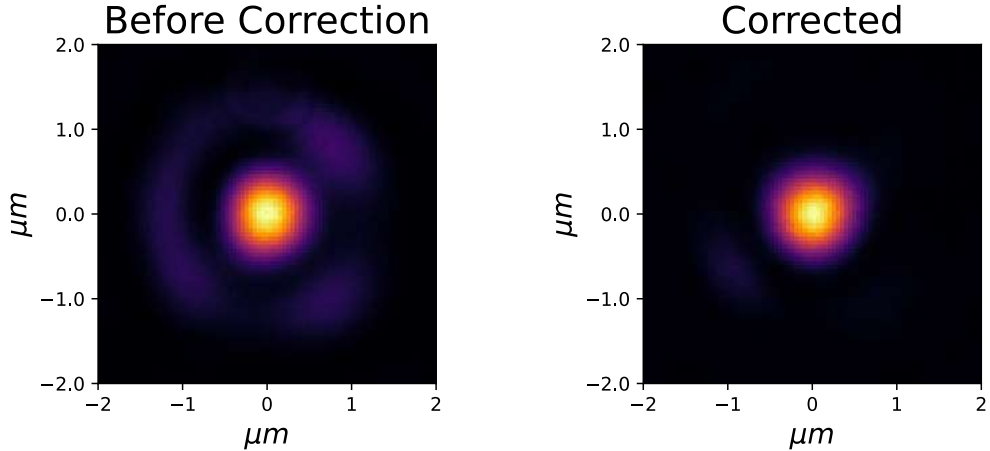


Figure 3.21: Single spot obtained from a flat phase profile, before and after the correction.

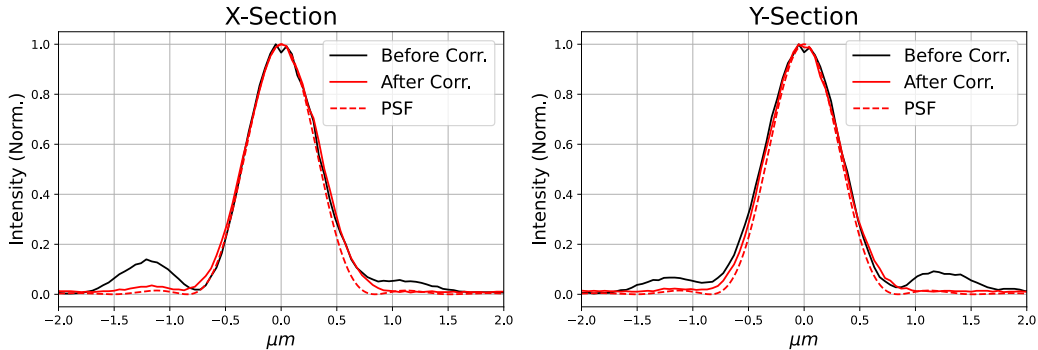


Figure 3.22: Sections of the spot in Fig. 3.21 along the two plot axes, compared with the system's PSF.

We conclude by showing the waist obtained using different sizes of superpixels in the Wavefront Calibration. As we can see in Fig. 3.23, reducing the size of the superpixels improves the quality of the wavefront. However, even for superpixels as large as 200×200 pixels, we observe an improvement in the symmetry of the spot compared to the uncorrected one.

The only one exception to this behavior is the spot obtained with the 80×80 pixels block correction. This is due to the fact that the table on which the setup was built did not shield environmental vibrations well, particularly those coming from the chiller used to cool the Ti:Sapph laser, which was located nearby. We believe that this source of noise caused drift in the optics, preventing a valid execution of the Wavefront Calibration with superpixels smaller than 90×90 pixels, since for them the procedure required too much time compared to the timescale of the drifts.

Note that this issue only occurred in the complete setup, due to the high sensitivity of the two consecutive microscope objectives (Fig. 3.2).

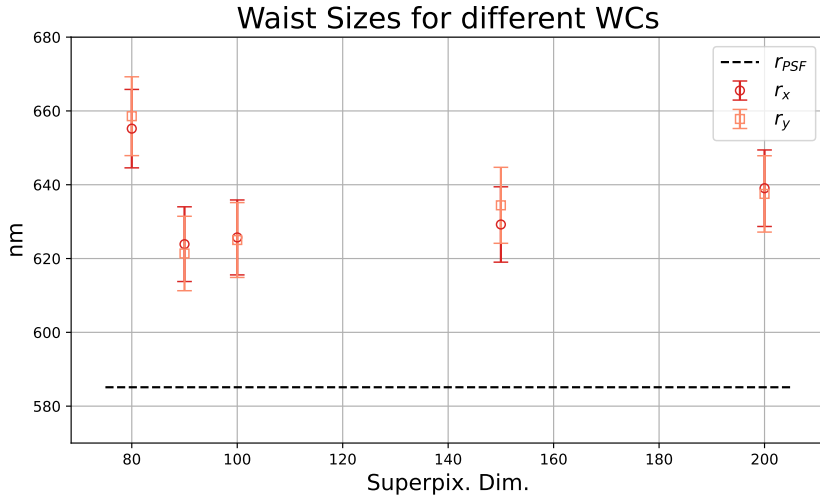


Figure 3.23: Waist of the spot obtained by applying a flat phase profile on the SLM after performing the Wavefront Calibration, for different superpixel dimensions. The incoherent values obtained for the 80×80 pixels block correction are a consequence of drifts in the most sensitive elements of the setup that occurred during the Wavefront Calibration.

3.5 Active Compensation of Inhomogeneities

In our setup (Fig. 3.2), we are able to communicate simultaneously with both the SLM and the camera. This feature, in addition to allowing for aberration compensation, also enables the implementation of a feedback loop to improve the quality of the generated patterns.

We have already explained the flow chart of the GSA in the previous chapter (Fig. 2.8) and the differences with respect to the Weighted GSA, which uses a weight function (2.32), making it more suited for the generation of spot arrays. The compensation of inhomogeneities is based on this weight function. In the Weighted GSA, during the generation of the CGH, before applying the constraint of the target amplitude, there is an intermediate step where the weight of each spots is measured [35]. The feedback consists of utilizing the weight of the real spots in the Fourier Domain instead of the simulated ones. In this way, we account for the presence of aberrations during the generation of the CGH, which cause a degradation of the produced patterns compared to the simulated ones. Even if we apply Wavefront Calibration to compensate for aberrations, we are still far from achieving a flat phase wavefront, especially in regions far from the calibration point used in the Wavefront Calibration procedure. This is why taking the weights directly from the generated spots improves the quality of the patterns. On the other end, if we were able to perfectly correct aberrations, the feedback would be useless.

Note that this homogenisation procedure cannot be applied in the basic version of the GSA, as it does not use a weight function or anything similar that can be utilized in the same way. For the generation of images that are not spot-based,

we did not observe any significant improvement when using the Weighted GSA with a feedback loop instead of the GSA.

In Fig. 3.24, we can see histograms showing the power distribution of the spots for a Kagome array of 243 sites at the focus of the Scan Lens, before and after the amplitude homogenisation procedure. We observe that the spread of the distribution is significantly reduced after applying the feedback, decreasing to one sixth of its value prior to the procedure. In Tab. 3.1, we also include other values regarding the arrays before and after feedback. We can see that the mean waist of the spots (\bar{w}_x , \bar{w}_y), as well as the mean radial displacement from their expected locations (\bar{r}_d), do not show significant improvements. Thus, the major effect of the feedback procedure is an increase in the uniformity of the spots, which is the quantity most closely related to the weight function used by the amplitude homogenisation routine.

	Pow. Spread	\bar{w}_x	\bar{w}_y	\bar{r}_d
Before F.	$31.0 \pm 2.5\%$	$23.5 \pm 0.1 \mu\text{m}$	$21.2 \pm 0.1 \mu\text{m}$	$4.1 \pm 0 \mu\text{m}$
After F.	$5.9 \pm 0.2\%$	$23.4 \pm 0.1 \mu\text{m}$	$21.2 \pm 0.1 \mu\text{m}$	$4.8 \pm 0 \mu\text{m}$

Table 3.1: Parameters of a Kagome array, with 243 spots, before and after the application of the feedback.

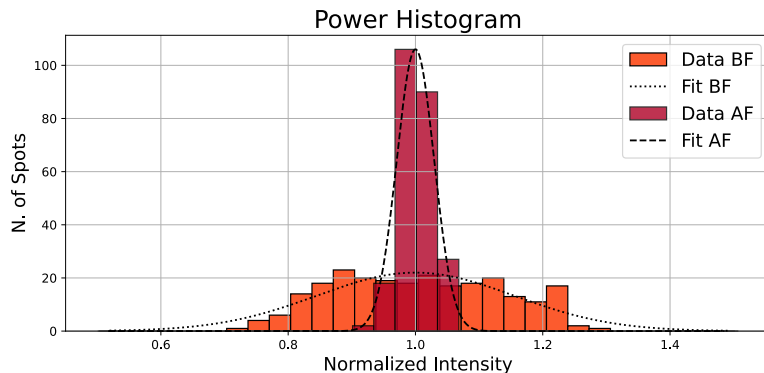


Figure 3.24: Histograms of the power distribution of the spots for a Kagome array of 243 spots, before and after the feedback procedure. The two curves are the result of fitting the two distributions with a Gaussian function. The power spread is obtained as the ratio between the standard deviation of the Gaussian and its mean value, σ_{fit}/μ_{fit} . The power values are normalized with respect to the mean values obtained from the Gaussian fits.

In Fig. 3.25, we can see the resulting array after 50 iterations of the Weighted GSA using feedback. This array was generated after applying the wavefront calibration shown in Fig. 3.18. In this case the PSF is an Airy Disk, with $d_{AD}^{sl} \approx 28.94 \mu\text{m}$, which using the conversion factor calculated in (3.4) gives a diffraction limit of $d_G^{sl} \approx 20.11 \mu\text{m}$.

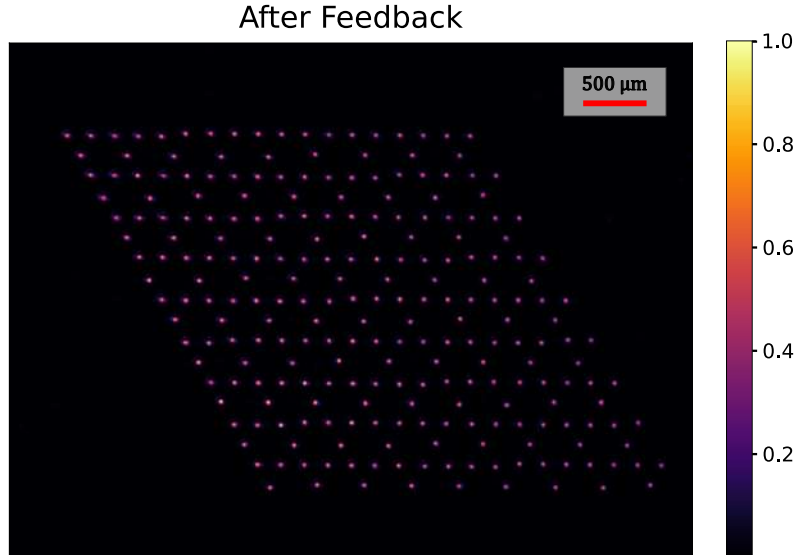


Figure 3.25: Kagome array after 50 iterations of the Weighted GSA using the feedback. Note the elongated shape along the x direction of the left-side spots, resulting in a mean waist value larger than that in the y direction. The low quality of these spots is due to their distance from the calibration point used for Wavefront Calibration. We chose this array to demonstrate the potential of the feedback routine because of the high number of spots, which we cannot observe in the focus of the Mitutoyo objective.

To perform the analysis on the arrays, we associate each spot with a square region centered on its expected position, typically with a side length of 90 pixels. We then fit these regions with a 2D Gaussian and evaluate their centers and waists from the fitted curves. From their mean values, we obtain \bar{w}_x , \bar{w}_y and r_d . To evaluate the power associated with each spot, we sum the intensity values measured by the camera for each pixel in the corresponding region, which represents its power. Using this information, we generate histograms and fit the distributions with a Gaussian. The power spread, which relates to the uniformity of the arrays, corresponds to the standard deviation of the Gaussian divided by its mean value (σ_{fit}/μ_{fit}). The smaller this value, the more uniform the array.

We use this parameter, instead of the one obtained with the formula:

$$u = 1 - \frac{I_{Max} - I_{min}}{I_{Max} + I_{min}} \quad (3.5)$$

This is because u is insensitive to the distribution of the data, while the bell shape of the histograms (Fig. 3.24) make a Gaussian fit more suitable for analysis.

In conclusion, the ability to perform a feedback routine on the generated arrays is very useful, as it enables homogeneity between the spots that would not otherwise be easily achievable. This feature is especially important in tweezer arrays, as uniformity is crucial for quantum simulation applications to ensure equal trap depth and loading probability across the spots, as well as enhancing the predictability of the resulting system [31, 51, 41, 38].

3.6 Results Evaluation

Now we will present some of the arrays obtained at the focus of the Mitutoyo, along with considerations regarding their quality and the minimum distance achievable between the spots. We will also show patterns that are not spot-based, generated in the focus of the Scan Lens. Although these patterns were created for fun, they will serve as a starting point for important considerations that will be fundamentals in the next chapter.

3.6.1 Arrays

The arrays are shown in Fig. 3.26, and their statistics in Tab. 3.2. Although the scale indicated by the bar is two orders of magnitude smaller than that in Fig. 3.25, their quality has not deteriorated significantly. As we can see in Tab. 3.2, they are less uniform and show slightly different mean waist sizes along the two axes. This difference is caused by the blurred shape of the spots on the edges of the images, particularly on the left side. This blurriness results from aberrations that are not well corrected, but can also be a consequence of their distance from the calibration point used for the Wavefront Calibration. No significant worsening effects are observed with an increasing number of spots, indeed, the best array is probably the Kagome array, which has 48 sites. The values in Tab. 3.2 are obtained with the same approach described in the previous section to obtain the values in Tab. 3.1.

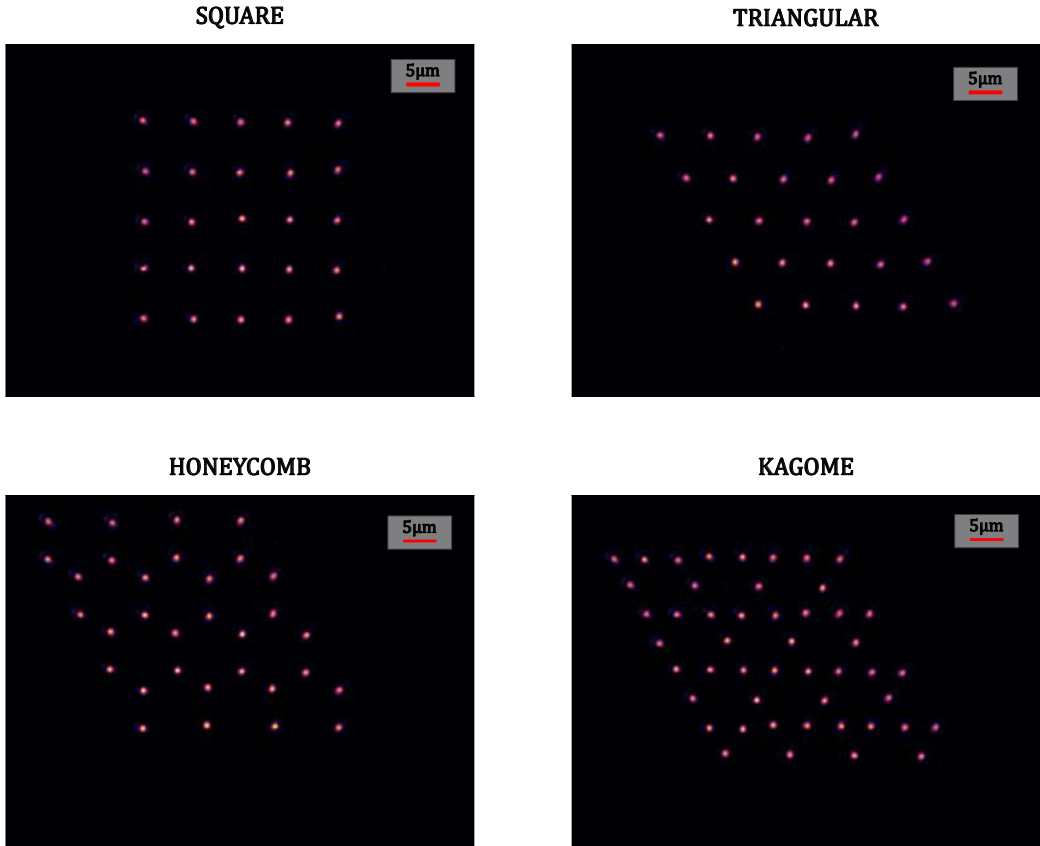


Figure 3.26: Arrays generated with different geometries. These results are from 50 iterations of the Weighted GSA with feedback, using the aberration compensation shown in Fig. 3.19.

Configuration	Pow. Spread	\bar{w}_x	\bar{w}_y	\bar{r}_d
Square (9)	$11 \pm 1\%$	634 ± 11 nm	648 ± 12 nm	60 ± 1 nm
Square (25)	$14 \pm 2\%$	636 ± 12 nm	645 ± 12 nm	47 ± 1 nm
Square (49)	$14 \pm 2\%$	642 ± 12 nm	669 ± 13 nm	51 ± 1 nm
Triangular (25)	$13 \pm 2\%$	637 ± 12 nm	678 ± 12 nm	78 ± 1 nm
Honeycomb (32)	$14 \pm 2\%$	637 ± 12 nm	653 ± 12 nm	56 ± 1 nm
Kagome (48)	$15 \pm 3\%$	633 ± 12 nm	649 ± 12 nm	21 ± 0 nm

Table 3.2: Statistics for various arrays, including those in Fig. 3.26. The numbers in parentheses in the first column indicate the number of sites.

3.6.2 Minimum Distance

We will now move on to the study of the minimum distance that can be achieved between two spots. From theory, we know that there are two limits.

The first limit comes from the *Rayleigh Criterion* for resolution [19, p.157–158], which states that we can distinguish two points if their distance is greater than:

$$R = 0.61 \frac{\lambda}{NA} \quad (3.6)$$

We have already calculated this quantity, which corresponds to the distance between the main peak and the first zero of the Airy disk, the PSF of our system, and corresponds to 842 nm. The other limit is related to the dimensions of the unit cell in which the Fourier Domain is discretized (Eq. (2.29)). This is essentially half the distance between the main zeros of the 2D *sinc* function [19, pp. 75–77], corresponding to the PSF of the full SLM display in the focus of the Scan Lens. In our case, since we are applying a circular mask on the SLM display, we can assume that the SLM display is a square with a side equal to the diameter of the mask. This implies that the unit cell will also have a square shape with side $\Delta x = 23.72 \mu\text{m}$. If we divide this value by the de-magnification value of the Mitutoyo, we obtain: $\Delta x^{mit} = 678 \pm 12 \text{ nm}$, which will set the lower bound to the minimum distance possible between two spots.

In Fig. 3.27, we examine how close we can get to this separation. We generated a 4-spot square array, which has a power spread of $15 \pm 3\%$, $\bar{w}_x = 625 \pm 11 \text{ nm}$, $\bar{w}_y = 628 \pm 12 \text{ nm}$ and $\bar{r}_d = 124 \pm 2 \text{ nm}$ with a desired distance of 60 px between the spots, corresponding to $2.906 \mu\text{m}^3$. We can see that up to 30 px, even if the shape of the spots is distorted, they can still be considered distinct. This is good, considering that Δx^{mit} correspond to $13.99 \pm 0.46 \text{ px}$.

At 20 px of separation corresponding to $0.969 \mu\text{m}$, the spots start to merge into a shapeless configuration, consistent with being very near to the theoretical limit. Note that the distortion of their shape is completely due to the phase mask applied on the SLM.

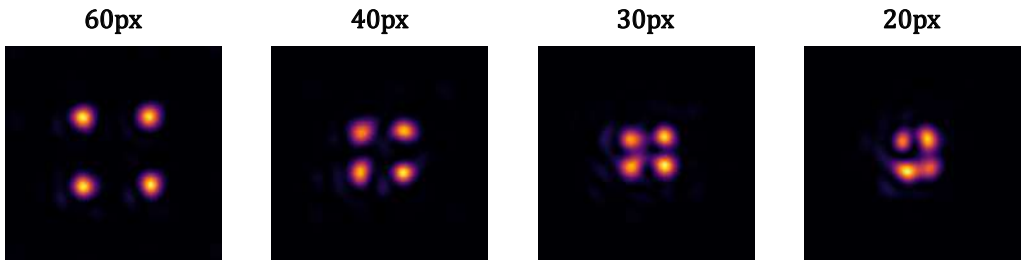


Figure 3.27: 4 spot arrays for different distance between the spots.

3.6.3 Generic Images

We conclude the chapter by showing two patterns generated at the focus of the Scan Lens, which can be observed in Fig. 3.28. Instead of a uniform pattern, they exhibit the phenomenon of *speckles*. Typically, this is a consequence of defects

³For separations below 60 px, we did not have enough space between the spots to study them separately.

in the optics on a scale comparable to the wavelength of the source, which, due to its coherence, generates random interference between various sections of the wavefront, resulting in brighter and darker zones known as speckles [18].

In our case, more than defects, the main source of this noise is the rapidly varying phase profile of the far field. We will discuss more about this in the next chapter.

On a positive note, even though this speckle noise is not functional, and very debilitating if we want to generate smooth intensity profiles, it adds an artistic touch to the images in Fig. 3.28.

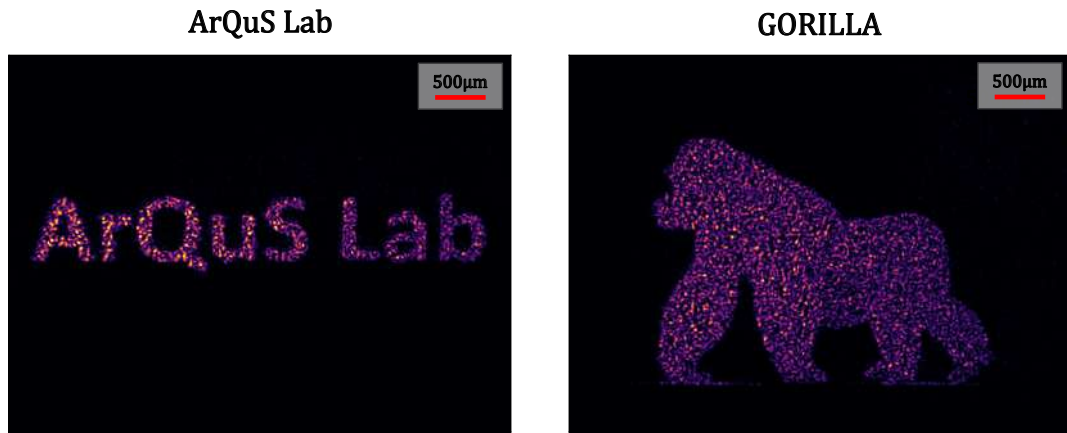


Figure 3.28: Two images taken at the focus of the Scan Lens, generated using 50 iterations of the GSA, where we can observe the presence of speckles noise.

The SLM has the ability to generate any intensity pattern we desire, allowing us to create arbitrary potential shapes that can be applied to atoms. We are particularly interested in double well structures to study the phenomenon of quantum tunneling, one of the most iconic aspects of quantum mechanics. In this chapter we will study the tunneling of ytterbium atoms in a double well potential using the magic wavelength for the clock transition at $\lambda = 759$ nm. This could be the starting point for simulating lattice models, such as those derived from the Hubbard model [51], as well as exploring more complex dynamics within various potential shapes.

We will begin our analysis with a very simple shape: a parabola with a rectangular barrier at its center. We will characterize the tunneling in the resulting system, also taking into account the effect of the optics on the potential's shape, and conclude with a test conducted on our setup. Unfortunately, it was not designed to generate this kind of pattern.

We will conclude the chapter discussing some adjustments that can be applied to the setup and the GSA in order to obtain smooth potentials, reducing the defects introduced by the speckle noise.

3.7 Theoretical model

In this section, we will present the mathematical model used for the double well tunneling dynamics. We will define the potential, diagonalize it, and show how its eigenvalues can be used to define the tunneling rate.

The potential is a parabola, with a rectangular split at its center, along one of its axes. It is defined as follows:

$$V(x, y) = \left[-V_0 + \frac{1}{2}m(\omega_x^2x^2 + \omega_y^2y^2) \right] \cdot \left[1 - \Theta\left(x + \frac{d}{2}\right) + \Theta\left(x - \frac{d}{2}\right) \right] \quad (3.7)$$

where $\Theta(x)$ is the *Theta Function*, which is 0 for $x < 0$ and 1 for $x \geq 1$. As we can see, aside from the mass of the particle, m (which in our case is the mass of the ytterbium atom), the potential in Eq. (3.7) is defined by three parameters: the trap depth V_0 , the frequencies ω_x and ω_y , and the dimension of the central barrier d . Eq. (3.7) is defined for all values of x, y such that $V(x, y) \leq 0$.

In Fig. 3.29 we can see a plot of $V(x,y)$ for $V_0 = h \cdot 100$ kHz, $w_x = 2\pi \cdot 1$ kHz, $w_y = 2\pi \cdot 4$ kHz and a split $d = 400$ nm.

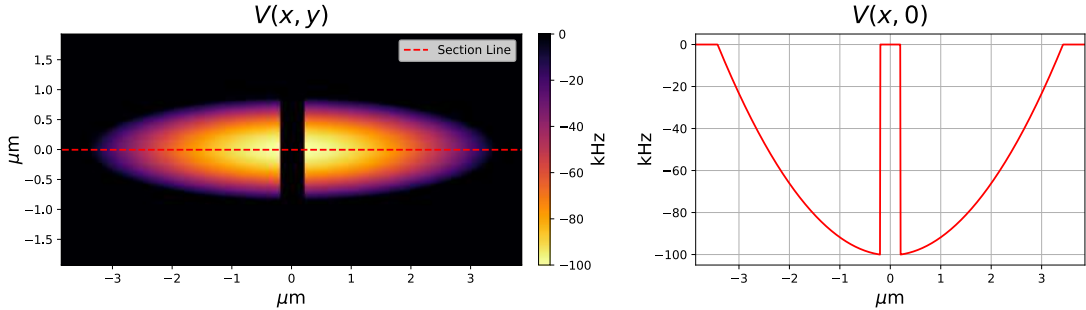


Figure 3.29: Plot and relative section of $V(x, y)$ for $V_0 = h \cdot 100$ kHz, $w_x = 2\pi \cdot 1$ kHz, $w_y = 2\pi \cdot 4$ kHz, and $d = 400$ nm.

Now that we have defined the potential, we need to obtain its energy spectrum. To do this, we tried several bases, but in the end, the most complete one to span the Hilbert space associated with the potential defined in Eq. (3.7), was the *Harmonic Oscillator* (HO) basis.

Since $V(x, y)$ does not couple the two axes of the reference frame, we can factorize the wavefunction, leading to two separate problems along the two directions. Given that we are interested in the tunneling phenomenon along the x -axis, we can ignore the other direction and focus on the corresponding 1D problem⁴.

To lighten the notation we will use the HO natural units:

$$\epsilon_{HO} = \hbar\omega \quad a_{HO} = \sqrt{\frac{\hbar}{m\omega}} \quad (3.8)$$

In this units, the Hamiltonian of the problem is:

$$H = -\frac{1}{2} \frac{d^2}{dx^2} + V(x, y) \quad (3.9)$$

where $V(x, y)$ is expressed in units of ϵ_{HO} . The elements of the HO basis are:

$$\psi_n(x) = \langle x | n \rangle = \frac{1}{\sqrt{2^n n!}} \pi^{-\frac{1}{4}} e^{-\frac{x^2}{2}} H_n(x) \quad (3.10)$$

where $H_n(x)$ is the Hermite Polynomial of degree n .

If the Hamiltonian were that of the HO with an offset of V_0 , the energy levels would be:

$$E_n = -V_0 + \frac{1}{2} + n \quad (3.11)$$

To obtain the energy spectrum associated with $V(x, y)$, we used the matrix formulation of the Hamiltonian in the HO basis. The elements of this matrix are

⁴From now on, we will omit the subscript indicating the axis, as we will only consider the x -direction

defined as [39, 29]:

$$H_{nm} = \langle \psi_n(x) | H | \psi_m(x) \rangle \quad (3.12)$$

Since we cannot use all the infinite elements of the basis, we need to determine how many of them are sufficient to obtain an accurate evaluation of the lowest energy levels of the spectrum, which are of interest for defining the tunneling rate. To do this, we diagonalize the Hamiltonian matrix for different numbers of basis elements until we observe convergence in the resulting eigenvalues.

In Fig. 3.30, we plot the results of this evaluation. In particular, we evaluate the relative difference of the two lowest obtained eigenvalues for different basis dimensions, for the potential shown in Fig. 3.29. The relative difference is defined as:

$$r.d. = \left| \frac{\epsilon_i - \epsilon_{i-1}}{\epsilon_i} \right| \quad (3.13)$$

where i is the index referring to the number of elements used to generate the Hamiltonian matrix. We can observe that for 15 elements, we reach a relative difference lower than 0.001 (0.1%), which is reduced by one order of magnitude using 50 elements.

Given the high convergence rate and the relatively short computation time, which takes only a few minutes, we decided to use a basis of 50 elements for our calculations. The lower levels of the spectrum are shown in Fig. 3.31

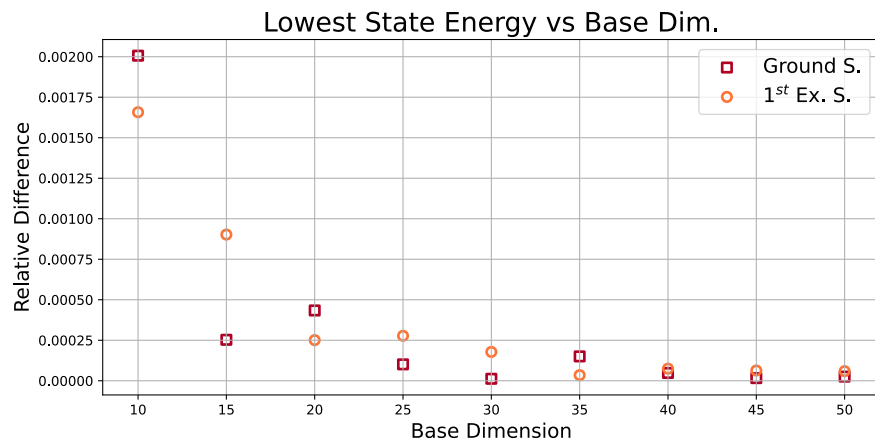


Figure 3.30: Relative difference (Eq. (3.13)) of the two lowest eigenvalues for different numbers of elements of the HO basis used to compute the energy spectrum. The potential to which this plot is referred is the one in Fig. 3.29.

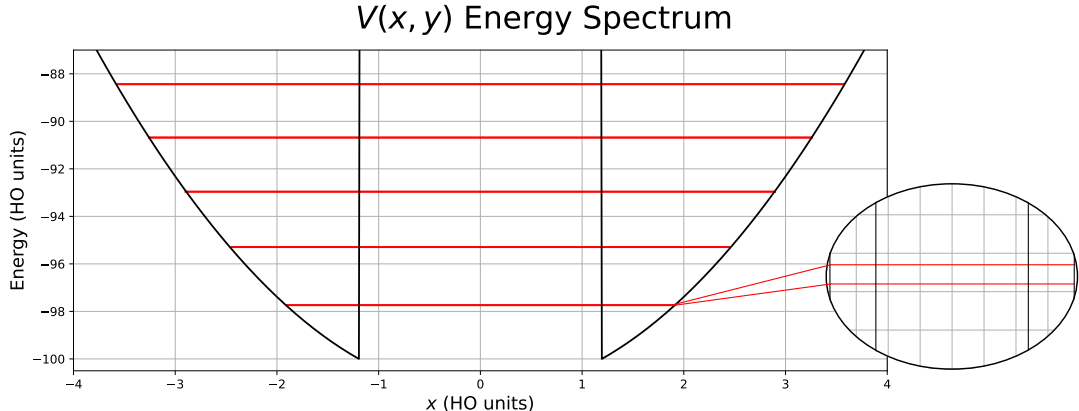


Figure 3.31: The 10 lowest energy levels of the potential shown in Fig. 3.29. As we can see, these levels are grouped into doublets, with a splitting much smaller than the splitting between different doublets.

As shown in Fig. 3.31, the lower levels of the spectrum are grouped into doublets. To understand why we have this distribution, we first need to consider the following potential:

$$U(x, y) = \frac{1}{2}m\omega^2x^2 + \delta(x) \quad (3.14)$$

This is essentially the potential of the HO with a δ -shaped barrier at the origin. The presence of the δ -function penalizes all HO states with an even index due to the fact that $\psi_n^{even}(x = 0) \neq 0$. As a result, the eigenfunctions of this potential will be the odd eigenfunctions of the HO, with a double degeneracy to restore the correct number of states.

In our case, the barrier does not have infinite height like the δ -function and moreover has a finite width, and so, instead of two completely degenerate levels, the states will be coupled into doublets, with a splitting that depends on the height and width of the barrier.

To obtain the tunneling rate, we have to define $\psi_L(x)$ and $\psi_R(x)$, which are the states with the wavefunction localized on one side of the barrier, each having the lowest possible energy. These can be obtained by using the symmetric and antisymmetric combinations of the eigenvectors of the lowest doublet [31]:

$$\psi_{L,R}(x) = \frac{1}{\sqrt{2}} [\psi_{GS}(x) \pm \psi_{ES}(x)] \quad (3.15)$$

where $\psi_{GS}(x)$ and $\psi_{ES}(x)$ are the wavefunctions of the ground state and the first excited state, respectively. Note that $\psi_L(x)$ and $\psi_R(x)$ are degenerate.

The two states obtained from the linear combination of the states belonging to the lowest doublet in Fig. 3.31 are shown in Fig. 3.32.

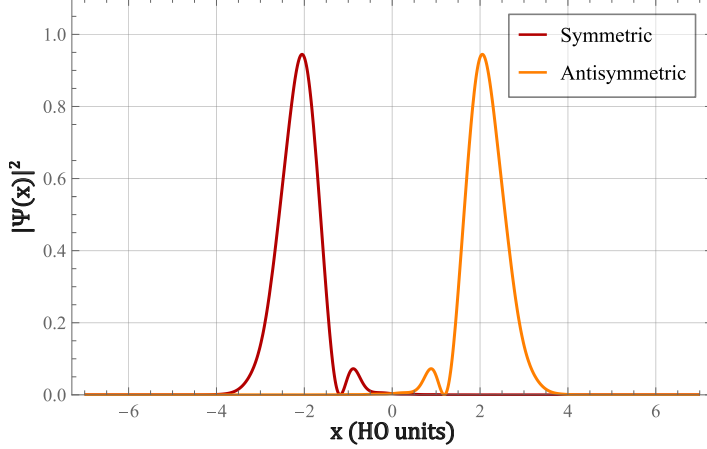


Figure 3.32: $|\psi_L(x)|^2$ and $|\psi_R(x)|^2$ obtained from the states belonging to the lowest energy doublet in Fig. 3.31.

To determine the tunneling rate, consider that the system is in an initial state localized on the left side of the barrier.

$$\Psi(x, t = 0) = \psi_L(x) = \frac{1}{\sqrt{2}} [\psi_{GS}(x) + \psi_{ES}(x)] \quad (3.16)$$

We aim to determine the time t_1 required for the system to transition from this state to the state localized on the right side:

$$\Psi(x, t = t_1) = \psi_R(x) = \frac{1}{\sqrt{2}} [\psi_{GS}(x) - \psi_{ES}(x)] \quad (3.17)$$

We know that for a generic time t , $\Psi(x, t)$ can be written as:

$$\Psi(x, t) = \frac{1}{\sqrt{2}} \left[\psi_{GS}(x) e^{-i \frac{E_{GS} t}{\hbar}} + \psi_{ES}(x) e^{-i \frac{E_{ES} t}{\hbar}} \right] \quad (3.18)$$

By comparing the last two equations, we obtain that:

$$\psi_{GS}(x) + \psi_{ES}(x) e^{-i \frac{(E_{ES} - E_{GS}) t_1}{\hbar}} \propto \psi_{GS}(x) - \psi_{ES}(x) \quad (3.19)$$

At this point we can determine the time t_1 :

$$e^{-i \frac{(E_{ES} - E_{GS}) t_1}{\hbar}} = -1 \implies t_1 = \frac{\pi \hbar}{E_{ES} - E_{GS}} \quad (3.20)$$

The tunneling rate J is defined as the frequency corresponding to the wavefunction that completes one full oscillation, going from left to right and back to left, with a period $T = 2t_1$, and thus:

$$J = \frac{E_{ES} - E_{GS}}{2\pi\hbar} = \frac{\Delta E}{\hbar} \quad (3.21)$$

We can see from Eq. (3.21), that $J \propto \Delta E$, which is consistent with the fact that shorter and taller barriers produce a larger splitting between the levels of

the doublets.

This model, and the corresponding definition of the tunneling rate J , is valid only if the different doublets are well separated from one another. The separation between the various doublets can be associated with ϵ_{HO} . This means that we need to have:

$$\Delta E \ll \epsilon_{HO} \implies \frac{2\pi J}{\omega} \ll 1 \quad (3.22)$$

The validity of this condition, ensuring that the doublets are well separated, allows them to be treated as independent two-level systems⁵. This is crucial for the assumption that $\psi_L(x)$ and $\psi_R(x)$ can be obtained as linear combinations of the two levels of the lowest energy doublet.

Note that these conditions also set an upper limit on the maximum value of J that can be obtained for a given ω .

For the potential in Fig. 3.29, this value corresponds to $J \approx 2.5$ Hz, and $\frac{2\pi J}{\omega} \approx 0.0025$.

3.8 Blurring Effect

As we have already discussed in the previous section, the PSF of our system is an Airy Disk with an associated waist of 585 nm. We also covered the Rayleigh criterion for resolution, which states that the minimum resolvable distance between two objects is 842 nm. These two values are a consequence of the finite apertures associated with the optics in the setup, and in particular to the microscope objective, which act as low-pass filters, cutting away the high frequencies associated with the Fourier transform of the amplitude patterns. These high frequencies correspond to the outer regions of the beam when it is collimated.

These effects must be considered, as the potentials we are interested in, such as the one in Fig. 3.29, have dimensions comparable to the PSF of the system. We simulate this effect and apply it to the potentials defined by Eq. (3.7). In particular, we take into account the blurring effect produced by the objective present in the main setup of the laboratory, which has a numerical aperture $NA = 0.6$, and a focal length $f = 27.15$ mm for a wavelength of $\lambda = 759$ nm. For this objective, the waist associated with the PSF is 536 nm, and the minimum resolvable distance is 772 nm.

In Fig. 3.33 we can see the consequence of this filtering on a potential with $V_0 = h \cdot 100$ kHz, $\omega_x = 2\pi \cdot 2$ kHz, $\omega_y = 2\pi \cdot 8$ kHz and a split $d \approx 154$ nm. As expected, the sharp edges of the barrier become smoother due to the filtering of the high frequencies.

⁵This is the two site version of being in the lowest band of a lattice provided the gap to higher bands is much larger than the bandwidth.

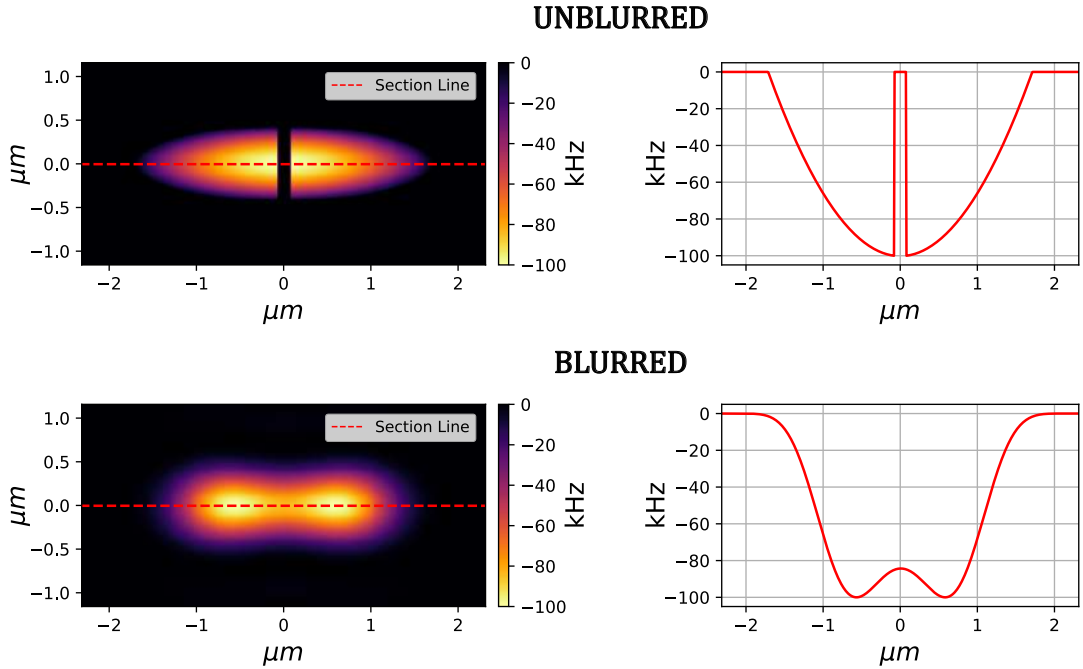


Figure 3.33: Effect of the blurring on a potential with the following parameters: $V_0 = h \cdot 100$ kHz, $\omega_x = 2\pi \cdot 2$ kHz, $\omega_y = 2\pi \cdot 8$ kHz and $d \approx 154$ nm. As shown, the effects of filtering the high frequencies in the Fourier transform of the potential are particularly pronounced at the sharp edge of the barrier.

Since the shape obtained with the setup is the blurred one, it will also be the one experienced by atoms, and so, if we want to study the tunneling rate of the double well potential, we must consider the eigenvalues obtained from its diagonalization.

As with the unblurred potentials, we must study the convergence of the lowest levels of the spectrum for different dimensions of the basis of the HO used. In Fig. 3.34, we plot the relative difference for the tunneling rate J for different values of the basis dimension. We observe that, in this case, the convergence is even better, and indeed with a basis of 35 elements, the relative difference goes to zero⁶. However, we decided to use a basis of 50 elements for our evaluations, to account for cases where the blurred potential is more distorted from a parabola than the one observed in Fig. 3.33.

The tunneling rate in this case converges to a value of $J \approx 144$ Hz. The ratio with the frequency ω gives $\frac{2\pi J}{\omega} \approx 0.072$.

⁶Note that a relative difference equal to zero does not imply an absolute convergence, since it is referred to values calculated numerically with finite precision.

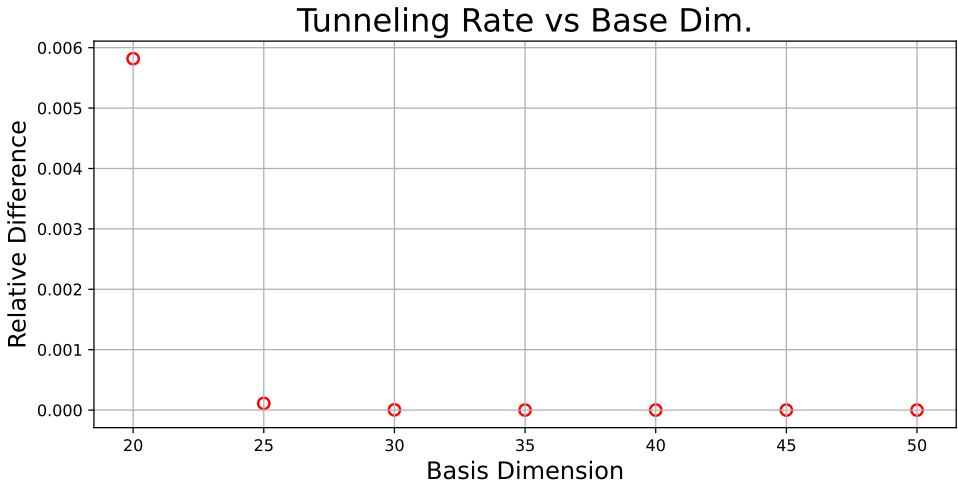


Figure 3.34: Relative difference of J for different basis dimensions of the blurred potential in Fig. 3.33

We now want to study how the tunneling rate changes for different trap heights and widths. To do this, it is useful to define a dimensionless parameter η [10] that will account for these two parameters of the double well. We define it as follows:

$$\eta = \frac{V_{barr}}{\epsilon_{HO}} \cdot \frac{d_{FWHM}}{a_{HO}} \quad (3.23)$$

where V_{barr} is the height of the barrier resulting from the blurring ($V(x=0, y=0)$ in our reference frame), and d_{FWHM} is its full width at half maximum. These two quantities are then divided by the HO natural units to obtain a dimensionless value.

From its definition, we can see that η essentially compares the barrier height and width with the energy and length scales defined by the HO basis we are using. In our case, we the mass is that of the ytterbium atom, which for the isotope ^{171}Yb is $m \approx 2.86 \cdot 10^{-23}$ Kg, and the frequency is $\omega = 2\pi \cdot 2$ kHz.

We chose this frequency because it allows us to obtain tunneling rates up to 100 Hz, while maintaining $\frac{2\pi J}{\omega} < 0.1$. We did not use a higher value because it would have increased the distance between the first doublet and the bottom of the potential. Since the barrier height is much smaller than V_0 due to the blurring produced by the objective, we risk having the lowest energy doublet already above the barrier, making the discussion of tunneling meaningless.

In Fig. 3.35, we plot the tunneling rate values obtained for various potentials, characterized by the dimensionless parameter η . As we can see, we observe an exponential behavior typical of tunneling phenomena. We fit the data with an exponential curve, allowing us to estimate the tunneling rate associated with a generic potential, given its η . In the plot, we also show three representative potential sections, corresponding to tunneling rates of around 1000, 100, and 10 Hz, respectively.

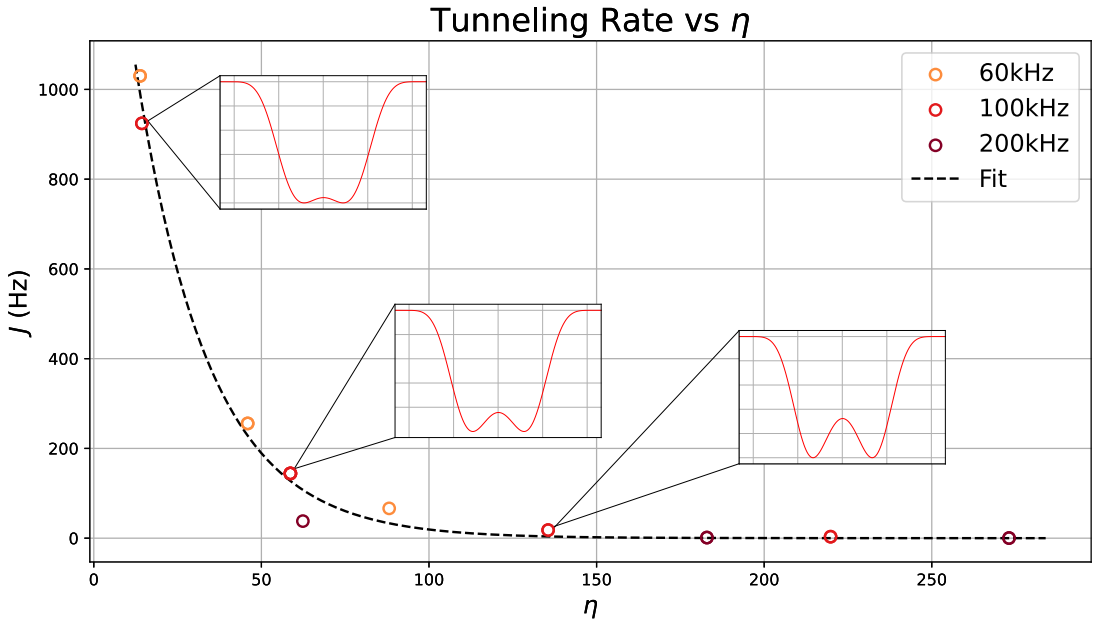


Figure 3.35: tunneling rate J for various potentials characterized by the parameter η . The values were obtained for different values of V_0 , as indicated by the legend. The three parabolas represented correspond to $V_0 = h \cdot 100$ kHz. Due to the distribution of these points, we fit them with an exponential curve: $f(x) = Ae^{-Bx}$.

Due to the value of $\omega = 2\pi \cdot 2$ kHz, we cannot consider tunneling rates higher than 200 Hz as valid. For these values, we also observe that the states $\psi_L(x)$ and $\psi_R(x)$ are not well confined to their respective sides of the barrier, which provides another reason to discard them.

The study of these cases requires the use of a different model that does not assume all the doublets decoupled from each other, allowing for tunneling events between them.

In Fig. 3.36, we can see these two states for the parabola shown at the top of Fig. 3.35, corresponding to $\eta \approx 14.34$ and $J \approx 924$ Hz.

One last consideration must be made regarding the values chosen for V_0 . Since we have fixed ω , larger values of V_0 result in larger potentials, which require more energy to be produced. For the values in Fig. 3.35, we chose V_0 such that the dimension of the potential along the x -direction did not exceed 5 μ m.

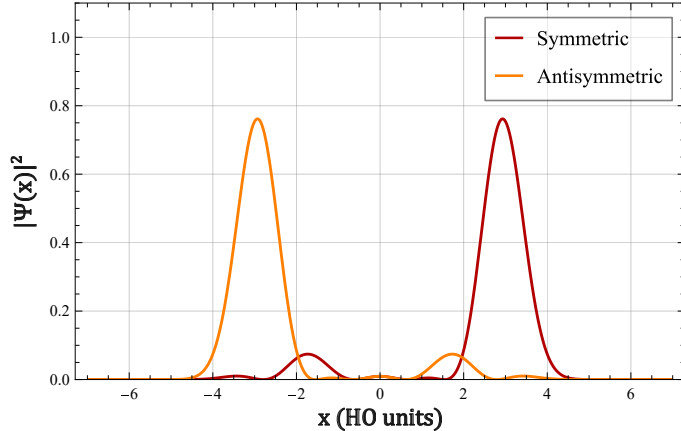


Figure 3.36: $\psi_L(x)$ and $\psi_R(x)$ for a parabola with $\eta \approx 14.34$ and $J \approx 924\text{Hz}$. Notice that the two states are not well localized on their respective sides of the barrier.

3.9 Generation via SLM

The sharp edges of the potentials defined by Eq. (3.7) will be blurred due to the filtering effect of the setup. Since we can simulate this feature, we decided to directly generate their blurred versions.

We tried to produce these potentials using the setup in Fig. 3.2, considering the blurring effect produced by the Mitutoyo objective. Our setup was built for the generation of tweezer arrays, so to use it for these more complex shapes, we need to make some modifications.

To produce the double well potential with the SLM, we need to use more than one unit cell to achieve an appropriate resolution of its profile. In our case, we have found that in the plane of the objective, the unit cell has sides of $\Delta x^{mit} = 678 \pm 12 \text{ nm}$, which means that to generate a potential of around $5 \mu\text{m}$, we can use only 7 unit cells.

To solve this problem, it is sufficient to use another scan lens with a shorter focal length (for example, 150 or 200 mm), and accordingly adjust all the optics to maintain the correct beam diameter at the microscope objective aperture [30, 37]. The only issue with this solution is how to fit it into the setup, in order to avoid an overlap between the incident and reflected beams on the SLM, while maintaining an angle $\alpha < 10^\circ$ between them, even though this is not the only solution.

Since these modifications will only involve changes to the setup elements and their arrangement, we leave this for future work. For now, we focus on determining whether we can generate the blurred potentials using the SLM, by observing the resulting pattern at the focus of the Scan Lens.

In Fig. 3.37, we can see the result of generating a parabola with $\eta \approx 92$ and

an expected tunneling rate $J \approx 28$ Hz⁷. As expected, we observe that the generated profile differs a lot from the target one due to the presence of speckle noise.

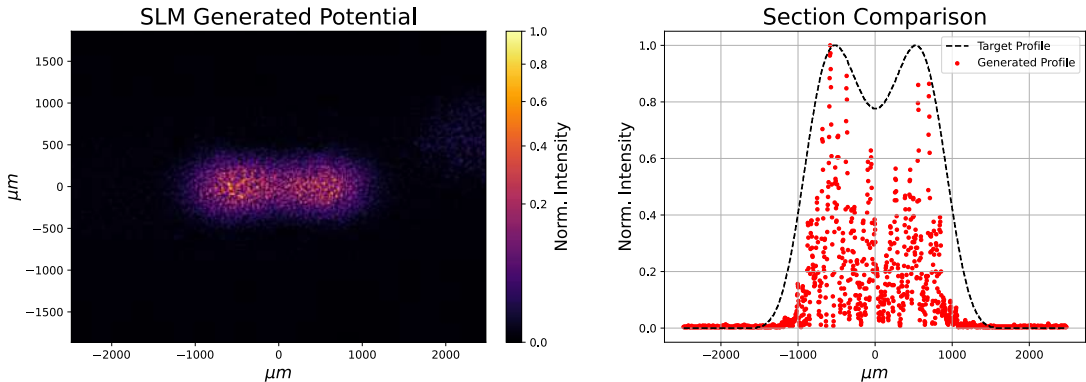


Figure 3.37: Double well generated at the focus of the scan lens. As we can see, the pattern is not smooth due to the presence of speckle noise. The target profile was a potential with $\eta \approx 92$ and $J \approx 28$ Hz.

Before discussing about the speckle noise, we want to make one last consideration. To correctly estimate the tunneling rate of the generated potentials, we must ensure that they are generated with the correct dimensions, which are obtained through the conversion factors obtained from the Fourier Calibration procedure. Obviously, the final check must be done by comparing the target and generated potentials, as well as by diagonalizing the resulting profile.

3.10 Speckle Noise

At the origin of the speckle noise, are regions with rapidly varying phase, which can lead to unwanted fluctuations in the intensity resulting in the zero intensity regions, as shown in Figs. 3.28 and 3.37.

To better understand this, imagine two nearby points in the Fourier Domain with similar amplitudes but phases that differ by about π . To satisfy the continuity condition, the field between them will be the result of the interpolation of the field in the two points. The only way to interpolate between them is by passing through a zero amplitude value [5].

Another way to understand this is by considering that since the two points are dephased by about π , they will produce destructive interference.

Speckles can be produced also by the presence of phase singularities, called vortices, which force the amplitude to go to zero, as it is the only value consistent with having all phase values between 0 and 2π at the same point [5].

This features in the far field phase pattern can be generated by defects in the

⁷Obviously, the value of η and J refer to the case where the potential is scaled to the correct dimension.

optics, but in our case are mainly a consequence of the CGH. In our algorithm, we did not take any precautions to avoid their presence in the phase of the far field phase, which is considered a free parameter, and indeed it was ignored in our discussion on the generation of the CGH.

In conclusion, to avoid the presence of speckles in our patterns, we must prevent rapidly varying changes and singularities in the far field phase profile of the generated patterns.

An algorithm that is particularly suited for generating arbitrarily shaped potentials using the SLM is the *Mixed-Region Amplitude Freedom* (MRAF) [42], a modified version of the GSA, which takes various precautions to produce patterns that are as smooth as possible.

The main difference between this algorithm and the standard version of the GSA is that it reduces the constraint on the target amplitude to only a fraction of the total Fourier domain, called the *Signal Region*, and completely removes it from the rest, called the *Noise Region*. This improvement enhances the quality of the obtained pattern, because, by relaxing some of the constraints, the algorithm is less likely to get stuck in a local minimum during the optimization process of the CGH. As a result, the algorithm is able to generate patterns with a smoother far field phase profile, reducing the presence of speckles⁸. Note that in the noise regions, we will obtain only noise.

This stagnation can also be prevented by using an initial phase for the near field, rather than a random one, that minimizes the presence of singularities in the far field phase and provides a better starting point by producing an intensity distribution similar to that of the target pattern [42].

Another way to improve the smoothness of the obtained pattern is to add an offset to the target amplitude [16]. This is particularly effective in preventing speckles caused by the presence of vortices, associated with zero amplitude values, since it makes the algorithm less tolerant towards them. The offset value should be determined empirically by testing which values prevent vortices from appearing in the generated pattern after the first iteration. This cannot be done in subsequent iterations, as the appearance of vortices cause stagnation in local minimum during the optimization process, making it difficult to remove them once they appear.

A further improvement can be obtained by using the full Helmholtz equation [16] to model the light propagation in the algorithm, instead of the one currently used. This essentially involves removing the small-angle assumptions made in Eqs. (2.9) and (2.16).

In conclusion, we have demonstrated that a simple double well potential allows us to achieve high tunneling rates for ytterbium atoms. However, to generate such patterns in our setup, we need to implement algorithms that are better suited for

⁸Notice that this is a similar situation to the one that produces better quality for non-spot patterns generated with the GSA compared to the Weighted GSA, where the presence of the weight constraint makes it more likely to get stuck in local minima during the optimization process, especially for arbitrary patterns (Fig. 2.10).

creating smooth amplitude patterns, rather than spot-based arrays.

Conclusions and Outlooks

The aim of this thesis project was to create an optical laser setup for a Spatial Light Modulator, analysing its ability in manipulating the wavefront of a laser source. The control of the device was achieved using a Python library called *slmsuite*, which simplified the implementation of all the algorithms necessary to generate the CGH and correct the optical aberrations.

This was accomplished, demonstrating the diffraction-limited performance achieved through the SLM by comparing the system's PSF with the theoretical one. We also highlight the good uniformity that can be achieved for spot-based arrays using a feedback loop.

In addition, we also studied the tunneling dynamics of ytterbium atoms inside a diffraction-limited double-well potential, demonstrating that tunneling rates of the order of 100 Hz can be achieved. In our model, we accounted for the blurring effect of the optics, particularly due to the filtering produced by the microscope objective's aperture.

To generate these patterns with the SLM, it is necessary to resolve the Speckle Noise.

The path initiated with this thesis project will continue with the implementation of the SLM in the main apparatus of the laboratory. In Fig. 3.38, a schematic image illustrates how this can be achieved. This image shows the breadboard above the science cell, where the 532 nm tweezer path is mounted. The idea is to build the SLM setup up to the Scan Lens and then, using a dichroic mirror at the indicated position, direct the beam into the Tube Lens (the last lens before the objective, with $f = 1000$ mm) already used for the other path.

As discussed in the first chapter, the optimal working condition for illuminating the microscope objective aperture is achieved when $\frac{w_0}{R} \sim 1$, where w_0 is the waist of the beam and R is the radius of the microscope aperture, which in this case is approximately 16 mm. To match this condition, considering a beam reflected from the SLM with a waist of 6.5 mm and a tube lens with $f = 1000$ mm, we can use a Scan Lens with $f = 400$ mm, the same used for the realization of the test setup (Fig. 3.2), chosen specifically for this reason.

This was obviously designed without considering the possibility of generating engineered potentials, like the one we used to simulate the tunneling dynamics. To do this we require such a demagnification to map the maximum possible number of unit cells in the Fourier Domain, in a region with an extension of a couple

of times the resolution limit of the optical system. To implement the SLM, taking this into account, and ensuring that the beam entering the objective is of the optimal size, additional optics must be inserted between the dichroic mirror and the Scan Lens.

Additionally, to generate these arbitrary potentials, an algorithm better suited CGH algorithm such as the MRAF must be implemented to obtain defect-free patterns.

Once these steps are completed, we will be able to generate patterns ranging from 2D tweezers arrays to ad hoc engineered potentials. The range of physical systems we will be able to study and simulate will be further expanded with the implementation of the clock laser, allowing us to study impurity-based systems as well as anything else that piques our curiosity.

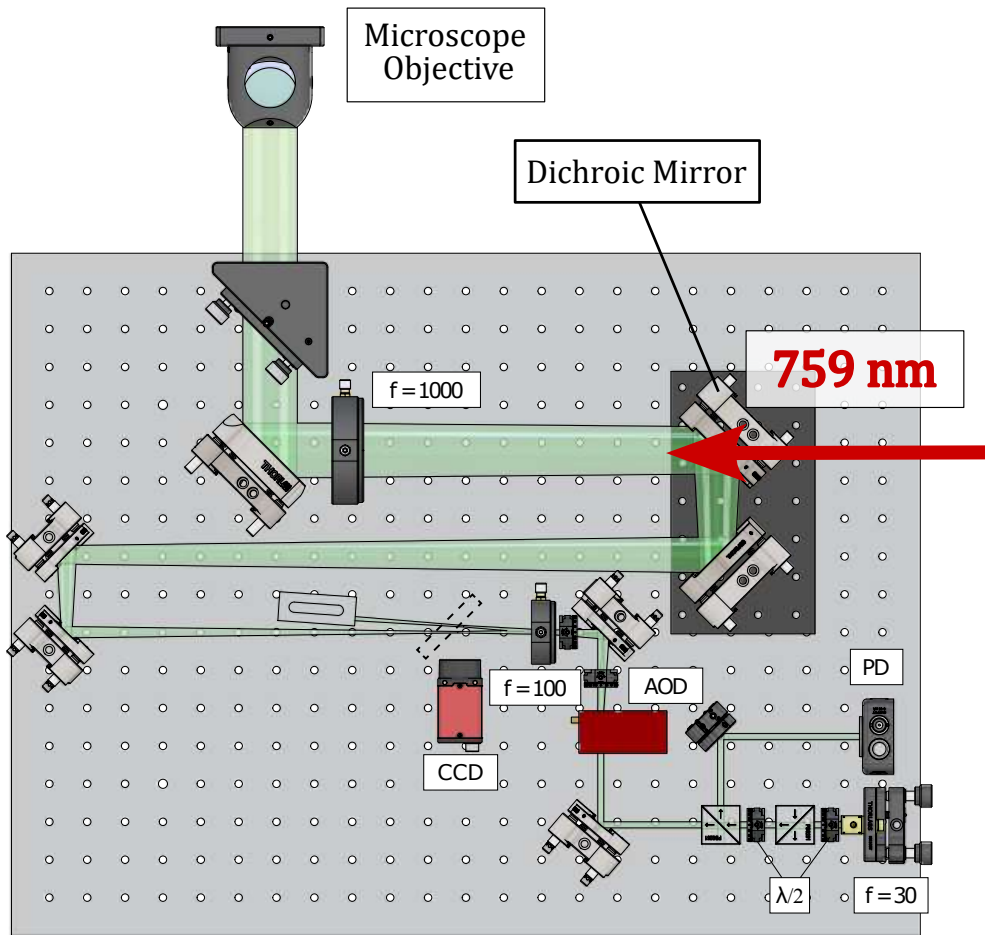


Figure 3.38: Schematic representation of the 532 nm tweezer's path, showing the possible input for the 759 nm SLM path.

Bibliography

- [1] Ireena A. Erteza. “Diffraction Efficiency Analysis for Multi-Level Diffractive Optical Elements”. In: *Sandia Report* (Nov. 1995).
- [2] Alexander Aeppli et al. “A Clock with 8×10^{-19} Systematic Uncertainty”. In: *Physical Review Letters* 133.2 (July 2024). ISSN: 1079-7114. DOI: 10.1103/physrevlett.133.023401. URL: <http://dx.doi.org/10.1103/PhysRevLett.133.023401>.
- [3] L. Amico et al. “Roadmap on Atomtronics: State of the art and perspective”. In: *AVS Quantum Science* 3.3 (Aug. 2021). ISSN: 2639-0213. DOI: 10.1116/5.0026178. URL: <http://dx.doi.org/10.1116/5.0026178>.
- [4] Daniel Barredo et al. “Synthetic three-dimensional atomic structures assembled atom by atom”. In: *Nature* 561.7721 (Sept. 2018), pp. 79–82. ISSN: 1476-4687. DOI: 10.1038/s41586-018-0450-2. URL: <http://dx.doi.org/10.1038/s41586-018-0450-2>.
- [5] Rick van Bijnen. “Quantum Engineering with Ultracold Atoms”. PhD thesis. Eindhoven University of Technology, 2013.
- [6] Dolev Bluvstein et al. “Logical quantum processor based on reconfigurable atom arrays”. In: *Nature* 626.7997 (Dec. 2023), pp. 58–65. ISSN: 1476-4687. DOI: 10.1038/s41586-023-06927-3. URL: <http://dx.doi.org/10.1038/s41586-023-06927-3>.
- [7] Thomas Chalopin et al. “Optical Superlattice for Engineering Hubbard Couplings in Quantum Simulation”. In: *Physical Review Letters* 134.5 (Feb. 2025). ISSN: 1079-7114. DOI: 10.1103/physrevlett.134.053402. URL: <http://dx.doi.org/10.1103/PhysRevLett.134.053402>.
- [8] T. Čižmàr, M. Mazilu, and K. Dholakia. “In situ wavefront correction and its application to micromanipulation”. In: *Nature Photonics* Vol. 4 (2010). DOI: <https://doi.org/10.1038/nphoton.2010.85>.
- [9] Claude N. Cohen-Tannoudji. “Manipulating Atoms with Photons”. In: *Nobel Lecture* (1997).
- [10] G. Del Pace et al. “Tunneling Transport of Unitary Fermions across the Superfluid Transition”. In: *Physical Review Letters* 126.5 (Feb. 2021). ISSN: 1079-7114. DOI: 10.1103/physrevlett.126.055301. URL: <http://dx.doi.org/10.1103/PhysRevLett.126.055301>.
- [11] G.J. Dijk. “Intensity Patterns Generated with a Spatial Light Modulator”. MA thesis. Eindhoven University of Technology, 2012.

- [12] V A Dzuba and A Derevianko. “Dynamic polarizabilities and related properties of clock states of the ytterbium atom”. In: *Journal of Physics B: Atomic, Molecular and Optical Physics* 43.7 (Mar. 2010), p. 074011. ISSN: 1361-6455. DOI: 10.1088/0953-4075/43/7/074011. URL: <http://dx.doi.org/10.1088/0953-4075/43/7/074011>.
- [13] Richard P. Feynman. “Simulating Physics with Computers”. In: *International Journal of Theoretical Physics* (1982).
- [14] C.J. Foot. *Atomic physics*. Oxford University Press, USA, 2005.
- [15] Grant R. Fowles. *Introduction to Modern Optics*. 2nd edition. Dover Publications, Inc., New York.
- [16] Alexander L. Gaunt and Zoran Hadzibabic. “Robust Digital Holography For Ultracold Atom Trapping”. In: *Scientific Reports* 2.1 (Oct. 2012). ISSN: 2045-2322. DOI: 10.1038/srep00721. URL: <http://dx.doi.org/10.1038/srep00721>.
- [17] R. W. Gerchberg and W. O. Saxton. “A Practical Algorithm for the Determination of Phase from Image and Diffraction Plane Pictures”. In: *Optik* Vol. 35.No.2 (1972).
- [18] J. W. Goodman. “Some fundamental properties of speckle*”. In: *J. Opt. Soc. Am.* 66.11 (Nov. 1976), pp. 1145–1150. DOI: 10.1364/JOSA.66.001145. URL: <https://opg.optica.org/abstract.cfm?URI=josa-66-11-1145>.
- [19] Joseph W. Goodman. *Introduction to Fourier Optics*. 2nd edition. McGraw-Hill Publishing Inc.
- [20] David J. Griffiths and Darrell F. Schroeter. *Introduction to Quantum Mechanics*. 2nd ed. Cambridge University Press, 2005.
- [21] Rudolf Grimm, Matthias Weidmüller, and Yurii B. Ovchinnikov. *Optical dipole traps for neutral atoms*. 1999. arXiv: [physics/9902072](https://arxiv.org/abs/physics/9902072). URL: <https://arxiv.org/abs/physics/9902072>.
- [22] David Gröters. “Diffraction-limited Imaging and Trapping of Ultracold Ytterbium Atoms in Optical Tweezer Arrays”. MA thesis. Ludwig-Maximilians-Universität München, 2023.
- [23] Hamamatsu. *LCOS-SLM X15213 series*. URL: <https://lcos-slm.hamamatsu.com/eu/en/related-contents.html>.
- [24] Hamamatsu. *Product information / LCOS-SLM Applications and Features*. URL: <https://lcos-slm.hamamatsu.com/eu/en/related-contents.html>.
- [25] W. Harm et al. “How to use a phase-only spatial light modulator as a color display”. In: *Optics Letters* Vol. 40.No. 4 (February 15, 2015). DOI: <http://dx.doi.org/10.1364/OL.40.000581>.
- [26] Peter W. Hawkes. *Volume 165: Imaging and Electron Physics*. Advances in Imaging and Electron Physics, 2010.

- [27] Johanna Hennebichler. “Towards the creation of a two-dimensional optical tweezer array using a liquid crystal spatial light modulator”. MA thesis. Institute for Experimental Physics, University of Innsbruck, 2023.
- [28] M. Inguscio and L. Fallani. *Atomic Physics: Precise Measurements and Ultracold Matter*. OUP Oxford, 2013. ISBN: 9780198525844. URL: <https://books.google.it/books?id=pTmaAAAAQBAJ>.
- [29] V Jelic and F Marsiglio. “The double-well potential in quantum mechanics: a simple, numerically exact formulation”. In: *European Journal of Physics* 33.6 (Sept. 2012), pp. 1651–1666. ISSN: 1361-6404. DOI: 10.1088/0143-0807/33/6/1651. URL: <http://dx.doi.org/10.1088/0143-0807/33/6/1651>.
- [30] Omar Abdel Karim. “Realization of a new experimental apparatus for the microscopic control of individual ytterbium atoms”. PhD thesis. ArQuS Lab, Università degli Studi di Trieste, 2025.
- [31] A. M. Kaufman et al. “Two-particle quantum interference in tunnel-coupled optical tweezers”. In: *Science* 345.6194 (2014), pp. 306–309. DOI: 10.1126/science.1250057. eprint: <https://www.science.org/doi/pdf/10.1126/science.1250057>. URL: <https://www.science.org/doi/abs/10.1126/science.1250057>.
- [32] D. Kim et al. “Large-scale uniform optical focus array generation with a phase spatial light modulator”. In: *Optics Letters* Vol. 14.Issue 12 (2019). DOI: <https://doi.org/10.1364/OL.44.003178>.
- [33] V. Lakshminarayanan and A. Fleck. “Zernike polynomials: A guide”. In: *Journal of Modern Optics - J MOD OPTIC* 58 (Apr. 2011), pp. 1678–1678. DOI: 10.1080/09500340.2011.633763.
- [34] Sirah Lasertechnik. *Datasheet Matisse CS*. URL: <https://www.sirah.com/lasers/cw/matisse-c/>.
- [35] R. Di Leonardo, F. Ianni, and G. Ruocco. “Computer generation of optimal holograms for optical trap arrays”. In: *Optics Express* Vol. 15.Issue 4 (2007). DOI: <https://doi.org/10.1364/OE.15.001913>.
- [36] P. D. Lett et al. “Optical molasses”. In: *J. Opt. Soc. Am. B* 6.11 (Nov. 1989), pp. 2084–2107. DOI: 10.1364/JOSAB.6.002084. URL: <https://opg.optica.org/josab/abstract.cfm?URI=josab-6-11-2084>.
- [37] Ivaylo Sashkov Madjarov. “strontium atoms in optical tweezer arrays”. PhD thesis. CALIFORNIA INSTITUTE OF TECHNOLOGY, Pasadena, California, 2021.
- [38] Hannah J. Manetsch et al. *A tweezer array with 6100 highly coherent atomic qubits*. 2024. arXiv: 2403.12021 [quant-ph]. URL: <https://arxiv.org/abs/2403.12021>.
- [39] F. Marsiglio. “The harmonic oscillator in quantum mechanics: A third way”. In: *American Journal of Physics* 77.3 (Mar. 2009), pp. 253–258. ISSN: 1943-2909. DOI: 10.1119/1.3042207. URL: <http://dx.doi.org/10.1119/1.3042207>.

- [40] I. Moreno et al. “Diffraction efficiency of stepped gratings using high phase-modulation spatial light modulators”. In: *Optics and Lasers in Engineering* Volume 126 (2020). DOI: <https://doi.org/10.1016/j.optlaseng.2019.105910..>
- [41] F. Nogrette et al. “Single-Atom Trapping in Holographic 2D Arrays of Microtraps with Arbitrary Geometries”. In: *Phys. Rev. X* 4 (2 May 2014), p. 021034. DOI: 10.1103/PhysRevX.4.021034. URL: <https://link.aps.org/doi/10.1103/PhysRevX.4.021034>.
- [42] Matthew Pasienski and Brian DeMarco. “A high-accuracy algorithm for designing arbitrary holographic atom traps”. In: *Opt. Express* 16.3 (Feb. 2008), pp. 2176–2190. DOI: 10.1364/OE.16.002176. URL: <https://opg.optica.org/oe/abstract.cfm?URI=oe-16-3-2176>.
- [43] Spectra Physics. *Matisse C Datasheet*. URL: <https://www.spectra-physics.com/en/f/matisse-c-tunable-ring-laser>.
- [44] Grégoire Pichard et al. “Rearrangement of individual atoms in a 2000-site optical-tweezer array at cryogenic temperatures”. In: *Phys. Rev. Appl.* 22 (2 Aug. 2024), p. 024073. DOI: 10.1103/PhysRevApplied.22.024073. URL: <https://link.aps.org/doi/10.1103/PhysRevApplied.22.024073>.
- [45] MIT Quantum Photonics AI Group. *slmsuite*. URL: <https://slmsuite.readthedocs.io/>.
- [46] Bahaa E. A. Saleh and Malvin Carl Teich. *Fundamentals of Photonics*. 2nd edition. John Wiley Sons, Inc., Publication. Chap. 6, pp. 215–227.
- [47] Patrick Salter and Martin Booth. *Designing and aligning optical systems incorporating liquid crystal spatial light modulators (SLMs)*. URL: <https://doi.org/10.5281/zenodo.3664146>.
- [48] Sara Sbernardori. “Coherent control of the ytterbium atom optical qubit”. MA thesis. Università degli Studi di Trieste, 2024.
- [49] Francesco Scazza. “Probing SU(N)-symmetric orbital interactions with ytterbium Fermi gases in optical lattices”. PhD thesis. LMU München: Faculty of Physics, 2015.
- [50] Hou-Ji Shao et al. *Observation of the antiferromagnetic phase transition in the fermionic Hubbard model*. 2024. arXiv: 2402.14605. URL: <https://arxiv.org/abs/2402.14605>.
- [51] Benjamin M. Spar et al. “Realization of a Fermi-Hubbard Optical Tweezer Array”. In: *Phys. Rev. Lett.* 128 (22 June 2022), p. 223202. DOI: 10.1103/PhysRevLett.128.223202. URL: <https://link.aps.org/doi/10.1103/PhysRevLett.128.223202>.
- [52] Daniel Adam Steck. *Quantum and Atom Optics*. 2007.
- [53] Charles H. Townes. “Production of Coherent Radiation by Atoms and Molecules”. In: *Nobel Lecture* (1964).
- [54] Marijn Leonardus Venderbosch. “Holographic Optical Tweezers for Arrays of Single Atoms”. MA thesis. Eindhoven University of Technology, 2022.

- [55] Julian Florian Wienand. “Quantum gas microscopy of fluctuating hydrodynamics in optical ladders”. PhD thesis. LMU München: Faculty of Physics, 2024.
- [56] A. Zenesini et al. “False vacuum decay via bubble formation in ferromagnetic superfluids”. In: *Nature Physics* 20.4 (Jan. 2024), pp. 558–563. ISSN: 1745-2481. DOI: 10.1038/s41567-023-02345-4. URL: <http://dx.doi.org/10.1038/s41567-023-02345-4>.

Ringraziamenti

Vorrei concludere questa tesi con alcune parole di ringraziamento.

Per prima cosa vorrei ringraziare il Prof. Francesco Scazza per avermi dato la possibilità di lavorare nel suo incredibile laboratorio, iniziandomi alle bellezze della fisica sperimentale.

Vorrei poi ringraziare tutti i componenti dell'ArQus Lab, e in particolare Alessandro e il Maestro Omar per avermi insegnato a stare in un laboratorio, a Sara per le indispensabili pause caffè, e a Riccardo Forti per il suo prezioso supporto durante alcune fasi di questa tesi.

Durante questi anni a Trieste ho avuto modo di conoscere tante persone fantastiche. Tra di queste, il mio caro amico Davide Bernocco, con il quale oltre ad attraversare tempeste, ho anche passato ore discutendo di fisica. Ti auguro di raggiungere il prima possibile questo traguardo.

Ringrazio il Judo Club Ken Otani di Trieste, e in particolare Mara e Fabio, per avermi insegnato tanto, sia riguardo il judo che riguardo la vita.

Continuiamo con la banda di scappati di casa comunemente detti "gli amici di giù", con i quali è sempre un piacere rivedersi durante i "Ritrovi Internazionali del Paesano". Tra loro, voglio menzionare Cristian Ferdinando Di Lorenzo, mio compagno in questa parentesi triestina della vita. Mi raccomando, cerca di mangiare e di non perdere tutti i capelli adesso che me ne vado.

Un immenso grazie alla mia famiglia, e in particolare ai miei genitori e a mia sorella Floriana, per il loro supporto incondizionato, nonostante le difficoltà degli ultimi anni. Questa tesi è dedicata a voi.

Infine, vorrei ringraziare Anna. Grazie per essermi sempre vicina e per farmi ridere così tanto. Sei una persona straordinaria e non hai idea di quanto io sia fortunato ad averti al mio fianco.

Nino